DISSERTATION

# SPIN WAVE INSTABILITY PROCESSES IN ANISOTROPIC FERRITE MATERIALS

Submitted by
Alexey V. Nazarov
Department of Physics

In partial fulfillment of the requirements
For the Degree of Doctor of Philosophy
Colorado State University
Fort Collins, Colorado, USA
Summer 2002

UMI Number: 3064010



ProQuest Information and Learning Company
300 North Zeeb Road
P.O. Box 1346
Ann Arbor, MI 48106-1346

COLORADO STATE UNIVERSITY

JULY 8, 2002

WE HEREBY RECOMMEND THAT THE DISSERTATION PREPARED UNDER OUR SUPERVISION BY ALEXEY V. NAZAROV ENTITLED SPIN WAVE INSTABILITY PROCESSES IN ANISOTROPIC FERRITE MATERIALS BE ACCEPTED AS FULFILLING IN PART REQUIREMENTS FOR THE DEGREE OF DOCTOR OF PHILOSOPHY.

Committee on Graduate Work

Richard E. Eykholt

Richard E. Eykholt (Member)

Stuart Field

Stuart Field (Member)

Carmen S. Menoni (Outside)

Carl E. Patton (Adviser)

David A. Krueger

David A. Krueger (Department Head)

# ABSTRACT OF DISSERTATION

## SPIN WAVE INSTABILITY PROCESSES IN ANISOTROPIC FERRITE MATERIALS

A theoretical and experimental study of spin wave instability processes in anisotropic ferrite materials has been performed. The theory of spin wave instability for ferromagnetic insulators is extended to include generalized anisotropy based on a tensor formulation of the static and dynamic effective fields. The formalism is set up for saturated magnetic ellipsoids and a general microwave field configuration. The analysis yields working formulae for the threshold microwave field amplitude evaluations and critical mode determinations. Numerical simulations are used to calculate threshold field and critical modes for first order oblique pumping processes in a thin disk with easy plane anisotropy. The theory was successfully applied to the analysis of comprehensive experimental data on anisotropic ferrite materials for various static and microwave field configurations.

The dependence of the threshold field amplitude on the external field was investigated experimentally at 9 and 16.7 GHz. The high power thresholds were measured for different geometrical configurations and spin wave relaxation rates were determined. The data showed qualitative agreement with the theoretical calculations. The spin wave linewidth was found to be independent of the spin wave propagation direction. The specific results are presented for three different ferrite materials, liquid phase epitaxy (LPE) yttrium iron garnet (YIG) single crystal thin films, polycrystalline hipped YIG, and Y-type zinc (Zn-Y) single crystal easy plane hexagonal ferrite.

In LPE YIG films, the spin wave linewidth was 0.2 Oe at 9 GHz and the influence of thin film geometry and small magnetocrystalline anisotropy on the high power thresholds was found. In hipped YIG, the spin wave linewidth was determined by the grain size and was 1.2 Oe at 9 GHz and 0.6 Oe at 16.7 GHz. In Zn-Y, 9 GHz data demonstrated related sample size effects, so that high power thresholds were inversely proportional to the sample lateral size. At 16.7 GHz, there were no sample size effects and oblique pumping measurements were performed. It was found that the spin wave linewidth increases from 12 Oe to about 18 Oe if the magnetization is pulled out of the easy crystallographic plane.

Alexey V. Nazarov
Department of Physics
Colorado State University
Fort Collins, CO 80523
Summer 2002

## ACKNOWLEDGEMENTS

I thank my thesis adviser, Professor Carl E. Patton, for his assistance, guidance, and encouragement through the duration of this project. He proposed the subject and persuaded me to investigate the high power microwave properties of ferrite materials.

I would like to thank Professor Richard E. Eykholt and Professor Stuart B. Field for helpful advice during my period of study as a graduate student at Colorado State University.

Dr. Jerome J. Green, Dr. Mark M. Scott, Professor Yuri M. Fetisov of Moscow Institute of Radioengineering, Moscow, Russia, and Professor Boris A. Kalinikos of the St. Petersburg Electrotechnical University, St. Petersburg, Russia are gratefully acknowledged for helpful discussions of the manuscript.

I would also like to thank all of my colleagues in the Magnetics Laboratory, especially Richard G. Cox, Dr. David Menard, Dr. Christoph Mathieu (now all three with Seagate Technology in Minneapolis), Dr. Sergey Lebedev, and Dr. Yong-Yeal Song.

The samples used in this investigation were kindly provided by Dr. M. Marysko of Institute of Physics, Prague, Czech Republic, Dr. G. Argentina of Pacific Ceramics, Inc., Sunnyvale, CA, and by Dr. M. A. Wittenauer, now at Colorado State University.

I also acknowledge my M. S. thesis advisor Professor Alexander G. Gurevich of the Ioffe Physico-Technical Institute, St. Petersburg, Russia for his introduction to the area of microwave magnetic materials. My parents are deeply appreciated for moral support.

This work was supported by the United States Office of Naval Research, Grant N00014-94-1-0096.

# TABLE OF CONTENTS

# CHAPTER 1

# INTRODUCTION

The goal of this introduction is to give background and motivation for the thesis research and provide an overview of the accomplished work with a detailed summary of each chapter. The introduction describes the effect of large magnetocrystalline anisotropy in ferrite materials and establishes the physics of spin wave instability processes.

## 1.1. Background and Motivation

Ferrites are oxide based magnetic materials with negligible conductivity. These materials are widely used in many devices operating in the microwave and millimeter wave frequency ranges. Such microwave applications include radar, electronic warfare systems, and rapidly blooming wireless communication, such as cellular phones. Spin wave instability is a nonlinear effect which occurs in ferrite magnetic materials when the microwave power level reaches a certain critical value. This effect can reduce the useful power range of microwave ferrite devices. From another point of view, the investigation of the spin wave instability processes provides valuable information about microwave loss in ferrite materials.

Ferrites are used in the device component design because of their non-reciprocal and non-linear effect on electromagnetic fields. Such devices include phase shifters, isolators, filters, tunable oscillators, power limiters, and more. The performance of these devices at microwave frequencies below 30 GHz has been investigated for decades. However, due to the recent rapid development in microwave applications, there is a demand to extend many of these device applications to frequencies above 50 GHz (Adam *et al.* [1991] and Vittoria [1980]) and to develop new ferrite materials for standard microwave applications at frequencies below 30 GHz.

Microwave ferrite devices utilize various physical effects. Devices such as resonance isolators, ferrite tuned oscillators, and some types of filters use the phenomenon of ferromagnetic resonance (FMR). Ferromagnetic resonance was discovered by Griffiths in 1946 in magnetic metal films and was first explained by Kittel in 1948. At the resonance, the absorbed microwave power drastically increases. The resonance occurs when the magnetic material is subject to microwave radiation with a frequency which is close to the frequency of the free gyroscopic precession of the magnetization. The frequency of the free gyroscopic precession is proportional to the applied magnetic field with a coefficient of 2.8 GHz/kOe. A larger applied field is necessary in order to operate a device at higher frequencies. Existing permanent magnets can provide a field strength up to 13 kOe and, therefore, the maximum FMR frequency is less than 40 GHz in standard isotropic ferrite materials. The use of electromagnets and superconductor magnets makes ferrite devices impractical because they would consume too much space and power. Therefore, successful device implementation for microwave frequencies above 30 GHz requires other solutions.

For isotropic ferrites, an increase in the operational FMR frequency requires an increase in applied field. One of the ways to decrease the required magnetic field and increase the operational frequency of microwave ferrite devices is to use a ferrite material with a large magnetocrystalline anisotropy. These ferrite materials have a preferred direction of magnetization with respect to the crystal axes. Hexagonal ferrites with large anisotropy represent one class of such ferrite materials. These hexagonal ferrites can have easy plane or easy axis anisotropy. The effective field due to the anisotropy in hexagonal ferrites with a reasonable Curie temperature is in the range of 8 to 20 kOe. These anisotropy fields function in a similar way to applied magnetic fields and can extend the frequency range of microwave ferrite devices up to 100 GHz. There is a problem, however. Currently available hexagonal ferrite materials exhibit relatively large microwave losses compared to ferrites with small anisotropy such as yttrium iron garnet.

The mechanisms of these large losses are not yet completely understood (Lebedev *et al.* [2002] and Patton [1988]).

The standard technique to study microwave losses in ferrite materials is FMR linewidth measurements (Lax and Button [1962]). The most commonly used FMR linewidth technique involves the microwave power absorption measurement at a constant frequency as the external static field is swept through the resonance position. The separation of the field points on the microwave absorption curve where absorbed power is half of its maximum value at the FMR field position is termed the half power FMR field linewidth $\Delta H_0$. The FMR linewidth $\Delta H_0$ can be used as a measure of the relaxation rate in the magnetic material.

When the amplitude of the microwave magnetic field becomes large, the FMR absorption curve can broaden. Moreover, additional microwave absorption may occur at magnetic fields below the FMR field. These effects were first observed by Bloembergen and Damon in 1952 and Bloembergen and Wang in 1954. These phenomena were explained by Anderson and Suhl in 1955. Due to the nonlinearity of the spin system, spin waves are coupled to the uniform magnetization mode excited by the external microwave magnetic (pumping) field. When the amplitude of this uniform mode exceeds a certain threshold value, the energy acquired by spin waves from this mode compensates spin wave losses and an exponential growth of the spin wave amplitudes begins. This effect is called spin wave instability. Spin wave instability influences the high power response of microwave ferrite devices through a drastic increase of microwave loss above specific threshold power level. This effect reduces the useful power range of linear devices. However, this effect can be useful in microwave power limiters (Dixon [1978]).

The spin wave instability theory was developed by Suhl in 1957 and Schlömann in 1959. The broadening of the FMR resonance absorption peak is termed resonance saturation (RS) and the microwave absorption at magnetic fields below the FMR field is termed subsidiary absorption (SA). In addition, Schlömann *et al.* [1960] discovered that spin wave instability could be caused directly by a microwave magnetic field parallel to the external static field. This phenomenon is called parallel pumping (PP). Resonance saturation is a second order process in which excited spin waves are at the pump frequency. Subsidiary absorption and parallel pumping are first order processes in which excited spin waves are at one half the pump frequency. These formulations were for isotropic ferrites. Only circularly polarized transverse and linearly polarized parallel pumping microwave field configurations were considered.

In order to deal with real ferrite materials and microwave fields which approximate device environments, it is necessary to extend the above theories to include anisotropy and more general pumping configurations. Yakovlev [1968], Green *et al.* [1968], and Patton [1969 and 1970] considered oblique pumping with a general microwave field polarization. These treatments considered only first order processes. The Suhl-Schlöman first order analysis for oblique pumping was also extended to include cubic anisotropy by Yakovlev and Burdin [1974] and Patton [1979]. Numerous authors (Schlömann *et al.* [1963], Green and Healy [1963], Dixon *et al.* [1965], Helszajn and McStay [1970 and 1972], Gurevich *et al.* [1999], and Cox *et al.* [2001]) have studied the high power response of uniaxial and planar ferrites. These various papers consider first and second order effects, RS, SA, and PP processes, and non-collinear magnetization field configurations.

Most of the theories contained in the above references were concerned with one special case or another. None of these works provide a fully general theoretical framework for the analysis of first and second order processes in a material of general shape, with a general anisotropy, or for a possibly non-collinear magnetization and field. The goal of the theoretical part of the work described in Chapter 2 was to develop such a theory and relate theoretical predictions to experimental data given in Chapters 4, 5, and 6. The analysis yields working formulae for the threshold microwave field amplitude for spin wave instability, specified as $h_c$, as a function of the spin wave decay rate, and the spin wave wave vector **k**. The spin wave decay rate is expressed in linewidth units through a "spin wave linewidth" parameter $\Delta H_k$. The $h_c$ threshold is **k** dependent. For a specific material, sample shape, static magnetic field, and microwave frequency and pumping configuration, one may determine the minimum $h_c$ and the corresponding critical mode **k** for this minimum. This minimum threshold, denoted below as $h_{crit}$, should correspond to the microwave threshold observed experimentally.

One can measure $h_{crit}$ vs. static field and use the theory to fit the data to obtain values of $\Delta H_k$. This procedure can also be used one to determine $\Delta H_k$ as a function of **k**. The spin wave linewidth value and its **k**-dependence contain valuable information about intrinsic relaxation mechanisms in ferrites (Sparks [1964] and Gurevich and Melkov [1996]). Unlike the FMR linewidth, the spin wave linewidth is not sensitive to sample surface quality or pores.

The main objective of this work was to investigate high power microwave thresholds and understand the relevant spin wave instability processes and loss mechanisms in ferrite materials with potential high frequency device applications. The emphasis is on the thin film geometry and the effects of magnetocrystalline anisotropy. The experimental tool for this investigation is the dependence of the threshold field $h_{crit}$ on the static field, pumping configuration, and the sample shape. The FMR characterization was also employed. Three different ferrite materials were studied experimentally, liquid phase epitaxy (LPE) low anisotropy yttrium iron garnet (YIG) single crystal thin films, dense polycrystalline hipped YIG, and Y-type zinc (Zn-Y) single crystal easy plane hexagonal ferrite. All of these materials have potential high frequency applications.

However, the large magnetocrystalline anisotropy which makes hexagonal ferrites attractive for millimeter-wave applications complicates the understanding of the spin wave instability processes. In order to provide a more tutorial approach, the simpler case of the yttrium iron garnet (YIG) ferrites with small anisotropy and low losses was investigated in this work first. Gaussian cgs units are employed throughout the work.

### 1.2. Investigation Overview

Chapter 2 introduces the fundamentals of the magnetization dynamics in ferrite materials and establishes theoretical grounds for the investigation of the spin wave instability processes. Section 2.1 establishes the laboratory frame sample and field geometry for the problem, the fundamental dynamic response, and effective field equations needed for the analysis. This is done for an ellipsoidal shape sample and a general anisotropy based on free energy considerations. This section also introduces the concept of a precession reference frame for the analysis of the dynamic response and establishes operating equations for static equilibrium.

Section 2.2 introduces the uniform precession mode and spin waves and incorporates the formalism established in the previous section to develop the coupled equations for the uniform precession mode and spin wave amplitudes in the linear case, when non-linear spin wave interactions can be neglected. Section 2.3 incorporates the formalism established in previous sections to develop working equations for spin wave instability and combines the results of the previous sections to obtain operational expressions for the threshold microwave field amplitude for spin wave instability under the general conditions outlined above.

Finally, Section 2.4 gives an example calculation for first order processes at 17 GHz in a typical Y-type hexagonal ferrite with planar anisotropy. Curves of the threshold microwave field $h_{crit}$ vs. the external static field $H_{ext}$ as well as results on the associated critical modes are presented. The results of the numerical calculations will be an important part of the oblique pumping data analysis in Chapter 6.

Chapter 3 introduces three specific ferrite materials that were studied, describes experimental techniques for threshold field measurements, and presents example results. Section 3.1 enumerates the three materials, single crystal liquid phase epitaxy (LPE) YIG thin (110) films, hipped polycrystalline bulk YIG spheres and disks, and single crystal *c*-plane plates of easy plane Zn-Y hexagonal ferrite. The chemical composition, crystalline structure, and growth methods are discussed along with sample preparation techniques. For hipped YIG and Zn-Y, the results of static magnetic property measurements on saturation induction and anisotropy field parameter are also given.

Section 3.2 describes the high power microwave spectrometer. The system was originally developed by Cox for X-band use at 9 GHz (Cox *et al.* [2001]). The current spectrometer utilizes a high-Q reflection cylindrical cavity for measurements at 9 GHz and a rectangular cavity for measurements at 17 GHz. Procedures for microwave field amplitude calibration are presented. The experimental setup allows one to obtain the cavity reflection coefficient vs. microwave field amplitude for different values of the applied static field, applied field orientation, and sample orientation. Section 3.3 is concerned with the threshold field determinations from such data. Two threshold determination methods and their advantages are discussed in this section.

Section 3.4 presents example results of the threshold field measurements in a polycrystalline YIG sphere at 9 GHz. The section establishes necessary terminology and procedures for the analysis of the results that are presented in Chapters 4, 5, and 6 in the form of threshold field $h_{crit}$ vs. applied field $H$ curves, often termed butterfly curves. Section 3.4 also establishes a framework for the analysis of the $h_{crit}$ data in terms of the theory. This framework forms the basis for the analysis of the $h_{crit}$ data presented in the next three chapters. This analysis reveals the excited critical modes and gives the spin wave linewidth $\Delta H_k$ dependence as a function of wave vector $\mathbf{k}$.

Chapter 4 presents the results of the parallel pumping threshold field measurements in single crystal LPE YIG (110) oriented thin films at 9 GHz. The results demonstrate the influence of the thin film geometry, which forces excited spin waves to propagate in the film plane, and small magnetocrystalline anisotropy on the spin wave excitation. Section 4.1 gives an overview of the data on FMR linewidth and the specifics of the $h_{crit}$ measurements for these films. Section 4.2 presents results on normally magnetized films of different diameters. In this case, spin waves propagate along an arbitrary direction in the film plane.

Section 4.3 presents the results on an in-plane magnetized film with $H$ applied along one of the main crystallographic axes. In this case, spin waves propagate along a specific direction in the film plane. Small magnetocrystalline anisotropy affects the spin wave instability threshold and shifts the butterfly curve kink point. The data agree with the results of the theoretical predictions in Chapter 2. It was found that the spin wave linewidth does not depend on the spin wave propagation direction. The $k = 0$ extrapolated spin wave linewidth was 0.18 Oe, close to the lowest reported values for bulk single crystal YIG (Kasuya and Le Craw [1961] and Yakovlev *et al.* [1971]).

Chapter 5 presents results of the high power microwave measurements in hipped polycrystalline YIG. This dense material has a very low FMR linewidth due to the absence of porosity. The investigation focuses on the influence of small anisotropy which exists in grains and changes microwave properties such as FMR linewidth and high power response. The results show that spin wave excitation for parallel pumping occurs independently in each individual grain. This effect does not appear to be important for the FMR linewidth and for perpendicular pumping. Chapter 5 also demonstrates that the intrinsic microwave loss in hipped polycrystalline YIG can be similar to the loss in single crystal YIG and that the spin wave linewidth is determined by the grain size.

Section 5.1 shows the results of the FMR linewidth measurements. Section 5.2 presents the results of the parallel and perpendicular pumping threshold field measurements at 9 GHz and the parallel pumping threshold field measurements at 16.7 GHz. Section 5.3 discusses the results of the previous sections and presents a spin wave linewidth analysis based on the transit time model.

Chapter 6 presents the results of the spin wave instability investigation in easy plane Zn-Y hexagonal ferrite plates with large magnetocrystalline anisotropy. The experimental results for parallel pumping at 9 and 16.7 GHz in in-plane magnetized Zn-Y plates will be presented first. At 9 GHz, data demonstrated sample size effects, so that high power thresholds were inversely proportional to the sample lateral size. At 16.7 GHz, there were no considerable size effects and experimental butterfly curves were in agreement with the developments of Chapter 2. The simple theoretical analysis will be presented only for the parallel pumping data.

The more complicated pumping situations include in-plane oblique pumping where $H$ is rotated in the plate plane and out of plane oblique pumping where $H$ is rotated in the plane perpendicular to the plate. The full power of the general spin wave instability theory of Chapter 2 was applied to the 16.7 GHz oblique pumping data. The theoretical model was consistent with the data. As a result of the data analysis, a "magnetic stress" effect was found. The results of the analysis show that $\Delta H_k$ is independent of the spin wave propagation direction but increases with an increase in the magnetic stress caused by the static magnetization deviation from the easy plane.

Section 6.1 describes the sample geometry and FMR characterization. The FMR characterization is used to obtain working parameters for the spin wave instability analysis. Section 6.2 establishes working equations for the parallel pumping data analysis. In this section, the results of the parallel pumping measurements at 9 and 16.7 GHz are presented and the sample size effect is discussed. Sections 6.3 and 6.4 present the in-plane and out of plane oblique pumping $h_{crit}$ data and analysis for the Mn-substituted Zn-Y disk at 16.7 GHz, respectively.

Chapter 7 presents a summary of the main results of the spin wave instability investigation in low loss single crystal, polycrystalline, and high anisotropy ferrite materials. Conclusions on the influence of thin film geometry and magnetocrystalline anisotropy on spin wave instability thresholds, the spin wave linewidth dependence on the spin wave propagation direction, transit time limited spin wave linewidth, and the effect of magnetic stress on spin wave linewidth are presented. Problems for future work in the area of high power microwave properties of magnetic materials are indicated.

# CHAPTER 2

# THEORY OF SPIN WAVE INSTABILITY PROCESSES

The focus of this chapter is on an introduction to uniform mode dynamics and spin waves and a formal development of spin wave instability theory in magnetic insulators with large magnetocrystalline anisotropy.

Section 2.1 establishes the laboratory frame sample and field geometry for the problem, the fundamental dynamic response, and effective field equations needed for the analysis. This section also introduces the concept of a precession reference frame for the analysis of the dynamic response and establishes operating equations for static equilibrium. Section 2.2 introduces the uniform precession mode and spin waves and incorporates the formalism established in the previous section to develop the coupled equations for the uniform precession mode and spin wave amplitudes in the linear case.

Section 2.3 incorporates the formalism established in previous sections to develop working equations for spin wave instability and combines the results of the previous sections to obtain operational expressions for the threshold microwave field amplitude for spin wave instability under the general conditions outlined above. Finally, Section 2.4 gives an example calculation for first order processes at 17 GHz in a typical Y-type hexagonal ferrite with planar anisotropy. Curves of the threshold microwave field $h_{crit}$ vs. the external static field $H_{ext}$ as well as results on the associated critical modes are presented. The results of the numerical calculations will be an important part of the oblique pumping data analysis in Chapter 6.

## 2.1. Sample Geometry and Effective Fields

Materials are called magnetic because of the magnetic fields which are present in these materials. These magnetic fields can be external and internal. External fields are fields that are applied from an external source. Internal fields are produced in magnetically ordered substances by the microscopic magnetic moments of each atom. Only magnetically ordered substances will be considered in this work. The orientation of magnetic moments in these substances occurs spontaneously, in the absence of an external magnetic field. The simplest type is a ferromagnet.

In this chapter, ferrites will be treated as ferromagnets. A continuum approach can be used to describe dynamic processes in ferromagnets. In this approach, the microscopic structure of the ferromagnet is ignored and the magnetization $\mathbf{M}$ is averaged over a small but macroscopic volume. Vector $\mathbf{M}$ is the quantity that enters the equations of macroscopic electrodynamics (Gurevich and Melkov [1996]). The continuum approach allows one to use the classical theory which will be engaged in this work.

The problem involves the response of the magnetization to various magnetic fields for a sample with a specific geometry. Figure 2.1 shows the basic sample geometry. One has an ellipsoidal-shaped single domain ferromagnetic sample with principal axes along $X$, $Y$, and $Z$. The ellipsoidal sample shape is used to provide the uniformity of the magnetization. The externally applied uniform static magnetic field $\mathbf{H}_{ext}$ has polar and azimuthal angles $\theta_H$ and $\varphi_H$ in the $(X, Y, Z)$ *laboratory frame*. The static magnetization vector $\mathbf{M}_s$ has polar and azimuthal angles $\theta_M$ and $\varphi_M$, respectively. In general, $\mathbf{H}_{ext}$ and $\mathbf{M}_s$ will not be collinear. The static equilibrium orientation of $\mathbf{M}_s$ will

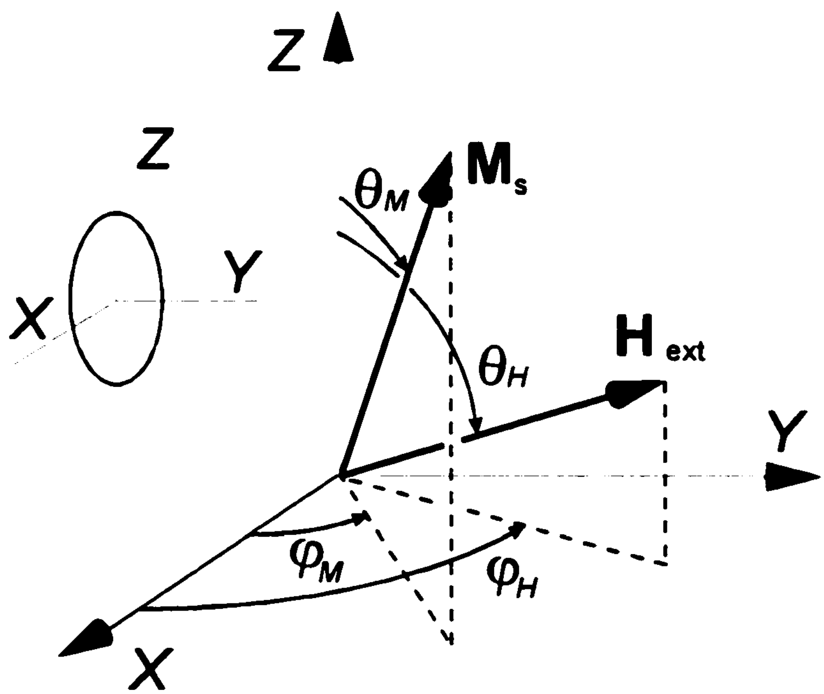


Figure 2.1. The laboratory ($X$, $Y$, $Z$) coordinate frame. The external static field $\mathbf{H}_{ext}$ is applied at a polar angle $\theta_H$ and an azimuthal angle $\varphi_H$. The static magnetization $\mathbf{M}_s$ lies at a polar angle $\theta_M$ and an azimuthal angle $\varphi_M$. The inset shows that the coordinate axes ($X, Y, Z$) coincide with the principal directions of the ellipsoidal sample.

be determined by direction and magnitude of $\mathbf{H}_{ext}$, the sample shape and corresponding demagnetizing factors $N_X$, $N_Y$, and $N_Z$, and the anisotropy of the material. These considerations will be developed shortly.

In order to solve the combined static and dynamic problems, it is necessary to develop analytic expressions for the static and dynamic effective fields. One may start this process with a magnetization vector written in the form

$$\mathbf{M} = \mathbf{M}_s + \mathbf{m} . \tag{2.1}$$

In general, the dynamic magnetization $\mathbf{m}$ is a function of the time $t$ and the position $\mathbf{r}$ in the sample, and may be expanded into a spatial Fourier series according to

$$\mathbf{m}(\mathbf{r},t) = \sum_{\mathbf{k}} \mathbf{m}_{\mathbf{k}}(t) e^{i\,\mathbf{k}\cdot\mathbf{r}} , \tag{2.2}$$

where $\mathbf{k}$ denotes the wave vector of an allowed spin wave. The term for $\mathbf{k} = 0$ corresponds to the uniform mode response $\mathbf{m}_0$. From here on, references to $\mathbf{m}(\mathbf{r},t)$ will be given as $\mathbf{m}$.

One may also write the total effective magnetic field as an $\mathbf{H}_{eff}$ and break this field down into various physical terms according to Patton [1979]

$$\mathbf{H}_{eff} = \mathbf{H}_{ext} + \mathbf{H}_D + \mathbf{H}_A + \mathbf{h}_{ex} + \mathbf{h} , \tag{2.3}$$

where $\mathbf{H}_D$ denotes the Maxwellian field due to sample shape demagnetizing effects and magnetic dipole interactions within the sample, $\mathbf{H}_A$ is an effective field due to anisotropy, $\mathbf{h}_{ex}$ is an effective field due to exchange, and $\mathbf{h}$ denotes the applied external microwave field. The $\mathbf{H}_D$ and $\mathbf{H}_A$ fields contain both static and dynamic components. The exchange field is a dynamic field. The convention to use lower case letters to denote dynamic fields will be followed here. The separation of the various fields into static and dynamic terms will become clear from the nomenclature developed below.

The $\mathbf{H}_D$ term in Eq. (2.3) consists of a static term and two dynamic terms. The static term consists of a demagnetizing field of the form $-4\pi\mathbf{N}'\mathbf{M}_s$, where $\mathbf{N}'$ is the diagonal demagnetizing tensor in the $(X, Y, Z)$ laboratory frame of Fig. 2.1. For the ellipsoid sample inset of Fig. 2.1, the diagonal elements $\mathbf{N}'$ may be taken as $N'_{XX} = N_X$, $N'_{YY} = N_Y$, $N'_{ZZ} = N_Z$. The $N_X$, $N_Y$, and $N_Z$ denote the usual ellipsoidal sample demagnetizing factors. These demagnetizing factors will turn out to be important parameters in the theory. The first dynamic term is the dynamic demagnetizing field counterpart to the above static field, $-4\pi\mathbf{N}'\mathbf{m}_0$. The second dynamic term in $\mathbf{H}_D$ is the dipole field associated with the spin waves. In the short wave length limit, this field may be written as

$$\mathbf{h}_{\text{dip}} = -4\pi\sum_{k\neq 0}\frac{\mathbf{k}(\mathbf{k}\cdot\mathbf{m}_{\mathbf{k}})}{k^2}e^{i\mathbf{k}\cdot\mathbf{r}}. \tag{2.4}$$

Consider the effective non-Maxwellian anisotropy field. The components of $\mathbf{H}_A$ may be written as

$$H_{A,i} = -\frac{1}{M_s}\frac{\partial}{\partial\alpha_i}F_A = -\frac{\partial}{\partial M_i}F_A, \quad i = (X,\ Y,\ Z), \tag{2.5}$$

where $F_A(\alpha_X, \alpha_Y, \alpha_Z)$ defines a general anisotropy free energy (Gurevich and Melkov [1996]), and $\alpha_X$, $\alpha_Y$, and $\alpha_Z$ are the direction cosines of $\mathbf{M}$ relative to the $X$, $Y$, and $Z$ axes in Fig. 2.1, respectively. It is important to realize that the $\mathbf{M}$ vector itself consists of a static component $\mathbf{M}_s$, as in Fig. 2.1, and the additional dynamic component introduced above. If the condition $|\,\mathbf{m}\,| << |\,\mathbf{M}_s\,|$ is satisfied, the static and dynamic terms in $\mathbf{M}$, when folded into Eq. (2.5), lead to $\mathbf{H}_A$ components of the form

$$H_{A,i} = H_{A,i}(\mathbf{M}_s) + \sum_{j=1}^{3} \left. \frac{\partial H_{A,i}(\mathbf{M})}{\partial M_j} \right|_{\mathbf{M}=\mathbf{M}_s} m_j \,. \tag{2.6}$$

The first term on the right side of Eq. (2.6) corresponds to a *static* effective anisotropy field which depends only on the static $\mathbf{M}_s$ component of the magnetization. This vector field will be denoted as $\mathbf{H}_{AS}$. The second term represents the dynamic part of $\mathbf{H}_A$. This vector field will be denoted as $\mathbf{h}_A$. The field $\mathbf{h}_A$ has the form $\mathbf{A}'\mathbf{m}$, where $\mathbf{A}'$ is an anisotropy tensor with components given by

$$A'_{ij} = - \left. \frac{\partial^2 F_A(\mathbf{M})}{\partial M_i \partial M_j} \right|_{\mathbf{M}=\mathbf{M}_s} . \tag{2.7}$$

It is clear that $\mathbf{A}'$ is a symmetric tensor.

The only remaining field terms in Eq. (2.3) are the effective exchange field and the applied microwave field. The exchange field may be written as $|\gamma| D\nabla^2 \mathbf{m} / M_s$, where $|\gamma|$ is the absolute value of the electron gyromagnetic ratio and $D$ is the exchange stiffness field parameter (Gurevich and Melkov [1996]). Detailed nomenclature for the applied microwave field $\mathbf{h}$ will be introduced later.

From the effective fields established above, one may now separate the static and dynamic contributions to $\mathbf{H}_{eff}$. The static terms combine to yield a static effective field given by

$$\mathbf{H}_{eff}^{S} = \mathbf{H}_{ext} - 4\pi \mathbf{N}'\mathbf{M}_s + \mathbf{H}_{AS} \,. \tag{2.8}$$

This vector field will be a function of the various parameters established above and, in particular, the direction of $\mathbf{M}_s$. The magnetization $\mathbf{M}_s$ will be in static equilibrium when the condition

$$\mathbf{M}_s \times \mathbf{H}_{eff}^{S} = 0 \tag{2.9}$$

is satisfied, such that $\mathbf{M}_s$ and $\mathbf{H}_{\rm eff}^{\rm S}$ are collinear. The complete dynamic part of $\mathbf{H}_{\rm eff}$ may now be written as

$$\mathbf{h}_{\rm eff} = -4\pi\sum_{k\neq 0}\frac{\mathbf{k}(\mathbf{k}\cdot\mathbf{m}_\mathbf{k})}{k^2}e^{i\mathbf{kr}} - 4\pi\mathbf{N}'\mathbf{m}_0 + \mathbf{A}'\mathbf{m} + \frac{1}{M_s}|\gamma| D\nabla^2\mathbf{m} + \mathbf{h}\,. \tag{2.10}$$

The next part of this section will consider the dynamics of the magnetization in a new $(x, y, z)$ coordinate system for which the $z$-axis coincides with the direction of $\mathbf{M}_s$ under conditions of static equilibrium. In this new reference frame, termed the *precession frame*, the uniform mode part of the dynamic $\mathbf{m}$ response will correspond to a Larmor precession of $\mathbf{M}$ about the $z$-axis. The static effective field in this frame will have only a $z$-component. The total dynamic field in Eq. (2.10) will be transformed into this frame. This will result in a precession frame equation of motion for the dynamic magnetization, or torque equation, which leads to the nonlinear coupled equations which are needed for the analysis of spin wave instability.

Consider the simple rotational transformation in Fig. 2.2 from the $(X, Y, Z)$ laboratory frame to the $(x, y, z)$ precession frame. The angles $\theta_M$ and $\varphi_M$ are the same angles as introduced in Fig. 2.1 for static equilibrium. For this transformation, (1) the $X$-$Y$ plane is rotated about the $Z$-axis by the angle $\varphi_M$ and (2) a new $X_1$-$Z$ plane is rotated about a new $y$-axis by the angle $\theta_M$. The transformation of any general vector $\mathbf{R}$ in the laboratory frame to the corresponding vector $\mathbf{r}$ in the $(x, y, z)$ frame may be written in the form $\mathbf{r} = \mathbf{TR}$, where the $\mathbf{T}$ matrix is given by

$$\mathbf{T} = \begin{pmatrix} \cos\theta_M\cos\varphi_M & \cos\theta_M\sin\varphi_M & -\sin\theta_M \\ -\sin\varphi_M & \cos\varphi_M & 0 \\ \sin\theta_M\cos\varphi_M & \sin\theta_M\sin\varphi_M & \cos\theta_M \end{pmatrix}. \tag{2.11}$$

The transformation of the various vector fields and tensors enumerated above to the $(x, y, z)$ frame is straightforward. The elements of the demagnetizing tensor in the $(x, y, z)$ frame, $\mathbf{N} = \mathbf{T}\mathbf{N}'\mathbf{T}^{-1}$, are given by

$$N_{xx} = (N_X \cos^2 \varphi_M + N_Y \sin^2 \varphi_M)\cos^2 \theta_M + N_Z \sin^2 \theta_M, \tag{2.12}$$

$$N_{yy} = N_X \sin^2 \varphi_M + N_Y \cos^2 \varphi_M, \tag{2.13}$$

$$N_{zz} = (N_X \cos^2 \varphi_M + N_Y \sin^2 \varphi_M)\sin^2 \theta_M + N_Z \cos^2 \theta_M, \tag{2.14}$$

$$N_{xy} = N_{yx} = (N_Y - N_X)\cos\theta_M \sin(2\varphi_M)/2, \tag{2.15}$$

$$N_{xz} = N_{zx} = (N_X \cos^2 \varphi_M + N_Y \sin^2 \varphi_M - N_Z)\sin(2\theta_M)/2, \tag{2.16}$$

and

$$N_{yz} = N_{zy} = (N_Y - N_X)\sin\theta_M \sin(2\varphi_M)/2. \tag{2.17}$$

The static demagnetizing field in the $(x, y, z)$ frame is $-4\pi\mathbf{N}(M,\hat{\mathbf{z}})$, where $\hat{\mathbf{z}}$ is a unit vector in the $z$-direction. The dynamic demagnetizing field is given by $-4\pi\mathbf{N}\mathbf{m}_0$, where $\mathbf{m}_0$ is given in terms of $(x, y, z)$ frame components.

In the same way, one can obtain the effective anisotropy fields in the $(x, y, z)$ frame. The specific form of $\mathbf{H}_{AS}$ will depend on the form of the anisotropy energy $F_A$ and the angles $\theta_M$ and $\varphi_M$. The dynamic anisotropy field in the precession frame will be taken as

$$\mathbf{h}_A = \mathbf{A}\mathbf{m} = \mathbf{T}\mathbf{A}'\mathbf{T}^{-1}\mathbf{m} = \begin{pmatrix} A_{xx} & A_{xy} & A_{xz} \\ A_{xy} & A_{yy} & A_{yz} \\ A_{xz} & A_{yz} & A_{zz} \end{pmatrix} \begin{pmatrix} \mathbf{m}_x \\ \mathbf{m}_y \\ \mathbf{m}_z \end{pmatrix}. \tag{2.18}$$

Since $\mathbf{A}'$ is a symmetric tensor and $\mathbf{T}$ corresponds to a unitary transformation, the matrix $\mathbf{A}$ is also symmetric. The specific form of the elements of $\mathbf{A}$ will also depend on

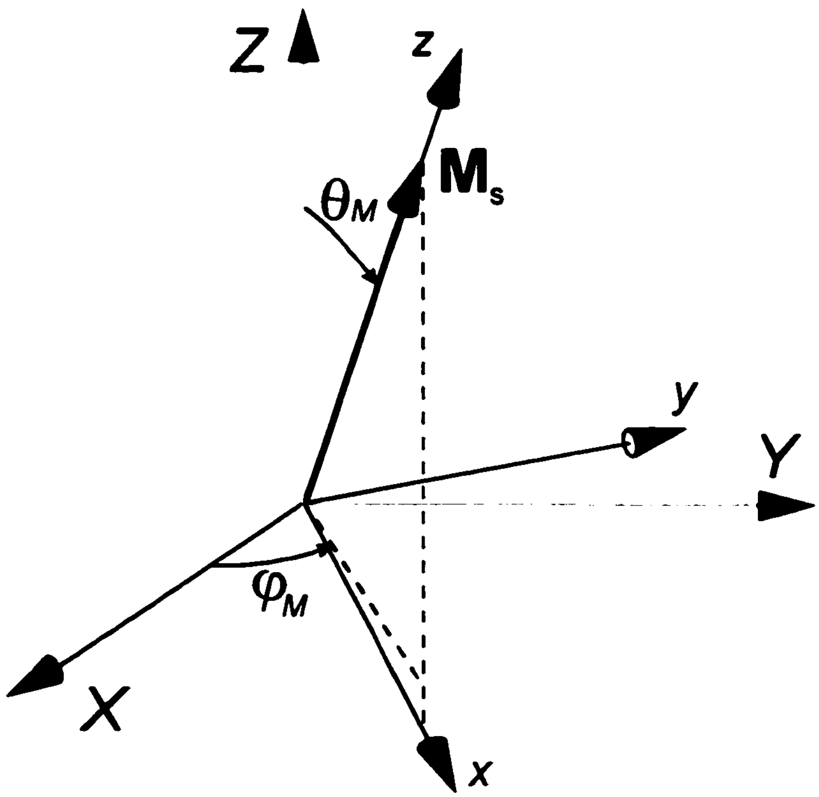


Figure 2.2. Transformation of the coordinate frame $(X, Y, Z)$ to the precession frame $(x, y, z)$. The $z$-axis coincides with the direction of the static magnetization $\mathbf{M}_s$. The static magnetization $\mathbf{M}_s$ lies at a polar angle $\theta_M$ and an azimuthal angle $\varphi_M$.

the form of the anisotropy energy $F_A$ and the static equilibrium magnetization angles $\theta_M$ and $\varphi_M$ which define the precession frame.

The exchange and dipole fields depend only on the dynamic magnetization **m**. The form of these fields is the same for the laboratory and the precession frames and the appropriate terms in Eq. (2.10) apply. The microwave field **h** may also be specified directly in the precession frame. The applied microwave field **h**($t$) is taken to be uniform over the ellipsoidal sample and with a general polarization. The components of this pumping field in the precession frame may be written as

$$h_x(t) = h_0\alpha_x \cos(\omega t + \delta_x) = h_0\alpha_x[e^{i(\omega t+\delta_x)} + e^{-i(\omega t+\delta_x)}]/2\,, \tag{2.19}$$

$$h_y(t) = h_0\alpha_y \cos(\omega t + \delta_y) = h_0\alpha_y[e^{i(\omega t+\delta_y)} + e^{-i(\omega t+\delta_y)}]/2\,, \tag{2.20}$$

and

$$h_z(t) = h_0\alpha_z \cos\omega t = h_0\alpha_z(e^{i\omega t} + e^{-i\omega t})/2\,. \tag{2.21}$$

The $h_0$ parameter serves to identify the amplitude of the pumping field. The relative amplitude parameters $\alpha_x$, $\alpha_y$, and $\alpha_z$, and the phase parameters $\delta_x$ and $\delta_y$ define the specific components of the pumping field in the $(x, y, z)$ precession frame.

Consider static equilibrium considerations. In the precession frame, the zero torque condition of Eq. (2.9) requires that the $x$ and $y$ components of $\mathbf{H}^{S}_{\mathrm{eff}}$ vanish. The corresponding equations then give the conditions on $\theta_M$ and $\varphi_M$ for static equilibrium. These conditions may be written as

$$\begin{aligned} &H_{\mathrm{ext}}[\sin\theta_H \cos\theta_M \cos(\varphi_H - \varphi_M) - \cos\theta_H \sin\theta_M] \\ &= 2\pi M_s(N_X \cos^2\varphi_M + N_Y \sin^2\varphi_M - N_Z)\sin 2\theta_M \\ &\quad + H_{AS,Z}\sin\theta_M - (H_{AS,X}\cos\varphi_M + H_{AS,Y}\sin\varphi_M)\cos\theta_M \end{aligned} \tag{2.22}$$

and

$$H_{ext}\sin\theta_H\sin(\varphi_M-\varphi_H)=H_{AS,Y}\cos\varphi_M-H_{AS,X}\sin\varphi_M$$

$$+2\pi M_s(N_X-N_Y)\sin 2\varphi_M\sin\theta_M\,. \tag{2.23}$$

The $H_{AS,X}$, $H_{AS,Y}$, and $H_{AS,Z}$ terms in Eqs. (2.22) and (2.23) give the components of $\mathbf{H}_{AS}$ in the laboratory frame. Note that Eqs. (2.22) and (2.23) are for a general anisotropy. The above equilibrium conditions define $\theta_M$ and $\varphi_M$ which set the precession frame. In this frame, the static effective field $\mathbf{H}_{eff}^S$ reduces to one component along $z$ which is given by

$$H_{eff}^S=H_{ext}\sin\theta_H\sin\theta_M\cos(\varphi_H-\varphi_M)+H_{ext}\cos\theta_H\cos\theta_M-4\pi M_s[N_Z\cos^2\theta_M$$

$$+(N_X\cos^2\varphi_M+N_Y\sin^2\varphi_M)\sin^2\theta_M]+(H_{AS,X}\cos\varphi_M+H_{AS,Y}\sin\varphi_M)\sin\theta_M$$

$$+H_{AS,Z}\cos\theta_M\,. \tag{2.24}$$

One now has expressions for all static and dynamic fields in the precession frame. The static effective field $\mathbf{H}_{eff}^S$ is parallel to $\mathbf{M}_s$ and along $z$. The dynamic magnetization $\mathbf{m}$ and the dynamic effective field $\mathbf{h}_{eff}$ will, in general have non-vanishing components along all three directions in the precession frame. Except for the external microwave field $\mathbf{h}$, the terms in $\mathbf{h}_{eff}$ all derive from $\mathbf{m}$ through Eq. (2.10) but expressed in the $(x,y,z)$ frame. It is convenient to write the transverse components of the dynamic magnetization and field in scalar complex form according to

$$m_\pm=m_x\pm im_y \tag{2.25}$$

and

$$h_{eff\pm}=h_{eff,x}\pm ih_{eff,y}\,, \tag{2.26}$$

where $h_{\mathrm{eff},x}$ and $h_{\mathrm{eff},y}$ denote the $x$ and $y$ components of $\mathbf{h}_{\mathrm{eff}}$, respectively. The constant magnetization condition $|\mathbf{M}| = M_s$ then leads to a dynamic magnetization $z$ component of the form

$$m_z = -(m_x^2 + m_y^2)/2M_s = -m_+m_-/2M_s. \tag{2.27}$$

Equation (2.27) is valid in the limit $|\mathbf{m}| << |\mathbf{M}_s|$ introduced above.

The next section will consider the magnetization equation of motion and introduce uniform precession and spin waves.

## 2.2. Uniform Mode and Spin Waves

Spin wave instability results from the analysis of the nonlinear terms in the torque equation of motion. In this section, only linear terms in torque equations will be considered. These linear terms lead to amplitudes for uniform precession of magnetization and spin waves. The torque equation of motion for the general magnetization vector $\mathbf{M}$ may be written as (Sparks [1964]),

$$\frac{d\mathbf{M}}{dt} = -|\gamma|\mathbf{M} \times \mathbf{H}_{\mathrm{eff}}. \tag{2.28}$$

The torque equation of motion was first proposed by Landau and Lifshitz [1935], based on the magnetic torque model. Based on the precession frame formulation of the dynamic magnetization and effective fields as given above, one can use Eq. (2.28) to obtain the equations of motion for the spin wave amplitudes. One does a plane wave Fourier expansion for the dynamic components of $\mathbf{M}$ in the precession frame. One then considers specific pairs of terms in this expansion for $\pm\mathbf{k}$, where $\mathbf{k}$ is a general spin wave

wave vector. Terms with $\mathbf{k} = 0$ correspond to the uniform mode. Such terms, when present, are connected with components of the microwave field which are transverse to the $z$-direction.

As a first step, one obtains expressions for $\dot{m}_+$ and $\dot{m}_-$ from Eq. (2.28). These may be written as

$$-i\dot{m}_+ = |\gamma| m_+ (H^S_{\mathrm{eff}} + h_{\mathrm{eff},z}) - |\gamma| (M_s + m_z) h_{\mathrm{eff}+} \tag{2.29}$$

and the corresponding equation for $\dot{m}_-$, where $h_{\mathrm{eff},z}$ denotes the $z$ component of $\mathbf{h}_{\mathrm{eff}}$. The $m_\pm$ variables are now expanded in Fourier series in the form

$$m_+ = M_s \sum_{\mathbf{k}} a_{\mathbf{k}} e^{i\mathbf{kr}} \tag{2.30}$$

and

$$m_- = M_s \sum_{\mathbf{k}} a^*_{-\mathbf{k}} e^{i\mathbf{kr}}. \tag{2.31}$$

The sums in Eqs. (2.30) and (2.31) specifically include the uniform mode at $\mathbf{k} = 0$ and $\mathbf{k} \neq 0$ terms which span the full range of allowed values for bulk spin waves. The nonzero $\mathbf{k}$ terms will be limited to the short wave length limit for which surface effects can be neglected. For convenience, the vector nomenclature for $\mathbf{k}$ will be dropped from subscripts from here on. Note that $a_0$ corresponds to a normalized complex uniform mode amplitude, while the $a_k$ factors with $\mathbf{k} \neq 0$ correspond to classical spin wave amplitudes (Sparks [1964]). Unless otherwise noted, references to $a_k$ will always imply the $\mathbf{k} \neq 0$ condition and $a_0$ will specifically denote the uniform mode.

The uniform microwave field introduced above produces a uniform mode response $\mathbf{m}_0$. Figure 2.3 shows the precessional motion of magnetization $\mathbf{M}$ about the internal effective magnetic field $\mathbf{H}_{\mathrm{eff}}$. Diagram (a) shows a free circular precession. Diagram (b)

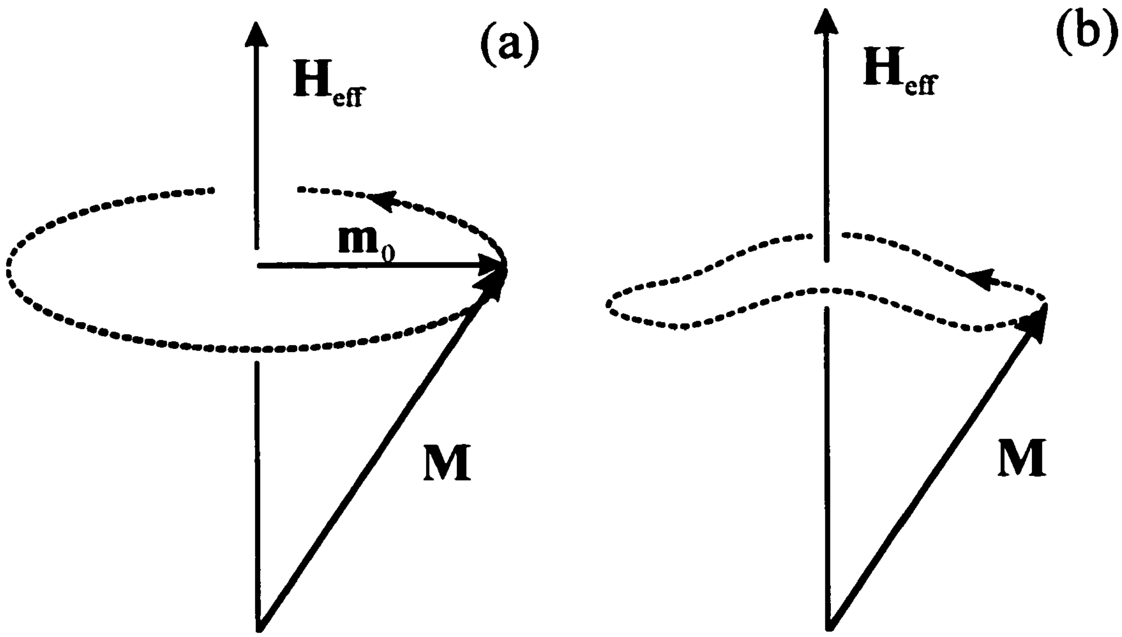


Figure 2.3. Uniform precession of the magnetization **M** about the internal magnetic field $\mathbf{H}_{eff}$. The static magnetization $\mathbf{M}_s$ is parallel to $\mathbf{H}_{eff}$. Diagram (a) is for circular uniform precession with the vector amplitude $\mathbf{m}_0$. Diagram (b) is for elliptical uniform precession when $\mathbf{m}_0$ varies with time.

shows an elliptical precession. The elliptical precession may be caused by a linear polarized applied microwave field, by anisotropy, and by a non-spherical sample shape. The undamped response may be evaluated from the torque equation, Eq. (2.28), with only linear terms in the dynamic variables taken into account. It will also be necessary to include the effects of damping, particularly for situations when one is operating close to ferromagnetic resonance. This will be accomplished by a complex frequency substitution technique. The result is a set of equations for the complex uniform mode amplitude $a_0$.

Based on the driving fields of Eqs. (2.19)-(2.21), one may obtain the undamped uniform mode response from the $x$ and $y$ components of the torque equation, Eq. (2.28), with only linear terms in the components of **h** and **m** included. For this analysis, **M** is taken as $M_s\hat{\mathbf{z}} + \mathbf{m}_0$ only, with all $\mathbf{k} \neq 0$ terms ignored, and $\mathbf{H}_{\text{eff}}$ is taken as

$$\mathbf{H}_{\text{eff}} = H_{\text{eff}}^{\text{S}}\hat{\mathbf{z}} - 4\pi\tilde{\mathbf{N}}\mathbf{m}_0 + \mathbf{h}. \qquad (2.32)$$

In the above expressions, $\tilde{N}_{ij} = N_{ij} - A_{ij}/4\pi$ correspond to reduced effective demagnetizing tensor elements. Equation (2.28) may now be cast in the same form as Eq. (2.29) with the $h_{\text{eff},z}$ and $m_z$ terms omitted and $h_{\text{eff}+}$ constructed from the $x$ and $y$ components of $\mathbf{h} - 4\pi\tilde{\mathbf{N}}\mathbf{m}_0$ only. The substitutions $m_+ = a_0 M_s$ and $m_- = a_0^* M_s$ then yield coupled equations for $a_0$ and $a_0^*$ given by

$$-i\dot{a}_0 = |\gamma| H_{\text{eff}}^{\text{S}} a_0 - |\gamma| h_\perp + \omega_M[(\tilde{N}_{xx} + \tilde{N}_{yy})a_0 + (\tilde{N}_{xx} + 2i\tilde{N}_{xy} - \tilde{N}_{yy})a_0^*]/2 \qquad (2.33)$$

and the companion complex conjugate. In Eq. (2.33), $h_\perp = h_x + ih_y$ expresses the transverse components of the external microwave field **h** in the same scalar complex form used above for the transverse magnetization and dynamic effective field and

$\omega_M = 4\pi|\gamma|M_s$ expresses the magnetic induction $4\pi M_s$ in frequency units. The solution of these coupled equations gives the complex uniform mode amplitude $a_0$,

$$a_0(t) = |\gamma| h_0 [q_{L0} \exp(i\omega t) + q_{A0} \exp(-i\omega t)]/2 . \tag{2.34}$$

The $q_{L0}$ and $q_{A0}$ factors are given by

$$q_{L0} = \frac{(\omega_y + \omega - i\omega_{xy})\alpha_x e^{i\delta_x} + i(\omega_x + \omega + i\omega_{xy})\alpha_y e^{i\delta_y}}{\omega_0^2 - \omega^2} \tag{2.35}$$

and

$$q_{A0} = \frac{(\omega_y - \omega - i\omega_{xy})\alpha_x e^{-i\delta_x} + i(\omega_x - \omega + i\omega_{xy})\alpha_y e^{-i\delta_y}}{\omega_0^2 - \omega^2} . \tag{2.36}$$

The frequency parameters $\omega_x$, $\omega_y$, and $\omega_{xy}$ are given by

$$\omega_x = |\gamma| H_{\mathrm{eff}}^{\mathrm{S}} + \omega_M \tilde{N}_{xx}, \tag{2.37}$$

$$\omega_y = |\gamma| H_{\mathrm{eff}}^{\mathrm{S}} + \omega_M \tilde{N}_{yy}, \tag{2.38}$$

and

$$\omega_{xy} = \omega_M \tilde{N}_{xy} . \tag{2.39}$$

The $\omega_0$ frequency parameter corresponds to the ferromagnetic resonance (FMR) frequency and is given by

$$\omega_0 = \sqrt{\omega_x \omega_y - \omega_{xy}^2} . \tag{2.40}$$

The $|\gamma| h_0 q_{L0}/2$ and $|\gamma| h_0 q_{A0}/2$ multipliers in Eq. (2.34) represent the Larmor and anti-Larmor amplitudes for the uniform mode. These amplitudes scale linearly with the pumping field amplitude $h_0$.

Note the singularities in the $a_0$ response in Eqs. (2.34)-(2.36) in the limit $\omega \to \omega_0$. This is due to the neglect of damping. Damping must be included in the analysis in order to describe properly the $a_0$ response, particularly when the pumping frequency $\omega$ is close to the FMR frequency $\omega_0$. The effect of uniform mode damping will turn out to have an important effect on the instability analysis, especially for second order processes.

There are various ways in which damping may be included in the uniform mode response (Gurevich and Melkov [1996]). In the next section, spin wave damping will be taken into account through a complex frequency substitution, $\omega_k \to \omega_k + i\eta_k$. A similar procedure will be followed here for the uniform mode frequency (Schlömann *et al.* [1963]). This substitution may be written as

$$\omega_0 \to \omega_0 + i\Delta\omega_0 / 2, \tag{2.41}$$

where $\Delta\omega_0$ is a frequency swept FMR linewidth parameter. For narrow linewidth materials, specific values for $\Delta\omega_0$ may be obtained from measurements of the FMR field swept linewidth $\Delta H_0$ according to (Hurben [1996])

$$\Delta\omega_0 = \frac{\partial\omega_0}{\partial H_{ext}} \Delta H_0 . \tag{2.42}$$

The formalism developed above provides working equations for the uniform mode amplitude $a_0$ for a general pumping field applied to an ellipsoidal sample with a general anisotropy.

Consider now bulk spin waves with non-zero **k**. Direct substitution of the various field terms developed above into Eq. (2.29) and the corresponding $\dot{m}_-$ equation, along with the expressions for $m_+$, $m_-$, and $m_z$, yields a set of nonlinear coupled equations for the $a_k$ and $a^*_{-k}$ spin wave amplitudes. In order to provide a more tutorial approach, equations for spin wave amplitudes will be first written without nonlinear terms. These linear equations are given by

$$-i\dot{a}_k = A_k a_k + B_k a^*_{-k} \tag{2.43}$$

and the companion complex conjugate equation with $\mathbf{k}$ replaced by $-\mathbf{k}$. The coefficients $A_k$ and $B_k$ are given by

$$A_k = |\gamma|[H^S_{\text{eff}} + Dk^2 - M_s(A_{xx} + A_{yy})/2] + \omega_M(\sin^2\theta_k)/2 \tag{2.44}$$

and

$$B_k = \omega_M \sin^2\theta_k \exp(2i\varphi_k)/2 - |\gamma| M_s(A_{xx} - A_{yy} + 2iA_{xy})/2. \tag{2.45}$$

In the above expressions, $\theta_k$ and $\varphi_k$ are the standard polar and azimuthal angles of the spin wave wave vector in the $(x, y, z)$ precession frame, respectively.

Equation (2.43) and its companion equation yield the bulk spin wave dispersion relation. Note that Eq. (2.43) is non-diagonal. The standard way to diagonalize the linear terms in Eq. (2.43) and obtain the spin wave normal modes is through the Holstein Primakoff (HP) transformation (Sparks [1964]). In terms of the parameters established above, one may transform the $a_k$ and $a^*_{-k}$ to a new set of spin wave amplitudes $b_k$ and $b^*_{-k}$ according to

$$a_k = \lambda_k b_k - \mu_k b^*_{-k} \tag{2.46}$$

and

$$a^*_{-k} = \lambda_k b^*_{-k} - \mu^*_k b_{-k}, \tag{2.47}$$

with transformation coefficients given by

$$\lambda_k = \sqrt{\frac{A_k + \omega_k}{2\omega_k}} \tag{2.48}$$

and

$$\mu_k = \sqrt{\frac{A_k - \omega_k}{2\omega_k}} \frac{B_k}{|B_k|}. \tag{2.49}$$

The $\omega_k$ term in Eqs. (2.48) and (2.49) is the usual bulk spin wave frequency $\omega_k$ given by

$$\omega_k = \sqrt{A_k^{\,2} - |B_k|^2} \tag{2.50}$$

Through this transformation, the linear terms in Eq. (2.43) yield a simple harmonic oscillator response equation of the form $-i\dot{b}_k = \omega_k b_k$. The spin wave dispersion relation in Eq. (2.50) gives rise to the usual spin wave band of allowed excitations discussed by Sparks [1964] and others. The present result, when all anisotropy terms are included, gives a general spin wave dispersion for anisotropic ferrites. Special cases have been considered elsewhere (Patton [1979] and Hurben and Patton [1998]). Another interesting and important situation occurs in thin magnetic films, where the spin wave dispersion is modified by boundary conditions for low wave number spin waves and additional surface modes appear (Stancil [1993] and Kalinikos *et al.* [1990]).

In the next section the equation for spin wave amplitudes will be written with nonlinear terms. These non-linear terms in the torque equation of motion will lead to the condition of spin wave instability.

## 2.3. Spin Wave Instability

Direct substitution of the various field terms developed in Section 2.1 into Eq. (2.29) and the corresponding $\dot{m}_-$ equation, along with the expressions for $m_+$, $m_-$, and $m_z$, yields a set of nonlinear coupled equations for the $a_k$ and $a^*_{-k}$ spin wave amplitudes. Following Suhl [1957], one may obtain the working equations for the spin wave instability analysis by retaining only linear terms in the $a_k$ and $a^*_{-k}$ amplitudes and terms up to second order in $a_0$ and $a_0^*$. This procedure is valid if the condition $|a_k| \ll |a_0| \ll 1$ is satisfied. A fairly tedious algebraic analysis yields general spin wave amplitude equations given by

$$-i\dot{a}_k = (A_k + C_k)a_k + (B_k + D_k)a_{-k}^* + |\gamma|h_z a_k \tag{2.51}$$

and the companion complex conjugate equation with **k** replaced by $-\mathbf{k}$. The coefficients $C_k$ and $D_k$ are given by

$$\begin{aligned}
C_k = &-\omega_M \sin 2\theta_k [a_0 \exp(-i\varphi_k) + a_0^* \exp(i\varphi_k)]/4 \\
&+[|\gamma| M_s (A_{zx} - iA_{zy}) - \omega_M (\tilde{N}_{zx} - i\tilde{N}_{zy})]a_0/2 \\
&+[|\gamma| M_s (A_{zx} + iA_{zy}) - \omega_M (\tilde{N}_{zx} + i\tilde{N}_{zy})]a_0^*/2 \\
&+|\gamma| h_\perp a_0^*/2 + |\gamma| M_0 (A_{xx} + A_{yy} - 2A_{zz}) a_0 a_0^*/4 \\
&+\omega_M (2\tilde{N}_{zz} - \tilde{N}_{xx} - \tilde{N}_{yy} + 3\cos^2\theta_k - 1)a_0 - \omega_M (\tilde{N}_{xx} + 2i\tilde{N}_{xy} - \tilde{N}_{yy}) a_0^* a_0^*
\end{aligned} \tag{2.52}$$

and

$$\begin{aligned}
D_k = &[-\omega_M \sin 2\theta_k \exp(i\varphi_k)/2 + |\gamma| M_s (A_{zx} + iA_{zy})]a_0 \\
&+|\gamma| h_\perp a_0 - \omega_M \sin^2\theta_k \exp(2i\varphi_k) a_0 a_0^*/4 - \omega_M (\tilde{N}_{xx} + 2i\tilde{N}_{xy} - \tilde{N}_{yy}) a_0 a_0^*/4 \\
&+|\gamma| M_s (A_{xx} + 2iA_{xy} - A_{yy}) a_0 a_0^*/4 + \omega_M (2\cos^2\theta_k - \tilde{N}_{xx} - \tilde{N}_{yy}) a_0 a_0/4 \\
&+|\gamma| (Dk^2 - M_s A_{zz}) a_0 a_0/2\,.
\end{aligned} \tag{2.53}$$

Equation (2.51) and its companion equation are the working equations for the first and second order spin wave instability threshold analysis. The coefficients $A_k$ and $B_k$ contain only materials parameters and the spin wave wave vector **k**. If only these right side terms are considered, Eq. (2.51) yields the bulk spin wave dispersion relation of Eq.

(2.50). The remaining right side terms involve the external microwave field, either explicitly or implicitly through uniform mode $a_0$ factors. These terms lead to spin wave instability. The details of the above procedures are well established (Sparks [1964]).

The key step in the Suhl analysis is now to apply the *same* HP transformation defined in Section 2.2 to the *nonlinear* as well as the *linear* terms in Eq. (2.51). This step changes Eq. (2.51) to the form

$$-i\dot{b}_k = \omega_k b_k + F_k b_k + G_k b^*_{-k}, \tag{2.54}$$

with corresponding changes to the companion equation. The $F_k$ and $G_k$ functions are given by

$$F_k = \lambda_k^2(|\gamma|h_z + C_k) + |\mu_k|^2(|\gamma|h_z^* + C_k^*) - \lambda_k(D_k\mu_k^* + \mu_k D_k^*) \tag{2.55}$$

and

$$G_k = \lambda_k^2 D_k + \mu_k^2 D_k^* - \lambda_k\mu_k(|\gamma|h_z + |\gamma|h_z^* + C_k + C_k^*). \tag{2.56}$$

Note that all terms in both $F_k$ and $G_k$ terms in Eq. (2.54) contain factors related to the microwave driving field, either directly in terms of explicit components of **h** or indirectly in terms of the uniform mode $a_0$ factors. Refer to Eqs. (2.52) and (2.53).

The transformation of the nonlinear terms in Eq. (2.51) modifies the $-i\dot{b}_k = \omega_k b_k$ equation in two important ways. First, the $F_k$ factor adds a complicated modulation to the spin wave frequency. Second, the coefficient $G_k$ provides a coupling between the $b_k$ and $b^*_{-k}$ modes. Parallel comments apply to the companion equation. These modifications relate to the well known problem of coupled harmonic oscillators (Gurevich and Melkov [1996]). A modulation in the coupling coefficient can lead to the transfer of energy from the source of the modulation to the coupled oscillators. In the present case, the $G_k$ factor represents this coupling and the energy which is coupled into the $b_k$ and $b^*_{-k}$ modes is the source of spin wave instability in the Suhl analysis. Above some critical microwave field amplitude, one finds an abrupt increase in the $b_k$ and $b^*_{-k}$ amplitudes. The $F_k$ factor leads only to a small modulation in the spin wave frequency. For this reason, the $F_k$ modulation term is omitted from the Suhl instability analysis.

It is important to realize that the terms in Eq. (2.56) contain harmonic factors of the form $e^{in\omega t}$ with $n$ values from -2 to 2, including zero. In order to make these harmonic terms explicit, $G_k$ may be cast in the form (Schlömann [1959])

$$G_k = \sum_{-2}^{2} G_k^{(n)} e^{in\omega t}. \tag{2.57}$$

As the analysis will show, the $n = 1$ and $n = 2$ terms lead to first order instability processes for spin waves at $\omega_k = \omega/2$ and second order processes at $\omega_k = \omega$, respectively. The label "first order" relates to the fact that the $e^{i\omega t}$ terms are associated with $h$ and $a_0$ factors to the first power. The term "second order" relates to combinations of these factors to the second power.

The next step in the analysis is to consider the $b_k$ equation of motion from Eq. (2.54) with $F_k$ set to zero and $G_k$ replaced by one $n$ term only from Eq. (2.57). It may be easily shown that the corresponding coupled equations of motion for $b_k$ and $b^*_{-k}$,

$$-i\dot{b}_k = \omega_k b_k + G_k^{(n)} b^*_{-k} \tag{2.58}$$

and

$$i\dot{b}^*_{-k} = \omega_k b^*_{-k} + (G_{-k}^{(n)})^* b_k, \tag{2.59}$$

have solutions which may be written in the form

$$b_k = b_{k0}^{n} e^{in\omega t/2}. \tag{2.60}$$

One then obtains the conditions for spin wave instability by examining the conditions for an unstable growth in the $b_{k0}^{n}$ amplitudes. This will correspond to the threshold for spin wave instability.

A simple but critical step in the above procedure is to introduce relaxation for the $b_k$ amplitudes. Following Schlömann [1959], such relaxation is included through the replacement $\omega_k \rightarrow \omega_k + i\eta_k$ in Eqs. (2.58) and (2.59), where $\eta_k$ corresponds to a spin wave relaxation rate. This modification in Eqs. (2.58) and (2.59), along with the substitution from Eq. (2.60), gives a second order differential equation for the $b_{k0}^{n}$,

$$\left[\frac{d^2}{dt^2} + 2\eta_k \frac{d}{dt} - \left|G_k^{(n)}\right|^2 + \left(\omega_k - \frac{n\omega}{2}\right)^2 + \eta_k^2\right] b_{k0}^{n} = 0. \tag{2.61}$$

Equation (2.61) has a simple algebraic solution of the form $b_{k0}^{n} \propto e^{\kappa t}$, with $\kappa$ given by

$$\kappa = -\eta_k + \sqrt{\left|G_k^{(n)}\right|^2 - (\omega_k - n\omega/2)^2}. \tag{2.62}$$

The increment parameter $\kappa$ determines the instability condition for the $b_k$ amplitudes. Keep in mind that the $b_k$ correspond to particular pairs of spin waves defined by $\omega_k$ and $\mathbf{k}$.

For $\kappa > 0$, the $b_{k0}^{n}$ will grow exponentially with time. This corresponds to unstable spin wave growth. For a given index $n$, therefore, spin wave instability can occur only if $G_k^{(n)}$ satisfies the condition

$$\left|G_k^{(n)}\right|^2 > (\omega_k - n\omega/2)^2 + \eta_k^2. \tag{2.63}$$

Keep in mind that the control parameter throughout the entire instability analysis is the $G_k$ coupling coefficient. Recall also that $G_k$ ultimately involves terms which scale with the microwave field and is controlled by the microwave power level at the sample. An equal sign in place of the ">" in Eq. (2.63) will define the spin wave instability threshold microwave field for a given index $n$ and the corresponding spin wave pair at $\omega_k$ and $\pm\mathbf{k}$.

Measurements of the threshold microwave field amplitude for spin wave instability are often used in conjunction with Eq. (2.63) to obtain empirical values for the spin wave relaxation rate $\eta_k$. This relaxation rate is often expressed in terms of an equivalent spin wave linewidth

$$\Delta H_k = 2\eta_k / |\gamma|. \tag{2.64}$$

Such a spin wave linewidth parameter is useful for comparison with ferromagnetic resonance linewidths in the ferrite sample.

Equation (2.63) constitutes the working equation for the determination of the spin wave instability threshold microwave field amplitude $h_{crit}$ for a given material, sample shape and orientation, static field, and microwave field polarization. The procedure is to examine all possible thresholds based on Eq. (2.63) and the available spin waves at a given $\omega_k$, identify that particular $(\omega_k, \pm\mathbf{k})$ mode pair with the lowest threshold as the critical mode, and assign that minimum threshold value as $h_{crit}$.

The first step in this procedure is to note that the relaxation rate $\eta_k$ is typically much less than $\omega_k$ and the minimum threshold will be obtained only for $\omega_k - n\omega/2 = 0$. This condition can be satisfied only for $n = 1$, with $\omega_k$ *equal to one half* the pumping frequency $\omega$, or for $n = 2$, with $\omega_k$ *equal to* $\omega$. These two cases correspond to the first and second order processes introduced in the discussion following Eq. (2.57) and the expansion of the general $G_k$ function into harmonic terms.

Under these conditions, the working equation for spin wave instability threshold determinations becomes $|G_k^{(n)}| = \eta_k$ for $n$ = 1 or $n$ = 2, only. This working equation, moreover, has a simple interpretation. For $n$ = 1, $|G_k^{(1)}| = \eta_k$ gives the spin wave specific threshold $h_c^{(1)}(\omega_k = \omega/2, \mathbf{k})$ for first order processes. For $n$ = 2, $|G_k^{(2)}| = \eta_k$ gives the spin wave specific threshold $h_c^{(2)}(\omega_k = \omega, \mathbf{k})$ for second order processes. The second and final step in the procedure to obtain $h_{\text{crit}}$ is to seek the minimum $h_c^{(1)}$ or $h_c^{(2)}$ over all available spin wave states at $\omega_k = \omega/2$ or $\omega_k = \omega$, respectively. The immediate task at hand, therefore, is to examine the various harmonic terms in $G_k$ and obtain explicit expressions for $G_k^{(1)}$ and $G_k^{(2)}$. Inspection of Eqs. (2.52), (2.53), and (2.56) shows that all harmonic time dependencies for $G_k$ are contained in the scalar complex uniform mode amplitude $a_0$ and the $z$-component of the applied microwave field $h_z$.

Consider first order processes. A convenient working equation for the spin wave specific threshold field $h_c^{(1)}(\omega_k = \omega/2, \mathbf{k})$ may be obtained by writing $h_c^{(1)}$ as the ratio of the spin wave linewidth $\Delta H_k$ and a dimensionless coupling parameter $Y_k^{(1)}$ according to

$$h_c^{(1)} = \frac{\Delta H_k}{\left|Y_k^{(1)}\right|}. \tag{2.65}$$

The development above yields a $Y_k^{(1)}$ function which may be written as

$$Y_k^{(1)} = [\lambda_k^2 q_{\text{L0}} d_k + \mu_k^2 q_{\text{A0}}^* d_k^* - \lambda_k \mu_k (2\alpha_z + q_{\text{L0}} c_k + q_{\text{A0}}^* c_k^*)], \tag{2.66}$$

with the coefficients $c_k$ and $d_k$ given by

$$c_k = -\omega_M (\sin 2\theta_k e^{-i\varphi_k}/2 + \tilde{N}_{zx} - i\tilde{N}_{zy}) + |\gamma| M_s (A_{zx} - iA_{zy}) \tag{2.67}$$

and

$$d_k = -\omega_M \sin 2\theta_k e^{i\varphi_k}/2 + |\gamma| M_s (A_{zx} + iA_{zy}). \tag{2.68}$$

Note that the $\lambda_k$, $\mu_k$, and $a_z$ parameters are dimensionless, the $q_{\mathrm{L0}}$ and $q_{\mathrm{A0}}$ have dimensions of inverse frequency, and the $c_k$ and $d_k$ have dimensions of frequency. As considered below, $|Y_k^{(1)}|$ reduces to the simple limiting case first order threshold expressions obtained by Suhl and Schlömann for isotropic ellipsoids of revolution and pure transverse Larmor or parallel pumping.

In a similar way, the spin wave specific threshold field $h_c^{(2)}(\omega_k = \omega, \mathbf{k})$ for second order processes may be written in the form

$$h_c^{(2)} = 2\sqrt{\frac{4\pi M_s \Delta H_k}{|Y_k^{(2)}|}}, \tag{2.69}$$

where $Y_k^{(2)}$ is a dimensionless coupling factor defined by

$$\begin{aligned} Y_k^{(2)} = {} & \omega_M \lambda_k^2 [q_{\mathrm{L0}}^2 f_k + q_{\mathrm{L0}} q_{\mathrm{A0}}^* g_k + q_{\mathrm{L0}}(\alpha_x e^{i\delta_x} + i\alpha_y e^{i\delta_y})] \\ & + \omega_M \mu_k^2 [q_{\mathrm{A0}}^{*2} f_k + q_{\mathrm{L0}} q_{\mathrm{A0}}^* g_k^* + q_{\mathrm{A0}}^* (\alpha_x e^{i\delta_x} - i\alpha_y e^{i\delta_y})] \\ & - \omega_M \lambda_k \mu_k [2 r_k q_{\mathrm{L0}} q_{\mathrm{A0}}^* + s q_{\mathrm{L0}}^2 + s^* q_{\mathrm{A0}}^{*2} \\ & + q_{\mathrm{A0}}^* (\alpha_x e^{i\delta_x} + i\alpha_y e^{i\delta_y}) + q_{\mathrm{L0}}(\alpha_x e^{i\delta_x} - i\alpha_y e^{i\delta_y})]. \end{aligned} \tag{2.70}$$

The as yet undefined coefficients are given by

$$f_k = |\gamma| D k^2 + \omega_M \cos^2\theta_k - |\gamma| M_s A_{zz} - \omega_M (\tilde{N}_{xx} + \tilde{N}_{yy})/2, \tag{2.71}$$

$$g_k = -\omega_M (\tilde{N}_{xx} + 2i\tilde{N}_{xy} - \tilde{N}_{yy} + \sin^2\theta_k e^{2i\phi_k})/2 + |\gamma| M_s (A_{xx} + 2iA_{yx} - A_{yy})/2, \tag{2.72}$$

$$\begin{aligned} r_k = {} & \omega_M \cos^2\theta_k + \omega_M \tilde{N}_{zz} + |\gamma| M_s (A_{xx} + A_{yy})/2 \\ & - |\gamma| M_s A_{zz} - \omega_M (\tilde{N}_{xx} + \tilde{N}_{yy} + \sin^2\theta_k)/2, \end{aligned} \tag{2.73}$$

and

$$s = -\omega_M (\tilde{N}_{xx} - 2i\tilde{N}_{xy} - \tilde{N}_{yy})/2. \tag{2.74}$$

The $f_k$, $g_k$, $r_k$, and $s$ have dimensions of frequency. As considered below, $|Y_k^{(2)}|$ reduces to the simple limiting case second order threshold expression obtained by Suhl for isotropic ellipsoids of revolution and pure transverse Larmor pumping.

The results contained in Eqs. (2.65) through (2.74) give the first completely general formulation of the first and second order threshold problem for a general anisotropy, a general microwave field configuration, a general ellipsoidal sample shape, and a non-collinear magnetization-field condition. This general result follows from application of the traditional spin wave instability analysis of Suhl and Schlömann almost verbatim, but with an effective field formulation based on the free energy considerations and the precession frame transformation procedure of Section 2.1.

All that remains is to examine the range of available spin wave wave vectors at $\omega_k = \omega / 2$ for first order processes or at $\omega_k = \omega$ for second order processes, and determine the lowest value of $h_c^{(1)}(\omega_k = \omega/2, \mathbf{k})$ or $h_c^{(2)}(\omega_k = \omega, \mathbf{k})$ for the available states, and obtain $h_{\mathrm{crit}}$. The hardest part of this analysis often turns out to be in setting up the minimization procedure over the available spin wave $\mathbf{k}$ states. This can be particularly challenging when the anisotropy has a significant effect on the spin wave dispersion relation of Eq. (2.50). The details of such minimization can be cogently discussed only within the context of a specific material and geometry. A demonstration example is given in the next section.

As emphasized above, the formulation given here is general. The specific working equations, however, have been set up in a way which facilitates the inspection of the results in special cases which correspond to the original results of Suhl and Schlömann.

For parallel pumping in isotropic ferrites, for example, the first order threshold equations given above reduce to

$$\left|Y_k^{(1)}\right| = 2\lambda_k \left|\mu_k\right| a_z = \left|B_k\right| / \omega_k = \omega_m \sin^2\theta_k / \omega . \tag{2.75}$$

This $\left|Y_k^{(1)}\right|$, in combination with Eq. (2.65), yields the well-known parallel pumping threshold $h_{crit} = \omega \Delta H_k / \omega_M$ with the critical modes at $\theta_k = 90^\circ$ (Schlömann *et al.* [1960]).

## 2.4. Demonstration calculation - first order thresholds for an easy plane ferrite disk.

This section supplements the previous general development by way of a specific example. The system considered is a thin disk with an easy plane anisotropy which coincides with the disk plane. The numerical evaluations are done for parameters applicable to Zn-Y, a Y-type hexagonal ferrite with planar anisotropy (Cox *et al.* [2001]). Only first order processes are considered. The results will be presented in the form of curves of the spin wave instability threshold field $h_{crit}$ as a function of $H_{ext}$, along with curves of the corresponding critical mode spin wave wave number $k$ and polar angle $\theta_k$ as a function of $H_{ext}$. The experimental data for this example will be shown in Chapter 6.

The geometry of the problem is shown in Fig. 2.4. The disk is in the $X$-$Y$ plane of the $(X, Y, Z)$ laboratory frame. The $X$-$Y$ plane is also the easy plane for the Zn-Y sample, and the $Z$-axis corresponds to the hexagonal $c$ axis. The field $\mathbf{H}_{ext}$ is in the $Y$-$Z$ plane and at an angle $\theta_H$ to the $Z$-axis. The magnetization $\mathbf{M}_s$ is in the $Y$-$Z$ plane and at an angle $\theta_M$ to the $Z$-axis. The linearly polarized microwave field $\mathbf{h}(t)$ is along $Y$. The figure shows a disk of finite extent and nonzero thickness. For simplicity, the disk demagnetizing

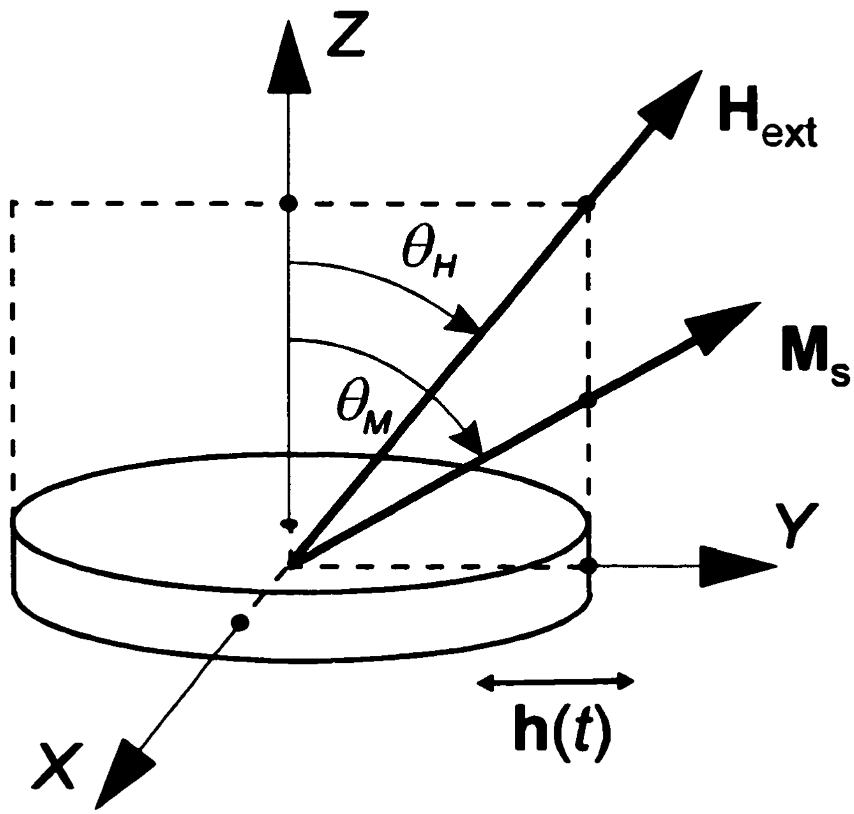


Figure 2.4. Geometry for the easy plane disk threshold analysis. The disk is in the $X$-$Y$ plane of the $(X, Y, Z)$ laboratory frame. The external static field $\mathbf{H}_{ext}$ is in the $Y$-$Z$ plane at an angle $\theta_H$ relative to $Z$. The static magnetization $\mathbf{M}_s$ is in the $Y$-$Z$ plane at an angle $\theta_M$ relative to $Z$. The linearly polarized microwave field $\mathbf{h}(t)$ is along $Y$.

factors will be set at $N_X = N_Y = 0$ and $N_Z = 1$. This corresponds to a disk diameter which is very large compared to the thickness. The microwave field **h**(t) will be taken to be uniform over the disk.

The easy plane anisotropy may be characterized in terms of an energy density function of the form

$$F_A = -K_U \cos^2\theta_M = -K_U M_Z^2 / M_s^2 . \tag{2.76}$$

where $K_U$ is an anisotropy parameter. For this anisotropy, the anisotropy field $\mathbf{H}_A$ defined in Eq. (2.5) has only one non-zero component, $H_{A,Z} = H_A \cos\theta_M$, where $H_A = 2K_U / M_s$ is a scalar anisotropy field parameter. For easy-plane Zn–Y, $K_U$ and $H_A$ are negative.

For planar anisotropy and the geometry of Fig. 2.4, it is clear that $\mathbf{M_s}$ will lie in the plane defined by $\mathbf{H}_{ext}$ and the $Z$-axis, with the azimuthal angles $\varphi_M$ and $\varphi_H$ in Fig. 2.1 equal to $\pi/2$. For the analysis below, the field $H_{ext}$ and the polar field angle $\theta_H$ will be the control parameters. As either of these field parameters is changed, the polar angle $\theta_M$ will also change. For each $(H_{ext}, \theta_H)$ combination, $\theta_M$ will be obtained from the static equilibrium condition of Eq. (2.22). For this example, Eq. (2.22) reduces to

$$H_{ext}\sin(\theta_H - \theta_M) = (H_A - 4\pi M_s)\sin(2\theta_M)/2 . \tag{2.77}$$

The equilibrium $\theta_M$ value then establishes the specific precession frame geometry discussed in Section 2.1 and the associated tensor components of the demagnetizing tensor **N** and the anisotropy tensor **A** in the precession frame. The components of **N** follow from Eqs. (2.12)-(2.17). For the geometry of Fig. 2.4, the only non-zero **N** components are $N_{xx} = N_Z \sin^2\theta_M$, $N_{xz} = N_{zx} = -N_Z \sin 2\theta_M / 2$, and $N_{zz} = N_Z \cos^2\theta_M$.

The components of the anisotropy tensor **A** follow from Eqs. (2.7), (2.11), and (2.18). For an anisotropy energy function $F_A$ of the form in Eq. (2.76) and a $\theta_M$ which satisfies the static equilibrium condition for a given $(H_{ext}, \theta_H)$ pair, the laboratory frame anisotropy tensor **A'** defined by Eq. (2.7) has only one non-zero component, $A'_{ZZ} = H_A / M_s$. The corresponding non-zero components of the precession frame anisotropy tensor **A** are $A_{xx} = H_A \sin^2\theta_M / M_s$, $A_{xz} = A_{zx} = -H_A \sin 2\theta_M / 2M_s$, and $A_{zz} = H_A \cos^2\theta_M / M_s$.

For the threshold evaluations, the microwave field is taken to have the explicit form $\mathbf{h}(t) = h_0 \cos(\omega t)\hat{\mathbf{Y}}$. The corresponding microwave field in the precession frame is then given by Eqs. (2.19)-(2.21) with $\alpha_x = \cos\theta_M$, $\alpha_z = \sin\theta_M$, and the remaining parameters $\alpha_y$, $\delta_x$, and $\delta_y$ set to zero.

Based on the above expressions, one can now construct explicit formulae for the static effective field $H^S_{eff}$, the spin wave dispersion relation $\omega_k(k, \theta_k, \varphi_k)$, the uniform mode response functions $q_{L0}$ and $q_{A0}$, and the first order coupling parameter $Y_k^{(1)}$ of Eq. (2.66). Based on these formulae, one may set up a suitable scan over available spin wave states at $\omega_k = \omega/2$, and determine the minimum threshold $h_{crit}$ and the corresponding $(k, \theta_k, \varphi_k)$ critical mode parameters for first order processes. If desired, one could follow a similar procedure for second order processes, based on $Y_k^{(2)}$ and a scan over available spin wave states at $\omega_k = \omega$.

The most challenging step in the above threshold calculation procedure is the set up of an appropriate scan over the available spin wave states. In the general case, one may construct a suitable scan in a purely mathematical way, based on the full ranges of $0 - \pi$

for $\theta_k$ and $0-2\pi$ for $\varphi_k$, and the requirement that $k$ be limited to real values. In any event, one calculates the threshold $h_c^{(1)}(\omega_k = \omega/2, \mathbf{k})$ or $h_c^{(2)}(\omega_k = \omega, \mathbf{k})$ for the full range of allowed $\mathbf{k}$ values, picks the minimum threshold value as $h_{crit}$ and the corresponding $(k, \theta_k, \varphi_k)$ critical mode. Note that $+\mathbf{k}$ and $-\mathbf{k}$ spin waves correspond to $(k, \theta_k, \varphi_k)$ and $(k, \pi-\theta_k, \pi+\varphi_k)$ spin waves, respectively, and these modes give the same threshold $h_{crit}$. For convenience, only critical modes with $\theta_k$ in the range $0-\pi/2$ were taken into account.

The above procedure was used to obtain explicit numerical values for $h_c^{(1)}$ over the full range of available spin wave states and then evaluate $h_{crit}$. This was done for a range of applied fields and field angles. These numerical results were then used to construct curves of $h_{crit}$ vs. $H_{ext}$ with $\theta_H$ as a control parameter. For these evaluations, $H_A$ was set at -9.0 kOe, $4\pi M_S$ was set at 2800 G, $|\gamma|$ was set to the free electron value of $1.76\times10^7$ rad/s·Oe, $\omega/2\pi$ was set at 17 GHz, the exchange constant $D$ was set to $5\times10^{-9}$ Oe·cm$^2$/rad$^2$, and $\Delta H_k$ was set at 1 Oe. The chosen $D$ value is for yttrium iron garnet. There is no reliable reported $D$ value in the literature for Zn–Y.

Figure 2.5 shows selected results from the numerical evaluations. Graph (a) gives $h_{crit}$ vs. $H_{ext}$ for $\theta_H$ values of 90°, 10°, and 5°. Graphs (b) and (c) give corresponding results on the critical mode spin wave wave number $k$ and polar angle $\theta_k$ as a function of $H_{ext}$. For $\theta_H$ = 90°, the critical mode azimuthal spin wave angle $\varphi_k$ was double valued at zero or 180°. For any $\theta_H$ value below 90°, the minimum threshold critical mode $\varphi_k$ was *single valued* at 180°.

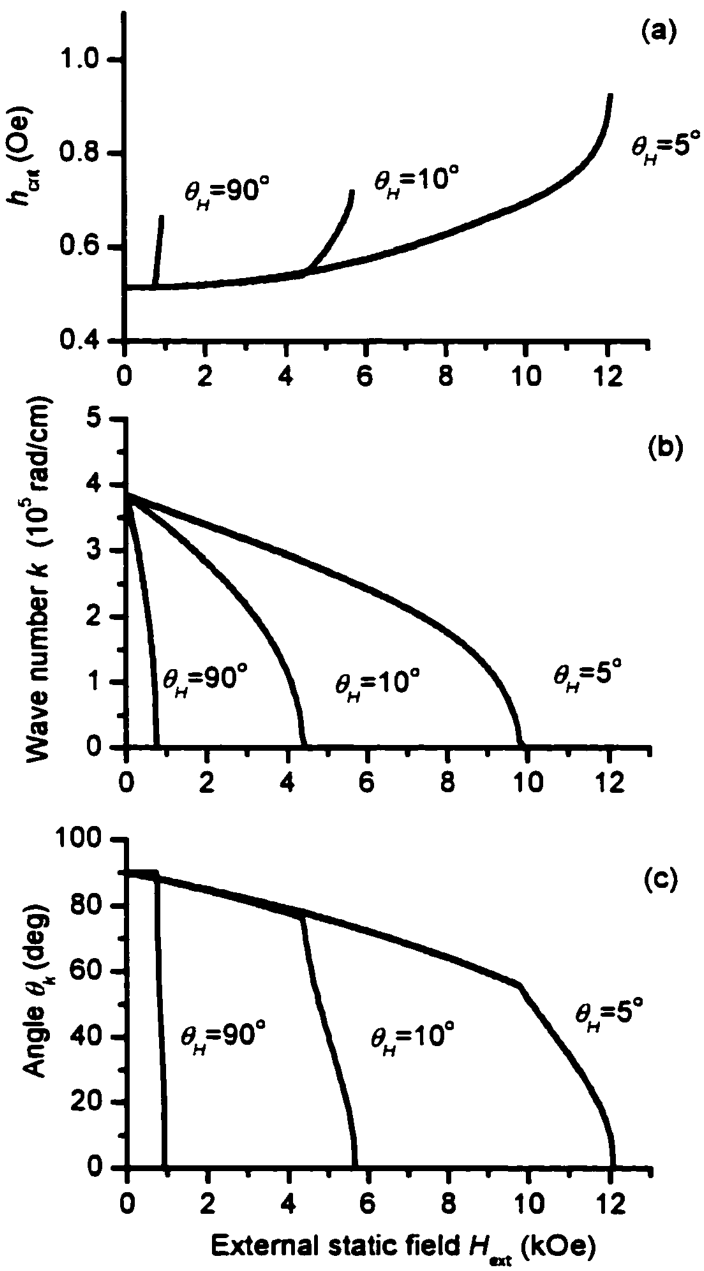


Figure 2.5. Threshold and critical mode parameters as a function of the external field $H_{ext}$ for the easy plane disk with 17 GHz microwave excitation. The graphs show (a) first order spin wave instability threshold field $h_{crit}$ vs. $H_{ext}$, (b) critical mode spin wave wave number $k$ vs. $H_{ext}$, and (c) polar spin wave propagation angle $\theta_k$ vs. $H_{ext}$. The graphs show results for values of $\theta_H$, the field angle relative to the disk normal, as indicated.

One aspect of Figs. 2.5(a) and 2.5(c) requires additional comment. In graph (a), the $h_{crit}$ curve for $\theta_H = 90°$ sticks at a constant value as long as the critical mode $k$ value is non zero. This corresponds to the flat part of the curve in (a) for $\theta_H = 90°$ and $H_{ext}$ below about 0.7 kOe. The other $h_{crit}$ vs. $H_{ext}$ curves for $\theta_H = 10°$ and $\theta_H = 5°$ in graph (a) start out at the same $h_{crit}$ value as for $H_{ext} = 0$, but then increase slightly as $H_{ext}$ is increased. The fact that the initial part of the $\theta_H = 90°$ curve in (a) is flat, while the other curves have a nonzero low field slope is not obvious from the curves.

The critical mode $\theta_k$ vs. $H_{ext}$ response in Fig. 2.5(c) shows a similar effect. The curve for the critical mode $\theta_k$ vs. $H_{ext}$ for $\theta_H = 90°$ sticks at precisely 90° as long as the critical mode $k$ is non zero. The curves for $\theta_H = 10°$ and $\theta_H = 5°$ start out at $\theta_k = 90°$ for $H_{ext} = 0$ but decrease slightly as $H_{ext}$ is increased from zero. These subtle effects are related to the change in the pumping configuration when $\mathbf{M}_s$ is pulled out of the disk plane. For $\theta_H = 90°$, one has a simple parallel pumping geometry. For $\theta_H \neq 90°$, one has a more complicated pumping geometry with both parallel and perpendicular pumping components. These distinctions will be considered in more detail below.

These results demonstrate the power of the general theory. Consider first the left most curves in the Fig. 2.5 graphs for $\theta_H = 90°$. As noted above, these results correspond to parallel pumping. This case, parallel pumping for an in-plane magnetized easy plane sample, corresponds to the specific problem considered by Schlömann *et al.* [1963]. For fields below about 700 Oe, $h_{crit}$ is constant, the critical mode $k$ decreases, and the critical mode $\theta_k$ sticks at 90°. Above 700 Oe, there is a jump in $h_{crit}$ and a rapid drop in the critical mode $\theta_k$ to zero over a very narrow field interval. These responses are all related to the shape of the spin wave band for this geometry and the critical mode behavior as it relates to this shape.

A perspective sketch of spin wave dispersion band for this parallel pump situation is shown in Fig. 2.6. The diagram is for purposes of illustration only and not to scale for the Zn-Y example considered here. The dispersion is shown for some fixed value of $H_{ext}$. The $\varphi_k$ axis is shown for 0 - 90° only in order to keep the diagram uncluttered. The inset shows $\omega_k$ vs. $\varphi_k$ for the range 0 - 180° for the top of the band at $\theta_k$ = 90° and $k$ = 0. An increase in $H_{ext}$ would shift the entire band up in frequency. Two constant $\theta_k$ surfaces are indicated. The $\theta_k$ = 0 surface which defines the bottom of the band is $\varphi_k$ independent and curves upward with increasing $k$ due to exchange. The $\theta_k$ = 90° surface which defines the top of the band changes with $\varphi_k$. This $\varphi_k$ dependence causes the warped surface evident in the figure.

Keep in mind that the first order threshold calculation for a given $H_{ext}$ will involve a scan over available spin wave states at $\omega_k = \omega / 2$. The available modes will correspond to a particular horizontal cut across the band in Fig. 2.6. As the field is increased, the spin wave band will move up, relative to this cut. The minimum threshold critical mode will correspond to a particular point on this cut, and the critical mode parameters will also change as the field is changed.

At very low field, the $\omega / 2$ cut will be above point $\omega_A$ in Fig. 2.6. As shown by Fig. 2.5 (b) and (c), the minimum threshold critical mode at $\theta_H$ = 90° for low fields has a nonzero $k$ and $\theta_k$ = 90°. As noted, this critical mode also has a $\varphi_k$ of 0 or 180°. The corresponding critical mode point is labeled "C" in Fig. 2.6. As the field is increased, the $\omega / 2$ cut remains fixed and the entire band shifts up. This causes the critical mode point

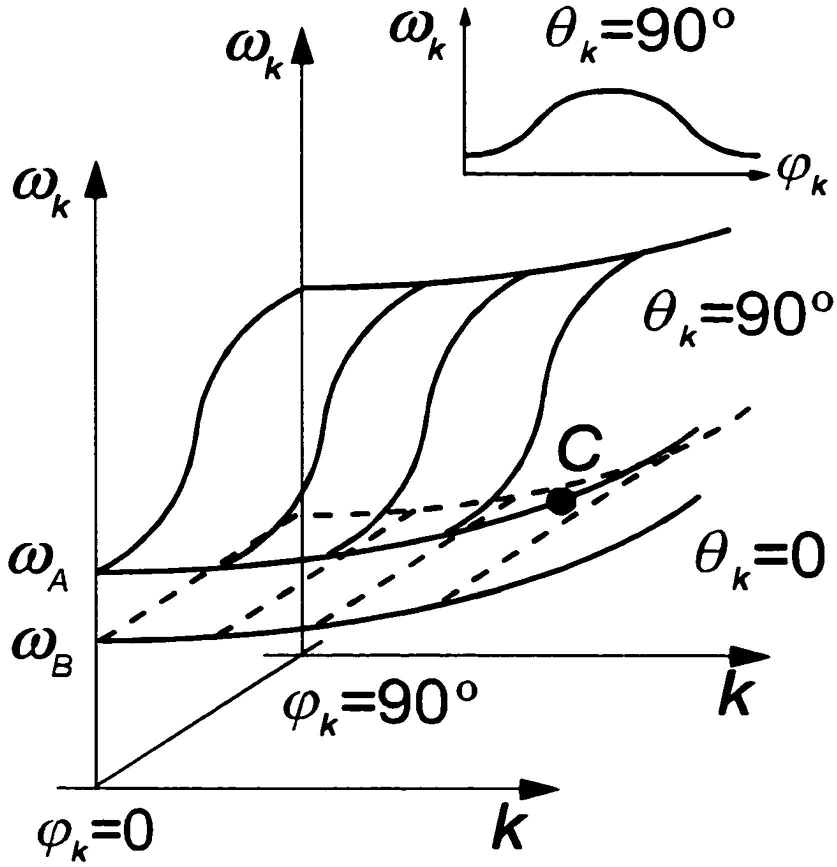


Figure 2.6. Schematic bulk spin wave dispersion diagram for an easy plane disk with the static field in plane at $\theta_H = 90°$. The graph shows the spin wave frequency $\omega_k$ vs. wave number $k$ and azimuthal spin wave propagation angle $\varphi_k$ for $\theta_k = 0$ and $\theta_k = 90°$, where $\theta_k$ is the polar spin wave propagation angle. The inset shows $\omega_k$ vs. $\varphi_k$ for $\theta_k = 90°$.

to move down in $k$. At some point in field, point $\omega_A$ moves up to meet the $\omega/2$ cut and the critical mode $k$-value goes to zero. This part of the critical mode behavior corresponds to the constant part of the curve at the start of the $h_{crit}$ vs. $H_{ext}$ curve in Fig. 2.5(a) for $\theta_H = 90°$. The corresponding change in $k$ is evident in Fig. 2.5(b). Note that $\theta_k$ is constant over this same field interval, as noted above and shown in Fig. 2.5(c). Note also that $\varphi_k$ remains at zero or 180° over this entire range.

As the field is increased further, the band continues to shift up relative to the $\omega/2$ cut. Correspondingly, the critical mode point moves from $\omega_A$ down to $\omega_B$ at the very bottom of the band, $\theta_k$ changes gradually from 90° to zero, and $\varphi_k$ remains at zero or 180° as before. This response corresponds to the steeply rising part of the $h_{crit}$ vs. $H_{ext}$ curve in Fig. 2.5(a) for $\theta_H = 90°$, as well as the rapid drop in $\theta_k$ in graph (a). Note that at the $\omega/2 = \omega_B$ end point, the $h_{crit}$ threshold is finite. For isotropic materials, the threshold at this band edge diverges because the limiting mode is circularly polarized. For Zn-Y, this end point mode is elliptically polarized and one obtains a non-infinite threshold. This observation was first made by Schlömann *et al.* [1963]. One may also note that the ellipticity causes a drastic factor-of-four reduction in the overall threshold for Zn-Y, relative to isotropic ferrite materials.

There is a fundamental reason for the critical mode response described above. In the case of parallel pumping, the minimum threshold mode is always the mode with the largest spin precession ellipticity. One may use simple dipole energy arguments to show that for an $\omega/2$ cut above $\omega_A$, the mode with the highest ellipticity sits at $\theta_k = 90°$ and $\varphi_k = 0$ or 180°. When the cut falls below $\omega_A$, the maximum ellipticity condition keeps $\varphi_k$ at zero or 180°, and $\theta_k$ is forced to decrease as $\omega_A$ and $\omega_B$ move up.

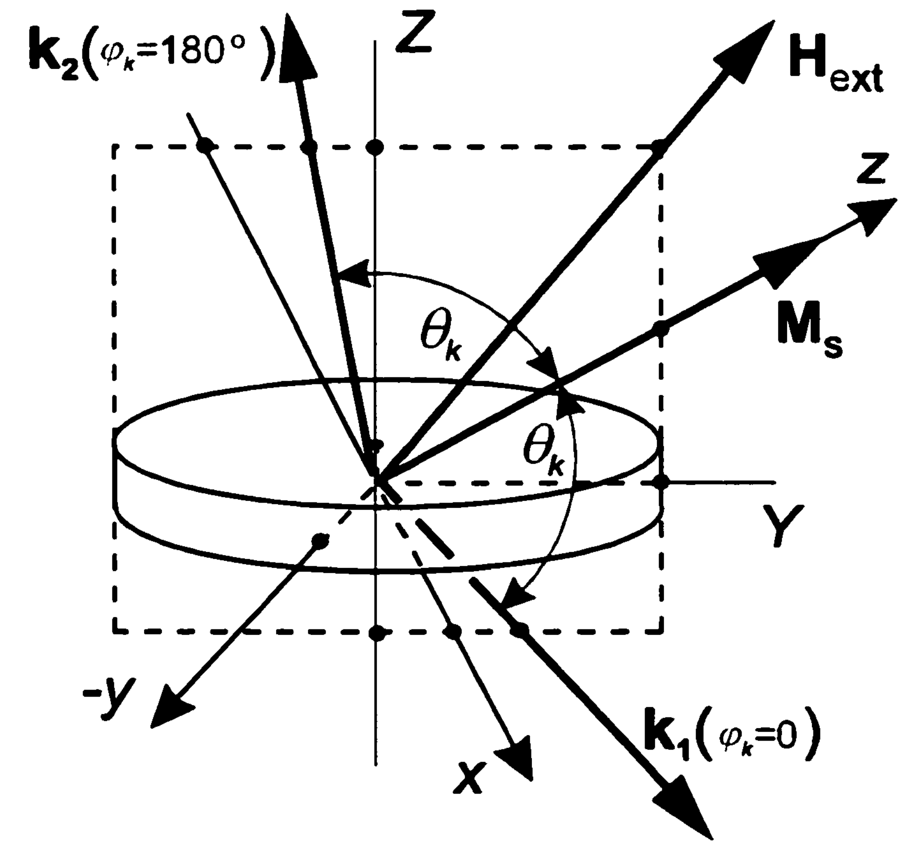


Figure 2.7. Spin wave propagation geometry for an out of plane external static field $H_{ext}$ and corresponding out of plane static magnetization $M_s$. The diagram shows the laboratory frame $Y$ and $Z$ axes and the precession frame ($x$, $-y$, $z$) axes. The wave vectors $\mathbf{k}_1$ and $\mathbf{k}_2$ are for a common polar spin wave propagation angle $\theta_k$ and values of the azimuthal spin wave propagation angle $\varphi_k$ of zero and 180°, as indicated.

Turn now to the two sets of curves in Fig. 2.5 for $\theta_H \neq 90°$. These curves are completely different from the situation for $\theta_H = 90°$ in-plane field case. The reason is that as $\theta_H$ drops below 90° so that the applied field is out of plane, any nonzero value of $H_{ext}$ will pull the static magnetization out of the disk plane. This has dire consequences for (1) the pumping configuration and (2) the response of the spin wave band to changes in the applied field.

These important effects can be understood from the modified version of Fig. 2.4 given in Fig. 2.7. There are two main changes in this figure. First, the indicated axes with arrowheads are the $(x, y, z)$ precession frame axes. The $x$-axis is in the plane of the page and the $y$-axis is into the page. Second, a pair of wave vectors are shown for $\varphi_k = 0$ or 180° and a common value of $\theta_k$, taken to be below 90°. The $\theta_k \neq 90°$ situation is chosen deliberately to demonstrate how the out-of-plane $\mathbf{H}_{ext}$ and $\mathbf{M}_s$ breaks the symmetry found for the $\theta_H = \theta_M = 90°$ situation discussed above.

When $\mathbf{H}_{ext}$ is out of plane, $\mathbf{M}_s$ will be gradually pulled out of the disk plane as $H_{ext}$ is increased. Moreover, the modifications to the spin wave band in Fig. 2.6 are such that the $\omega_A$ point is pushed down in frequency for a given value of $H_{ext}$. The net result is a significant increase in the size of $H_{ext}$ which is needed to raise $\omega_A$ up to the $\omega_k = \omega/2$ cut which defines the available modes for instability. The applicable equations for the present example are

$$H_{eff}^{S} = H_{ext}\cos(\theta_H - \theta_M) - 4\pi M_s \cos^2\theta_M + H_A \cos^2\theta_M, \tag{2.78}$$

the equilibrium condition of Eq. (2.77), and the spin wave dispersion,

$$\omega_k^2 = |\gamma|^2 [H_{eff}^{S} + Dk^2 + H_A \cos^2\theta_M] \times [H_{eff}^{S} + Dk^2 + H_A \cos 2\theta_M]$$

$$+|\gamma|\omega_M \sin^2\theta_k[H_{\text{eff}}^{\text{S}} + Dk^2 + H_A(\cos^2\theta_M - \sin^2\theta_M \sin^2\varphi_k)]\,. \tag{2.79}$$

In the $\theta_H = \theta_M = 90°$ limit, Eq. (2.79) reduces to $H_{\text{eff}}^{\text{S}} = H_{\text{ext}}$ and the spin wave band reduces to the form shown in Fig. 2.6. The values of $H_{\text{ext}}$ for which $\omega_A$ crosses $\omega/2$ for the two right most curves in Fig. 2.5(a) correspond to the kink points at about 4.4 and 9.8 kOe for $\theta_H = 10°$ and $\theta_H = 5°$, respectively.

The small increase in $h_{\text{crit}}$ with $H_{\text{ext}}$ for fields below the kink points in Fig. 2.5(a) for $\theta_H = 10°$ and $\theta_H = 5°$, and the corresponding weak drops in the critical mode $\theta_k$ in Fig. 2.5(c) curve are due to the change from pure parallel pumping to oblique pumping. Oblique pumping means that the microwave field has components both parallel and perpendicular to $\mathbf{M}_s$. This effect can be seen from Fig. 2.7. Keep in mind that the linearly polarized microwave field (not shown) is in the film plane and along $Y$, while $\mathbf{M}_s$ is tipped out of the film plane. As $H_{\text{ext}}$ is increased, $\mathbf{M}_s$ is pulled more and more out of plane and the $\mathbf{h}$ component transverse to $\mathbf{M}_s$ increases. The increase in this transverse pumping component causes the critical mode $\theta_k$ to decrease. Note that for pure parallel pumping with $\mathbf{h}$ parallel to $\mathbf{M}_s$, the critical mode $\theta_k$ value sticks at exactly 90° even if $\mathbf{M}_s$ is pulled away from $Y$. In the present geometry, the microwave field direction is fixed, the out-of-plane $\mathbf{H}_{\text{ext}}$ pulls $\mathbf{M}_s$ out of plane and forces the system into an oblique pumping configuration.

The change to an oblique pumping configuration has an additional effect which breaks the symmetry and shifts the critical mode response from the two equivalent $\varphi_k$ propagation angles of zero and 180° to $\varphi_k = 180°$ only. Figure 2.7 shows that the out of plane $\mathbf{M}_s$ also yields a precession frame $x$-axis which is rotated away from the disk normal and hard $c$ axis in this example. The figure also shows two potential $\mathbf{k}$ vectors at

$\varphi_k = 0$ and $\varphi_k = 180°$. In the case of an out of plane $\mathbf{M}_s$, it is clear that these two vectors are not equivalent. Based on the ellipticity arguments given above, one can show that the mode with the highest ellipticity, and hence the lowest threshold, will be for the **k** which is closest to the *c* axis, or the $\varphi_k = 180°$ direction in the figure. The symmetry breaking effect explains, therefore, the analytical result of two equivalent critical mode propagation directions of $\varphi_k = 0$ or $180°$ for $\theta_H = 90°$ and a single direction at $\varphi_k = 180°$ for $\theta_H < 90°$. Note that the symmetry in the critical mode $\varphi_k$ can be broken even for oblique pumping in isotropic ferrites (Yakovlev [1969] and Patton [1969]).

The above example demonstrates the application of the formal theory to real problems and gives specific results for first order processes in an easy plane ferrite disk. The power of the general theory is especially evident for the oblique pumping geometry which is obtained when the static applied field is out of plane. The spin wave instability theory discussed in this chapter will be used for the data analysis in Chapters 4, 5, and 6. The results of the above example calculations will be an important part of the oblique pumping data analysis for Zn-Y in Chapter 6. The next chapter is concerned with the investigated ferrite materials, threshold field measurement technique, and example results.

# CHAPTER 3

# MATERIALS AND EXPERIMENTAL TECHNIQUES

This chapter introduces the materials and the experimental techniques which were used for the spin wave instability threshold measurements. Section 3.1 describes the materials and static magnetic properties. The three materials include LPE YIG thin films, polycrystalline hipped YIG, and easy plane hexagonal ferrite Zn-Y. Brief remarks are also provided on sample preparation and physical properties.

Section 3.2 discusses the operation and calibration of the high power microwave spectrometer. Section 3.3 describes the specific methods for threshold field determination. One is based on the visual inspection of the reflected pulse shape. The second method determines a threshold field from the quantitative data on reflection coefficient vs. microwave field amplitude.

Section 3.4 gives example results on a threshold field $h_{crit}$ for a standard commercial polycrystalline YIG sphere and establishes procedures for the $h_{crit}$ data analysis. These example results serve to introduce the technique of the spin wave instability threshold field measurements and parameters that will be important for the next three chapters. Based on these threshold data, presented in the form of butterfly curves, critical modes and a specific $\Delta H_k$ dependence as a function of wave vectors can be determined.

### 3.1. Materials and Static Properties

Three different types of materials were investigated. These three types are single crystal low linewidth LPE YIG, polycrystalline hipped YIG, and high anisotropy single crystal Zn-Y. The Zn-Y materials were of two kinds, pure and Mn-substituted. The main focus of the work was on the Mn-substituted Zn-Y, denoted as Zn(Mn)-Y. Along with Zn(Mn)-Y, some of the pure Zn-Y samples were measured. The chemical composition and static magnetic properties of these materials are summarized in Table 3.1. For single crystal LPE YIG, the values of $4\pi M_s$ and $H_A$ were taken from the literature (Winkler [1981]). For hipped YIG and Zn-Y, the values of $4\pi M_s$ and $H_A$ were obtained experimentally and will be discussed shortly.

Single crystal YIG has a small cubic magnetocrystalline anisotropy. The cubic anisotropy may be characterized in terms of an energy density function of the form

$$F_A = K_1(\alpha_1^2\alpha_2^2 + \alpha_2^2\alpha_3^2 + \alpha_3^2\alpha_1^2)^2 + \dots \tag{3.1}$$

where $K_1$ is the first-order anisotropy constant and $\alpha_1$, $\alpha_2$, and $\alpha_3$ are the direction cosines of **M** with respect to the directions [100], [010], and [001] in the cubic lattice (Gurevich and Melkov [1996]). This free energy allows one to write specific expressions for elements of the anisotropy tensor **A** in Chapter 2. The relevant components of the anisotropy tensor will be given in Chapter 4 in connection with the data for single crystal LPE YIG films. Following the literature, the anisotropy field parameter $H_A$ in YIG is defined by $H_A = K_1/M_s$, where only the first anisotropy energy constant $K_1$ which is negative is taken into account. The anisotropy field $H_A$ in Zn-Y was introduced in

Table 3.1. Summary of chemical composition, saturation induction $4\pi M_s$, anisotropy field parameter $H_A$ for LPE YIG, hipped YIG, Zn(Mn)-Y, and pure Zn-Y.

| Material | Chemical composition | Saturation induction $4\pi M_s$ (G) | Anisotropy field $H_A$ (Oe) |
|---|---|---|---|
| Single crystal LPE YIG | $Y_{2.995}Ca_{0.005}Fe_5O_{12}$ | 1750 | -44 |
| Polycrystalline hipped YIG | $Y_3Fe_5O_{12}$ | 1825 | - |
| Single crystal Mn-substituted Zn(Mn)-Y | $Ba_2Mn_{0.68}Zn_{1.82}Fe_{11.83}O_{21.2}$ | 2330 | -9300 |
| Single crystal pure Zn-Y | $Ba_2Zn_2Fe_{12}O_{22}$ | 2550 | -7900 |

Section 2.4 and is defined by $H_A = 2K_u/M_s$. Here $K_u$ is the uniaxial anisotropy energy constant which is also negative.

The first material type is single crystal YIG films made by liquid phase epitaxy (LPE). The single crystal YIG films are useful for microwave applications because of the small size and very low microwave loss. These samples were produced through a collaborative effort with Charles University of Prague and were provided by Dr. M. Marysko of Institute of Physics, Prague, Czech Republic. These materials are unique because they were produced with a lead free flux based on a BaO oxide. In conventional liquid phase epitaxy of garnets, thin films of highest perfection are grown from a PbO-$B_2O_3$ flux on nonmagnetic garnet substrates such as gadolinium gallium garnet (GGG) (Winkler [1981]). The best quality films were obtained on (110) oriented GGG substrates, as opposed to conventional Pb-based films where the (111) orientation gives the best results. The NMR measurements on these films verified very small content of impurities and a very narrow NMR linewidth which means large relaxation times (Marysko *et al.* [2001]).

Small additions of $Ca^{2+}$ ions were introduced into the melt in order to compensate the charge of the tetravalent silicon impurity ions $Si^{4+}$ and reduce the number of divalent iron ions $Fe^{2+}$. The chemical composition of the films was $Y_{3-x}Ca_xFe_5O_{12}$ where x denotes the Ca concentration per formula unit (f.u.). Chapter 4 presents $h_{crit}$ results only on films with specific x = 0.005. The nominal film thickness of the investigated samples was 11 μm. The films were subsequently cut and shaped into discs with diameters ranging from 1.5 to 4 mm. The samples were fabricated in the Czech Republic. The unique feature of these samples compared to standard (111) oriented films is that the

(110) oriented films have [100], [110], and [111] axes in the plane of the films which makes it possible to investigate the effect of magnetocrystalline anisotropy in high quality single crystal YIG thin films.

The second material type is dense hipped polycrystalline YIG. Hipped YIG is particularly useful for microwave applications because it has relatively low microwave loss and can be made in a larger size and at a lower cost than single crystal YIG. Hipped polycrystalline YIG spheres and discs were provided by Dr. Gil Argentina of Pacific Ceramics, Inc. The initial material used to make the samples was pure yttrium iron garnet polycrystalline powder. After conventional sintering, a large slug of the material was put through a hot isostatic pressing treatment. The nominal grain size was 8 $\mu$m. The disks and spheres were made from the inside part of the slug in order to avoid an oxygen deficient exterior. The hipped YIG ferrite samples were shaped as spheres and disks and polished afterwards. The spheres were approximately 2 mm in diameter and the discs were 3 mm in diameter and 0.5 mm in thickness. A density of 5.172 g/cm$^3$ was assumed, which corresponds to the theoretical value of 100% dense YIG material. This assumption is supported by the FMR linewidth measurements that proved that porosity was eliminated. Some of the spheres were roughly polished. However, subsequent measurements showed no significant differences of the magnetic properties between polished and unpolished spheres.

It turned out to be that the measurements of the geometrical size made with a micrometer were inconsistent. Therefore, the geometrical properties were calculated from the measured mass and the specified density. The mass and the density yield the volume of the sample. The volume yields a diameter for a sphere and the thickness for a disk. All samples showed similar microwave properties and the data for only one sphere and one disk are presented. The physical properties of the samples are given in Table 3.2. Vibrating sample magnetometer (VSM) has been used to measure static magnetization of the sphere and the disk. The average saturation induction obtained was $4\pi M_s$ = 1825 G. The accuracy was about 2% which was about 20 G. The saturation magnetization was obtained from the measured magnetic moment in emu and the volume from Table 3.2.

Polycrystalline YIG can be considered as a ferrite material with zero anisotropy. The anisotropy field parameter $H_A$ of single crystal YIG is about 44 Oe which is much smaller than $4\pi M_s$. It means that magnetocrystalline anisotropy can be completely neglected in polycrystalline YIG with randomly oriented grains. Therefore, polycrystalline hipped YIG can be assumed to be completely isotropic for the analysis of experimental data.

The third type is single crystal hexagonal ferrite Zn-Y with large easy plane anisotropy when the easy direction is in the basal hexagonal $c$ plane. The "Y" letter indicates a ferrite type. The hexagonal ferrites with large anisotropy are promising materials for microwave and millimeter wave applications (Vittoria [1980]). The unit formula for Zn-Y is $Ba_2Zn_2Fe_{12}O_{22}$. The Zn-Y ferrite has a Curie temperature of 405 K and the unit cell with dimensions 6 and 43.5 angstrom which is stretched along the hexagonal $c$ axis (Sugimoto [1982]).

The main focus of the work was on the Mn-substituted Zn(Mn)-Y. Some of the pure Zn-Y samples were also measured. The formula unit for the substituted material used in this study was $Ba_2Mn_{0.68}Zn_{1.82}Fe_{11.83}O_{21.2}$. These easy-plane hexagonal ferrites were

Table 3.2. Summary of the hipped YIG sample properties.

| Sample shape | Mass (mg) | Thickness (mm) | Diameter (mm) | Volume ($mm^3$) |
|---|---|---|---|---|
| Sphere | 23.30 | - | 2.049 | 4.51 |
| Disc | 15.34 | 0.420 | 3.00 | 3.25 |

grown by Dr. Michael A. Wittenauer at Purdue University under United States Office of Naval Research (ONR) Grant No. N00014-91-J-1323. The Mn-substitution compensates the excess of $Fe^{2+}$ ions and reduces microwave conductivity. Microwave conductivity adds associated significant eddy-current contribution to the loss (Truedson [1993]).

The samples came as single crystal chunks. The measurements of microwave magnetic properties require high quality defect-free samples. It is hard to fabricate defect-free single crystal samples because the material is brittle. Various mechanical operations were performed to produce circular and rectangular plates of different sizes and thicknesses and polish them. All samples had a crystallographic *c*-plane in the plane of the plate.

Table 3.3 shows physical properties of the nine samples that were fabricated for microwave measurements. The focus is on the S1 through S6 Zn(Mn)-Y samples and the SP1 – SP3 Zn-Y samples are also listed. The geometrical sizes were measured by a spatially calibrated Meiji EMZ optical microscope with 5 μm resolution. The table also shows the estimated volume for S2 and SP1 samples inferred from the sample mass and a theoretical density of 5.48 g/cm$^3$ (Truedson [1993]). These volume values were used for the VSM measurements.

The static magnetic properties were deduced from the VSM measurements. Magnetization vs. applied field was measured on the Zn(Mn)-Y disk sample S2 and the large Zn-Y disk sample SP1 listed in Table 3.3. Data were obtained for applied fields up to 15 kOe, for field directions which were both in-plane and perpendicular to the plane of the plate. Shape demagnetizing effects were taken into account empirically, based on the saturation induction determinations and the saturation fields for the in-plane and

Table 3.3. Summary of Zn(Mn)-Y and Zn-Y sample properties.

| Sample | Material | Sample shape | Thickness (mm) | In-plane size (mm) | Mass (mg) | Volume ($cm^3$) |
|---|---|---|---|---|---|---|
| S1 | Zn(Mn)-Y | disk | 0.34 | 2.39 | - | - |
| S2 | Zn(Mn)-Y | disk | 0.19 | 2.32 | 4.1 | 0.0075 |
| S3 | Zn(Mn)-Y | disk | 0.14 | 1.52 | - | - |
| S4 | Zn(Mn)-Y | disk | 0.09 | 2.32 | - | - |
| S5 | Zn(Mn)-Y | slab | 0.09 | 1.62×0.72 | - | - |
| S6 | Zn(Mn)-Y | slab | 0.05 | 1.44×0.64 | - | - |
| SP1 | Zn-Y | disk | 0.43 | 2.53 | 11.5 | 0.0021 |
| SP2 | Zn-Y | disk | 0.20 | 2.50 | - | - |
| SP3 | Zn-Y | disk | 0.13 | 1.81 | - | - |

perpendicular-to-plane field cases. The saturation induction $4\pi M_s$ was determined to be 2.33 ± 0.04 kG for Zn(Mn)-Y and 2.55 ± 0.04 kG for pure Zn-Y, based the magnetic moment values at 15 kOe and volume estimates inferred from the sample mass in Table 3.3. Based on this value for $4\pi M_s$ and the measured saturation fields in the parallel and perpendicular configurations, the negative anisotropy field $H_A$ was determined to be -9.3 ± 0.1 kOe for Zn(Mn)-Y and -7.9 ± 0.1 kOe for pure Zn-Y. The Mn-substitution not only reduces conductivity but also significantly changes material parameters. The $H_A$ values for these materials can also be deduced from the FMR field measurements which will be discussed in Section 6.1.

DC resistivity measurements were performed as a check of the effectiveness of Mn-substitution and suppression of $Fe^{2+}$ ions. The sample was positioned between two metal plates which served as contacts and the current was measured at constant voltage of 18 V. For pure Zn-Y the resistivity $\rho_{\parallel}$ in the direction parallel to hexagonal $c$ axis was $7.0\times10^5$ $\Omega$·cm. The resistivity $\rho_{\perp}$ in the direction perpendicular to hexagonal $c$ axis was $4.9\times10^4$ $\Omega$·cm. The anisotropy of resistivity was also shown by Kasami and Koide [1966]. In this case, the resistivity is much larger because of the high purity of Zn-Y material. DC resistivity measurements of Zn(Mn)-Y showed that $\rho_{\parallel}$ is greater than $4\times10^7$ $\Omega$·cm which is typical for a good insulator. This means that eddy-current losses in Zn(Mn)-Y are negligible because microwave resistivity scales with dc resistivity (Truedson *et al.* [1994]).

### 3.2. High Power Microwave Spectrometer

The high power reflection cavity microwave spectrometer used in this work was similar to the systems described by Cox *et al.* [2001] and Zhang *et al.* [1987]. Measurements were made with two different waveguide-cavity systems. Waveguide-cavity systems with resonance frequencies of 9 and 16.7 GHz were set up at X-band and Ku-band, correspondingly. The X-band cavity was designed for 9 GHz. The Ku-band cavity was designed for 16.7 GHz. A block diagram of the basic system is shown in Fig. 3.1. The spectrometer consists of a pulsed microwave source, an input microwave line, a reference arm, a reflection arm, an electromagnet, and a cavity with a sample. The cavity is positioned between magnet poles of an electromagnet. Cavity and sample considerations will be given shortly.

The pulsed microwave source consists of a Hewlett Packard (HP) 83640A synthesized sweeper, a Wavetek Model 81 pulse generator, and an Applied Systems Engineering Model 174XKu travelling wave tube (TWT) amplifier. The synthesized sweeper provides a –4 dBm cw signal to the TWT amplifier. The pulse generator sends a 4 V gate signal to the TWT amplifier which triggers the generation of a microwave pulse of approximately 2 kW in peak power with a maximum duty cycle limit of 4%. The standard pulse width was 50 μs, the pulse repetition frequency was 40 Hz, and the pulse rise time was about 100 ns.

The input microwave line consists of a high power isolator, a microwave switch, a precision attenuator, and a reflection cavity. For X-band 9 GHz measurements, a Raytheon 1XH7 isolator is used. For Ku-band 16.7 GHz measurements, a Raytheon

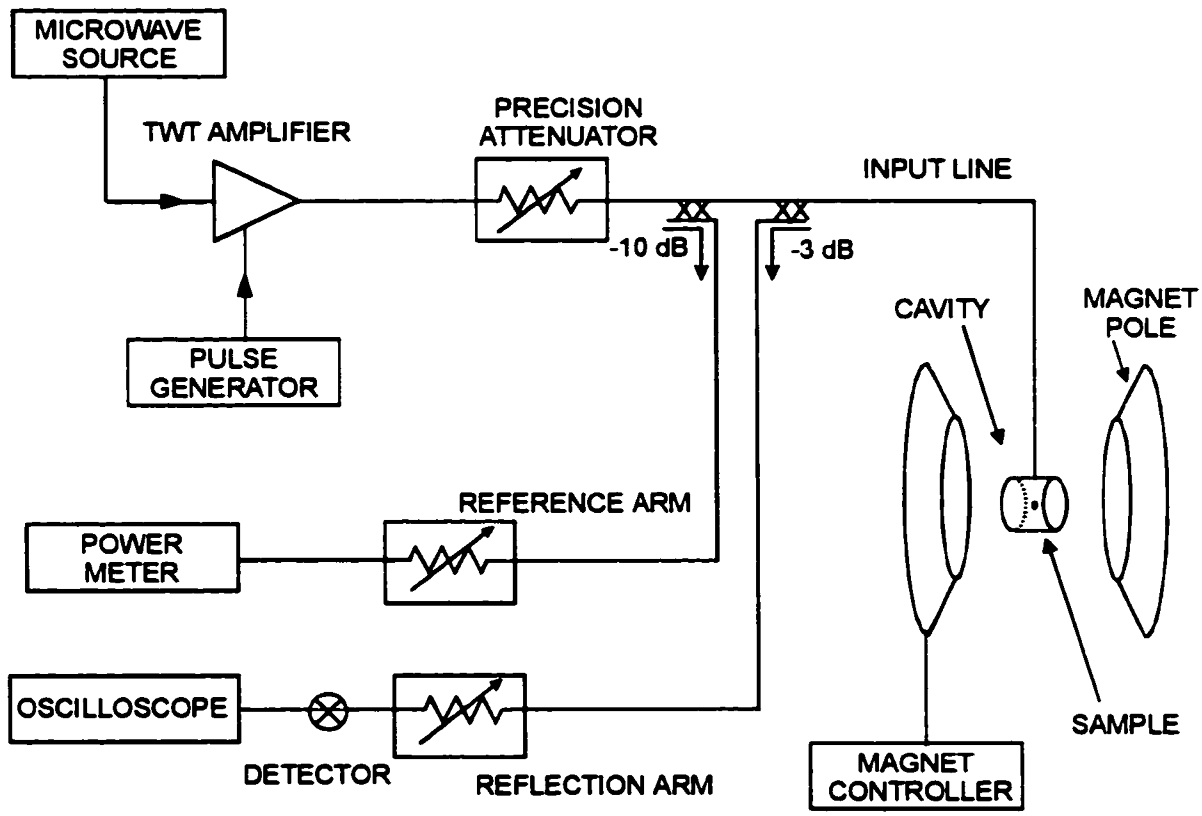


Figure 3.1. Schematic diagram of the high power reflection cavity microwave spectrometer used for spin wave instability threshold measurements.

1KuM2 isolator is used. The microwave switch is used for low power calibration measurements. The precision attenuator controls the input microwave power. For X-band 9 GHz measurements, an HP X382A precision attenuator is used. For Ku-band 16.7 GHz measurements, an HP P382A precision attenuator is used.

The reference and reflection arms monitor the power incident on and reflected from the cavity, respectively. The reference arm is coupled to the input microwave line through a 10 dB directional coupler and is terminated with an HP 8481A power sensor. The microwave power incident on the power sensor is measured by an HP 436A power meter. The reference arm attenuator protects the sensitive power sensor. After the adjustment for the power difference between the cavity position and the power sensor position, the measured average power divided by the duty cycle gives the peak input power at the cavity, $P_{in}$. The reflection arm is coupled to the input microwave line through a 3 dB directional coupler and is terminated with an HP 8474D microwave detector. The voltage signal from the detector is observed with a Tektronix TDS410A digitizing oscilloscope, which is synchronized with the pulse generator. The reflection arm attenuator protects the sensitive power sensor.

The electromagnet is a 12 inch electromagnet with variable size pole pieces. The electromagnet can be rotated in horizontal plane so that the direction of the magnetic field can change with respect to a microwave magnetic field direction in a cavity. The electromagnet is powered by a Harvey-Wells HS-1050 precision magnet power supply. The maximum magnetic field strength is about 8.5 kOe for a 4 inch magnet gap and about 20 kOe for a 1.25 inch magnet gap, respsectively. The magnetic field is measured by an F. W. Bell Series 9900 gaussmeter. The magnetic field setting is computer

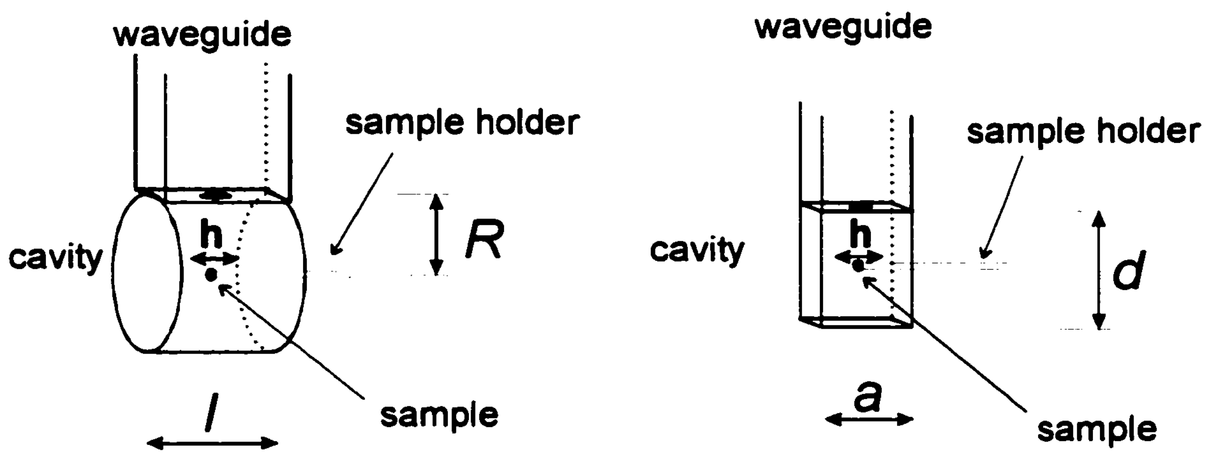


a) b)

Figure 3.2. Schematic diagram of the reflection cavities with a sample. a) $TE_{011}$ cylindrical cavity with the resonance frequency $f_{res}$ = 8.993 GHz. b) $TE_{102}$ rectangular cavity with the resonance frequency $f_{res}$ = 16.725 GHz.

controlled via a combined General Purpose Interface Bus (GPIB) and Data Acquisition Card (DAC) interface. All other measurement devices are also computer controlled via GPIB interface.

Figure 3.2 shows a schematic diagram of the two reflection cavities. Figure 3.2(a) shows a $TE_{011}$ cylindrical cavity with the resonance frequency $f_{res}$ = 8.993 GHz. For this excitation frequency, a high Q cylindrical cavity was used because the filling factor was small and high sensitivity was needed. Figure 3.2(b) shows a $TE_{102}$ rectangular cavity with the resonance frequency $f_{res}$ = 16.725 GHz. For this excitation frequency, the filling factor was higher than at lower frequencies and high sensitivity was not necessary. Both cavities were under coupled, which means that the increase in the cavity loss would increase the reflection from the cavity.

In both cases the sample position was in the center of the cavity and the microwave magnetic field was linearly polarized and along the sample holder length. Sample holders were made of rexolite rods and were of two types. One type holds the disk sample so that the disk normal is parallel to the sample holder length. The second type holds the disk sample so that the disk normal is perpendicular to the sample holder length. These sample holders along with the capability of magnet rotation provide the capability for a separate control of the orientation of the sample and microwave magnetic field and applied static field directions. This capability is important for oblique pumping measurements described in Chapter 6.

The next experimental consideration is the calibration procedure to obtain the microwave magnetic field amplitude at the sample position as a function of the power incident on the cavity, $P_{in}$. From standard microwave theory (Green and Kohane [1964]), the relation between $P_{in}$ and the peak microwave field amplitude at any point inside the cavity may be written as (Patton and Green [1971])

$$h = \sqrt{\frac{40Q_L(1-\rho_0)}{g_m f_{res} V_c} P_{in}}\ , \tag{3.2}$$

where $Q_L$ is the loaded Q of the cavity, $\rho_0$ is the dimensionless voltage reflection coefficient of the cavity at resonance, $g_m$ is a dimensionless geometrical factor, $f_{res}$ is the resonance frequency in GHz, $V_c$ is the cavity volume in mm$^3$, $P_{in}$ is the power incident on the cavity in W, and $h$ is the microwave field amplitude in Oe. The voltage reflection coefficient $\rho_0$ in Eq. (3.1) is related to the standard reflection coefficient $\Gamma$, measured in dB, according to $\rho_0 = 10^{\Gamma/20}$.

The $g_m$ parameter in Eq. (3.2) relates the stored energy in the cavity to the microwave field amplitude at a certain point, which is the center of the cavity in the present case. The $g_m$ parameter can be calculated from the standard waveguide theory (Waldron [1964] and Jackson [1998]) and is given by

$$g_m = \frac{\int_{V_c} |h|^2 \, dV}{V_c |h_0|^2}\ , \tag{3.3}$$

where $h_0$ is the field amplitude at the point where the sample is located. For the $TE_{011}$ cylindrical cavity used here, $g_m$ may be written as

$$g_m = \frac{1}{2} J_0^2(\rho_{11}) \left[ 1 + \left( \frac{\pi R}{l \rho_{11}} \right)^2 \right], \tag{3.4}$$

where $J_0$ is the zero order Bessel function, $\rho_{11}$ is the first zero root of the first order Bessel function, $R$ is the cavity radius, and $l$ is the cavity length shown in Fig. 3.2(a). For the $TE_{102}$ rectangular cavity used here, $g_m$ may be written as

$$g_m = \frac{1}{4}\left[1+\left(\frac{d}{2a}\right)^2\right], \tag{3.5}$$

where $a$ and $d$ are the width and the length of the cavity shown in Fig. 3.2(b), respectively.

Equation (3.2) shows that the calibration of the microwave field requires two parameters, $Q_L$ and $\rho_0$. For $Q_L$ and $\rho_0$ measurements, the following modifications can be made to the system shown in Fig. 3.1. In this case, the synthesized sweeper is connected directly to the input line via microwave switch and replaces the TWT amplifier so that the TWT amplifier is disconnected from the input microwave line. An HP 70820A microwave transition analyzer (MTA) replaces the crystal detector and the oscilloscope and measures the signal reflected from the cavity. The MTA system controls the sweeper, sweeps the frequency, and provides fixed cavity response as a function of the frequency. For the calibration scan, the cavity is replaced by a short which is positioned at the cavity iris position to give a reference input response. The reflection coefficient $\rho$ is the ratio of the cavity response to the reference response as a function of frequency. The minimum reflection coefficient corresponds to $\rho_0$ in Eq. (3.2). The $Q_L$ determination assumes a $\rho$ vs. $f$ cavity response which corresponds to a Lorenz resonance curve.

An example of the cavity response as a function of frequency for the empty $TE_{011}$ cylindrical cavity is shown in Fig. 3.3. The figure shows the reference and cavity reflection coefficients $\rho$ in dB. Based on the $\rho$ vs. $f$ response, one can determine the value of the $Q_L$ parameter (McKinstry and Patton [1989]). One also has to choose an appropriate frequency span for the $Q_L$ determinations.

For the high Q cylindrical cavity, the typical parameters were the following: a frequency span of about 80 kHz, a reflection coefficient Γ of about −19 dB, a $Q_L$ parameter of about 13,000, and a calibration ratio of about 16 $Oe^2/W$. If there is a sample in the cavity, the losses in the cavity may increase and calibration ratio may decrease up to 12 $Oe^2/W$ depending on the size of the sample. For the $TE_{102}$ rectangular cavity with resonance frequency 16.725 GHz, the frequency span was about 1000 kHz, the reflection coefficient Γ was about −16 dB, the $Q_L$ parameter was about 2,500, and the calibration ratio was about 8 $Oe^2/W$.

Equation (3.2) yields the microwave field amplitude for an empty cavity. When a sample is positioned in the cavity, a microwave field distribution changes. Equation (3.1) may still be used for the microwave field determination if the sample does not perturb the microwave field distribution significantly. In general, the microwave field should be calibrated for each sample orientation and every value of the static magnetic field $H$. In this work, the microwave field was calibrated for each sample orientation. Note that the $Q_L$ parameter may depend on $H$, especially when $H$ is near the FMR field position. In the present work, all measurements were made far from FMR and sample absorption did not significantly depend on $H$. When $Q_L$ value depends on $H$, an additional error is introduced and this error is taken into account. The overall measurement error of the microwave field amplitude measurements is estimated to be less than 10 %.

The above considerations describe the calibration procedure to find the microwave field amplitude at the sample position in the cavity. For this work, the main use of the high power microwave spectrometer was to measure the spin wave instability threshold

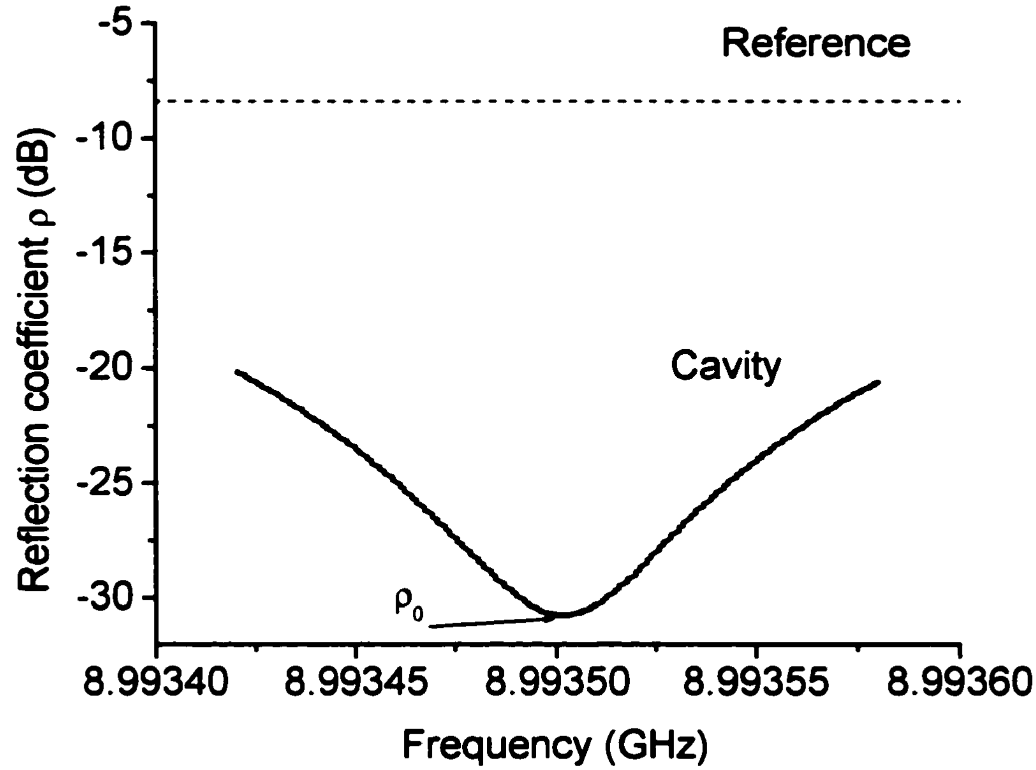


Figure 3.3. Reflection coefficient as a function of frequency for the $Q_L$ measurements for the empty $TE_{011}$ cylindrical cavity with the resonance frequency $f_{res}$ = 8.993 GHz. The solid line corresponds to the cavity response, the dashed horizontal line corresponds to the reference response. The minimum reflection coefficient is $\rho_0$.

field as a function of applied field $H$ for a given sample orientation. Therefore, one has to determine when the known microwave field amplitude exceeds the spin wave instability threshold. The next section will consider different methods of the threshold field determination.

### 3.3. Threshold Field Determination

The threshold field determination is based on the detection of the change in the microwave absorption of a sample. When the microwave field amplitude is below threshold, the sample microwave absorption is linear and the reflection coefficient is constant. Above threshold, the absorption drastically increases and one can observe the change in a signal reflected from the cavity. Measurements are carried out in a pulse regime and this change can be detected by two methods. The first one is a visual detection when one detects a threshold by observing a distortion in the reflected pulse. This visual method was used for $h_{crit}$ measurements described in Chapters 4, 5, and $h_{crit}$ measurements at 16.7 GHz described in Chapter 6. The second one involves point by point measurements of reflection coefficient vs. microwave magnetic field amplitude $h$ and consecutive threshold determination from these plots which can be done in two ways. This reflection coefficient method was used for $h_{crit}$ measurements at 9 GHz described in Chapter 6.

Consider the visual method. The threshold can be visually detected by the observation of the distortion in the shape of the reflected pulse envelope. Figure 3.4 illustrates the change in the pulse shape as the incident power increases for the pure Zn-Y

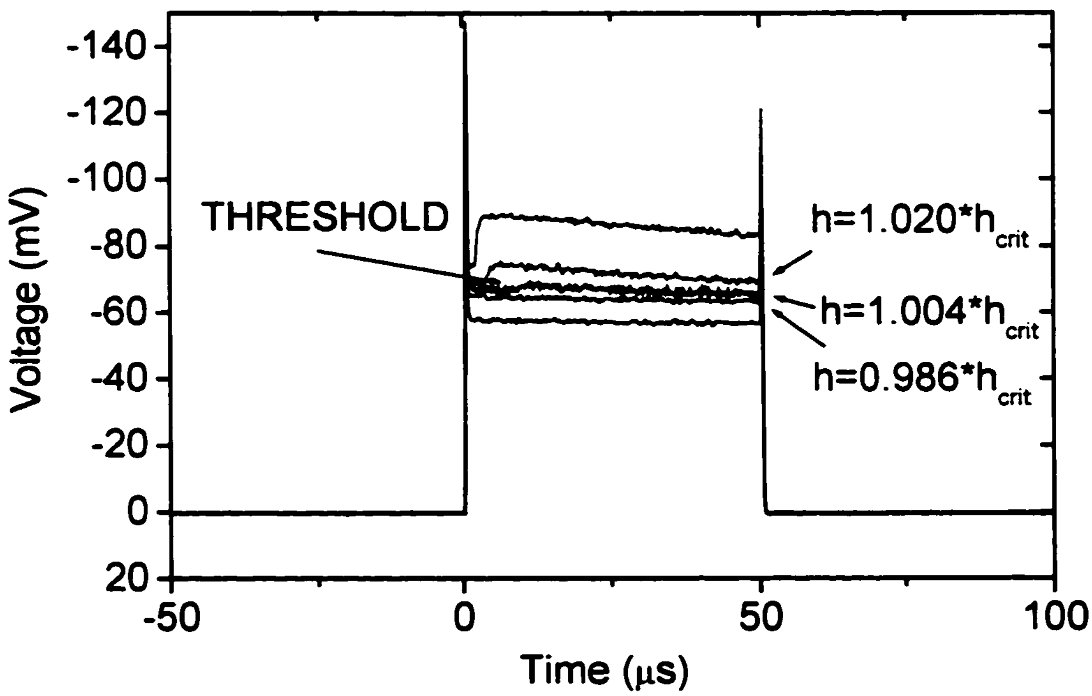


Figure 3.4. The envelope of the pulse reflected from the cavity with the Zn-Y disk. Parallel pumping at 16.723 GHz, applied field $H = 950$ Oe.

disk at 16.723 GHz pumping frequency. Note that the actual measured voltage signal from the crystal detector is negative and the pulse profile is negative too. The distinct spikes at the leading and trailing edge of the pulse are common for the reflection cavity response. These spikes originate from the frequency transition from dc to the carrier operational frequency at the leading and trailing edge of the input pulse generated by TWT. One can see that the threshold can be visually detected with accuracy better than 1 %. A threshold can be resolved even better in the case of yttrium iron garnet, where the characteristic step begins from the very end of the pulse (Schlömann *et al.* [1960]).

The visual method is convenient and fast. It requires the visual detection of the threshold and successive measurement of the input power $P_{in}$. An applied field is set up by hand, the power is increased by hand, and one looks at the distortion of the reflected pulse. Then one records the values of $H$ and $P_{inc}$ and from the calibration procedure of the previous section obtains $h_{crit}$ vs. $H$ curves that will be discussed in the next section. The visual method is useful when there is a clear distortion of the reflected pulse. When there is no clear distortion but gradual change in the reflection coefficient, one has to use the second method of the threshold field determination.

In the reflection coefficient method, the reflection coefficient is measured as a function of the microwave field amplitude. It requires the scan of the input power and, consequently, the microwave field amplitude. The manual scan is very time consuming and automation is necessary to perform routine measurements. Cox [2002] presents an elaborate discussion on the high power microwave spectrometer automation. The details of the automated system operation are given below.

The measurement system was operated by Labview program, which performs the following operations. First, it sets up a scan over applied dc field $H$ values of interest. Second, for each $H$ value, it adjusts the frequency of the input microwave signal so that it equals the resonant frequency of the cavity, which may change with $H$. Third, it scans the input power via a step motor which changes the setting of the main attenuator. The input power $P_{in}$ is recorded by the power meter. The power $P_{out}$, reflected from the cavity, is measured by the crystal detector. The crystal detector is calibrated so that the detector voltage corresponds to a certain power level. Then the reflection coefficient $\rho_0$ may be written as $\rho_0 = (P_{in}/P_{out})^{1/2}$. The microwave field amplitude $h$ is calculated from Eq. (3.1). The result is a pair of values ($h$, $\rho_0$) for the specific value of $P_{in}$. Fourth, these pairs form an array where $\rho_0$ is a function of $h$. This array is written in a data file. Fifth, the step motor resets the attenuator to the initial power level and $H$ is set to a new value.

As a result of the program, a user gets a number of data files equal to the number of $H$ values, where each file contains dependence $\rho_0$ vs. $h$. Analysis of such data file yields the threshold $h_{crit}$ value. Figure 3.5 shows an example of the $\rho_0$ vs. $h$ dependence for the pure Zn-Y disk at 8.993 GHz pumping frequency. The data are shown by connected squares. The threshold corresponds to the increase in microwave loss and hence, reflection coefficient. As data in Fig. 3.5 show, the increase in the reflection coefficient is not always distinct. One can determine $h_{crit}$ value from these data as 2.7 ± 0.3 Oe. As discussed by Zhang *et al.* [1987], in the second reflection coefficient method the $h_{crit}$ value can be found by "exact" and "extrapolation" methods.

In the "exact" method, the threshold $h_{crit1}$ corresponds to the deviation of the experimental curve from the horizontal straight line drawn through the experimental

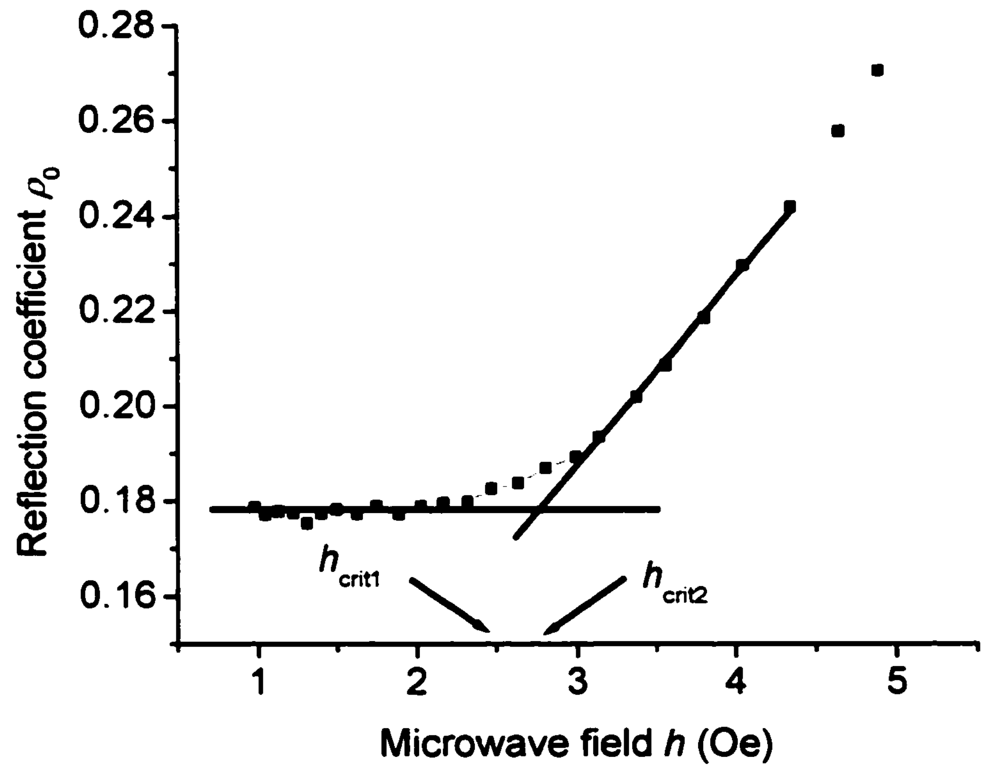


Figure 3.5. Reflection coefficient $\rho_0$ vs. microwave field $h$ for the pure Zn-Y disk. Parallel pumping at 8.993 GHz, applied field $H$ = 400 Oe. The closed squares indicate experiment. Deviation of the experimental curve from the horizontal straight line yields $h_{crit1}$, which corresponds to the exact method. Intersection of the straight lines yields $h_{crit2}$, which corresponds to the extrapolation method.

points in the linear region where the reflection coefficient is constant. The criterion is that the $\rho_0$ increases with increase in $h$ and the deviation is greater than the maximum error deviation of the points which form the horizontal line. In Fig. 3.5, the "exact" method yields $h_{crit1}$ value of 2.43 Oe. In the "extrapolation" method, the threshold $h_{crit2}$ value of 2.77 Oe corresponds to the intersection of the horizontal line and a line which is formed by the straight line drawn through the experimental points in the nonlinear region where the reflection coefficient linearly increases.

Unlike in the visual method, the $\rho_0$ vs. $h$ data do not give an unambiguous threshold specification. The choice between "exact" and "extrapolation" methods depends on the sample properties. If the sample is magnetized uniformly then the "exact" method is preferable. However, if sample is not magnetized uniformly, the "extrapolation" method is more reliable. For example, in the case of Zn-Y disk at 9 GHz pumping frequency the applied field value is about 400 Oe. The magnetization $4\pi M_s$ is 2330 G and the anisotropy field $H_A$ is about 9.4 kOe. In this case, the sample may not be uniformly magnetized and there are may be regions in the sample that have different magnetic state than the majority of the sample volume. The threshold for these regions may be lower than for the bulk of the sample. In order to find the threshold for the bulk of the sample, the second method should be used in this case. In general, one should always use the same threshold field determination method for the investigation of the particular sample.

Another important issue of the threshold field determination is a pulse width. As discussed in Chapter 2, spin wave instability processes involve the growth of parametric spin waves when the microwave field amplitude exceeds a specific threshold $h_{crit}$. There is always some characteristic time for such processes to develop and for the microwave field to reach its maximum in a cavity. Schlömann [1963] showed that if the microwave pulse is too short, the measured $h_{crit}$ values will be higher than for the infinite pulse width. The employed pulse width of 50 μs was long enough to avoid this effect. If a pulse width is too long, sample heating may occur and measurements will not be reliable (McKinstry *et al.* [1985]). The heating may be detected by a change in the pulse amplitude with pulse width and duty cycle. In the present work, heating effects were observed only well above the threshold and all precautions were taken to dismiss questionable data affected by heating.

### 3.4. Example Butterfly Curve Results

The test spin wave instability threshold measurements were performed for a sphere of a standard G113 polycrystalline YIG made by TransTech, Inc.. The sphere had a diameter of 2.5 mm. The example results were obtained for the parallel pumping configuration at 9 GHz. The $h_{crit}$ values were determined for the same results by visual and reflection coefficient methods discussed in the previous section.

Figure 3.6 shows the example butterfly curve, $h_{crit}$ vs. $H$ for parallel pumping at 9 GHz in the G113 polycrystalline YIG sphere. Open circles show $h_{crit}$ which was determined by the visual method. Closed squares show $h_{crit}$ which was determined by the reflection coefficient method. Compare first the visual and reflection coefficient methods. The data in Fig. 3.6 demonstrate that the results are independent of the threshold field determination method. One can see that these two methods yield identical $h_{crit}$. The number of points for the visual method is larger because it is about 20 times

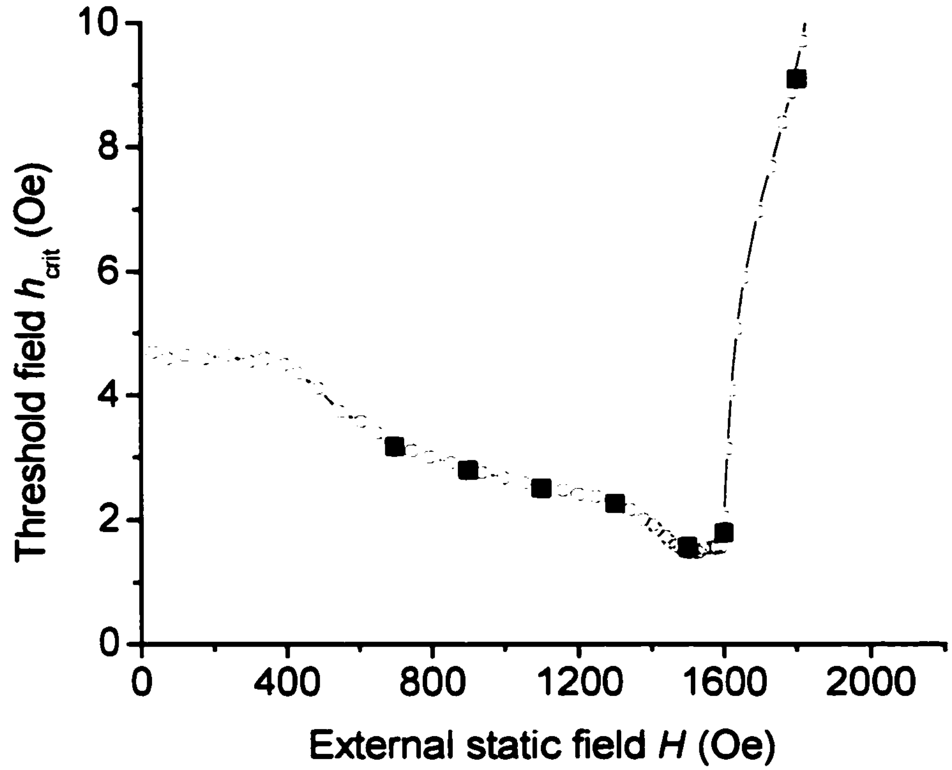


Figure 3.6. Spin wave instability threshold $h_{crit}$ as a function of the external static magnetic field $H$ for parallel pumping at 9 GHz in the G113 polycrystalline YIG sphere. The open circles indicate threshold observation by the visual method; the closed squares indicate threshold observation by the reflection coefficient method.

faster than the reflection coefficient method. These data demonstrate the practical advantages of the visual method which was utilized in this investigation when it was applicable.

The data in Fig. 3.6 represent a typical parallel pumping butterfly curve response for an isotropic polycrystalline sample. This is one of the simplest situations one can consider. The jump in the data at $H \sim 600$ Oe is attributed to demagnetizing effects. Above this field the sample is saturated. The measured $h_{crit}$ drops from about 3 Oe at $H =$ 600 Oe to about 1.5 Oe at $H = 1540$ Oe, where $h_{crit}$ has a minimum. This change corresponds to a $k$-dependent $\Delta H_k$. At the $H$ range of 1500 - 1600 Oe one can see a relatively flat $h_{crit}$ region which occurs in polycrystalline ferrites and will be discussed in detail in Chapter 5. In order to keep a reasonable scale the entire butterfly curve is not shown. It drastically goes up above $H \sim 1600$ Oe and terminates at the maximum achievable in the experiment $h_{crit}$ of 36 Oe at $H = 2070$ Oe.

One can take this experimental result and connect it with spin wave instability theory developed in Chapter 2 in order to demonstrate an example $h_{crit}$ data analysis. This is done to show how to connect the data with the theory. The butterfly curve is in a good agreement with the literature (Schlömann *et al.* [1960]). The $h_{crit}$ parallel pumping response in the case of isotropic polycrystalline ferrites is related to spin wave linewidth $\Delta H_k$ by

$$h_{crit} = \min_{\theta_k} \left\{ \frac{\omega \, \Delta H_k}{\omega_M \sin^2 \theta_k} \right\} \tag{3.6}$$

which follows from Eq. (2.65) and (2.75). The spin waves are excited at half pump frequency. The expression in the brackets represents the specific threshold $h_c$, as it is discussed in Chapter 2. If $\Delta H_k$ is independent of $k$ and $\theta_k$, the minimum threshold $h_{crit}$ is realized for $\theta_k$ = 90°. The azimuthal angle $\varphi_k$ of the parametrically excited spin waves can take any value, so that the entire plane of spin waves with wave vectors **k** and −**k** which lie in the $\theta_k$ = 90° plane is excited. The spin waves available for excitation are determined by the spin wave dispersion which depends on $H$. For an isotropic ferromagnet, the spin wave dispersion follows from Eq. (2.50) and may be written as

$$(\omega_k / |\gamma|)^2 = [H - H_{\rm dem} + Dk^2 + 4\pi M_s \sin^2\theta_k][H - H_{\rm dem} + Dk^2], \tag{3.7}$$

where the demagnetizing field $H_{\rm dem} = 4\pi N_z M_s$ for the sphere is $4\pi M_s/3$. For a 9 GHz excitation frequency, the spin wave frequency is 4.5 GHz.

Figure 3.7 shows the $h_{\rm crit}$ data from Fig. 3.6 and the $h_{\rm crit}$ response calculated from Eq. (3.6) with the available critical modes calculated from the spin wave dispersion of Eq. (3.7). For standard YIG, the parameters $4\pi M_s$ = 1750 G, $|\gamma|/2\pi$ = 2.8 GHz/kOe, and $D$ = $5.2\times10^{-9}$ Oe·cm$^2$/rad$^2$ were used in the analysis. The calculations were done for a constant spin wave linewidth $\Delta H_k$ value of 0.8 Oe. Arrows indicate the calculated parameters of the theoretical butterfly curve: demagnetizing field $H_{\rm dem}$, the static field $H_c$ which corresponds to the kink in $h_{\rm crit}$ curve, and the cutoff field $H_{\rm cut}$, where $h_{\rm crit}$ curve goes to infinity. These important parameters will be discussed below.

Below $H_{\rm dem}$ ~ 600 Oe, the sample is not saturated and there is a jump in the data. The calculated $h_{\rm crit}$ terminates at $H_{\rm dem}$. The expressions for $H_c$ and $H_{\rm cut}$ follow from the spin wave dispersion of Eq. (3.7). The field $H_c$ is the field at which spin waves with $\omega_k$ = $\omega/2$ and $\theta_k$ = 90° have $k$ = 0 and is given by

$$H_c = \sqrt{(\omega/2|\gamma|)^2 + (2\pi M_s)^2} - 2\pi M_s + H_{dem}. \tag{3.8}$$

The $H_{\rm cut}$ value corresponds to $k$ = 0 and $\theta_k$ = 0 and is given by

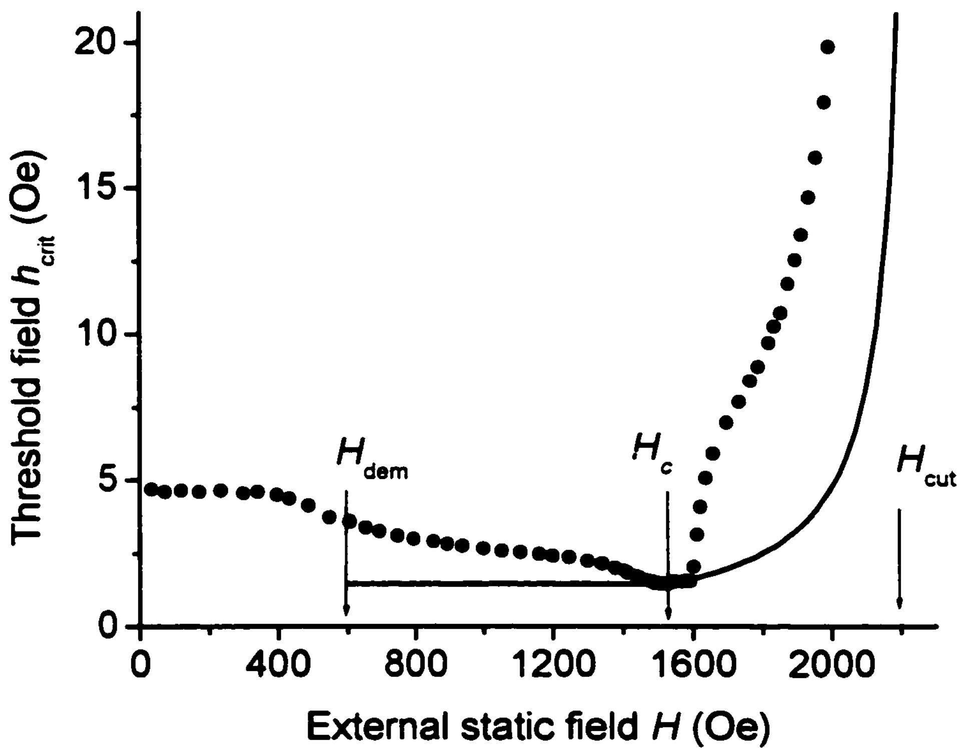


Figure 3.7. Spin wave instability threshold $h_{crit}$ as a function of the static external magnetic field $H$ for parallel pumping at 9 GHz in the G113 polycrystalline YIG sphere. The closed circles indicate the data, the solid line indicates the calculated $h_{crit}$ response. The calculations were done for a constant spin wave linewidth $\Delta H_k$ value of 0.8 Oe. Arrows indicate the demagnetizing field $H_{dem}$, the field $H_c$, and the cutoff field $H_{cut}$.

$$H_{cut} = \omega / 2|\gamma| + H_{dem} . \tag{3.9}$$

The theoretical $h_{crit}$ response can be understood better if one uses spin wave dispersion diagrams. These diagrams along with Eq. (3.6) identify excited critical modes $k$ and $\theta_k$.

Figure 3.8 shows the spin wave dispersion for different values of the external static field $H$. When $H$ is small, as in Fig. 3.8(a), $\omega/2$ lies above the upper boundary of the non-exchange spin wave spectrum and spin waves with non-zero wave numbers and $\theta_k = 90°$ are excited. When $H$ reaches $H_c$, as in Fig. 3.8(b), $k$ becomes zero. When $H$ is greater than $H_c$ but less than $H_{cut}$, as in Fig. 3.8(c), $k$ stays zero and $\theta_k$ decreases. When $H$ is greater than $H_{cut}$, as in Fig. 3.8(d), there are no spin waves with $\omega_k = \omega/2$ available for excitation and spin wave instability processes do not occur.

The spin wave band concept and parallel pumping at half pump frequency provide a very successful explanation of the high power data. There are three field intervals in Fig. 3.7, defined by $H_{dem}$, $H_c$, and $H_{cut}$, which have different physical origin of the $h_{crit}$ response. Below $H_{dem}$, the sample is not saturated and the theory is not applicable. In the field range from $H_{dem}$ to $H_c$, the $h_{crit}$ response is determined by the $k$-dependent spin wave linewidth $\Delta H_k$. In the field range from $H_c$ to $H_{cut}$, the $h_{crit}$ response is determined by the $\theta_k$-dependent spin wave linewidth $\Delta H_k$.

The butterfly curve provides information about the dependence of the spin wave linewidth parameter $\Delta H_k$ as a function of the wave number $k$. The spin waves with $\theta_k = 90°$ are excited perpendicular to the $H$ direction at the half pumping frequency of 4.5 GHz. It follows from Eqs. (3.7) and (3.8), that their wave numbers are given by

$$Dk^2 = H_c - H . \tag{3.10}$$

The $\Delta H_k$ vs. $k$ analysis applies to the $h_{crit}$ response in the field range from $H_{dem}$ to $H_c$.

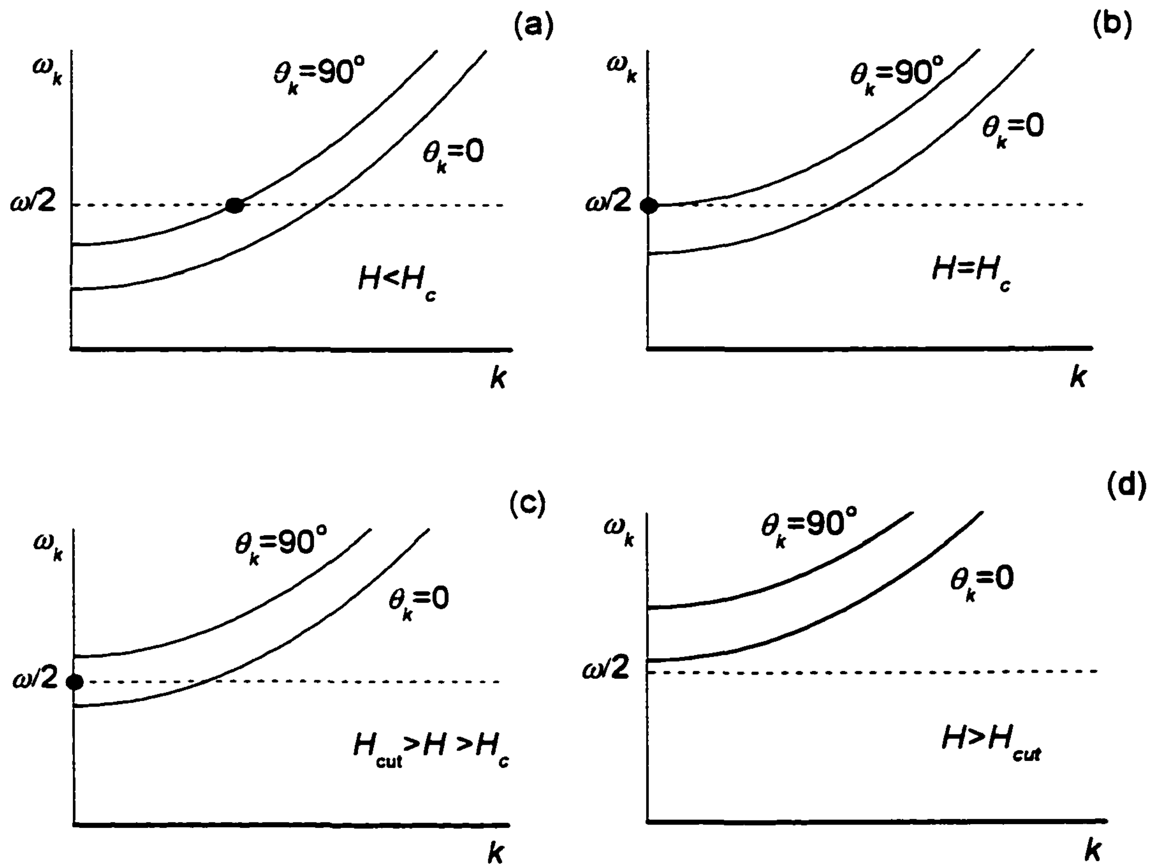


Figure 3.8. Relative positions of the spin wave spectra and the parallel pumping half-frequency $\omega/2$. Dots indicate critical modes at $\omega_k = \omega/2$. (a) At $H < H_c$ spin waves with $k > 0$ and $\theta_k = 90°$ are excited, (b) at $H = H_c$ spin waves with $k = 0$ and $\theta_k = 90°$ are excited, (c) at $H_c < H < H_{cut}$ spin waves with $k = 0$ and $\theta_k < 90°$ are excited, and (d) no spin waves are available at $\omega_k = \omega/2$.

Figure 3.9 shows the spin wave linewidth parameter $\Delta H_k$ at 4.5 GHz as a function of the wave number $k$. Squares indicate the experimental data, the straight line shows the linear fit for wave numbers in the range $0 - 3.5\times10^5$ rad/cm. This linear fit is given by

$$\Delta H_k(k) = \Delta H_{k=0} + Bk \, , \tag{3.11}$$

where $\Delta H_{k=0}$ is 0.81 Oe and $B$ is $2.48\times10^{-6}$ Oe·cm/rad. These parameters are in a good agreement with data for large grain polycrystalline YIG (Patton [1969]). The linear $\Delta H_k$ vs. $k$ dependence will be discussed in Chapter 5 for hipped polycrystalline YIG.

These example results show what one can expect from the spin wave instability threshold measurements and the $h_{crit}$ analysis. As the result of these measurements one can obtain the $h_{crit}$ vs. $H$ dependence for various orientation of the sample, the static external field, and the linear polarized microwave field. The analysis of this dependence yields the excited critical modes and the spin wave linewidth parameter $\Delta H_k$ as a function of the critical mode wave number and direction.

The $h_{crit}$ response in single crystal YIG differs from the $h_{crit}$ response in polycrystalline YIG. In single crystal YIG, the minimum of $h_{crit}$ is distinct and its position depends on the orientation of $H$ with respect to the crystallographic axes. These features will be considered in Chapter 4 where the $h_{crit}$ data on single crystal LPE YIG films with small anisotropy are given. The discussion on spin wave instability in polycrystalline YIG will be developed in more details in Chapter 5 where the data on bulk polycrystalline hipped YIG and the analysis are presented.

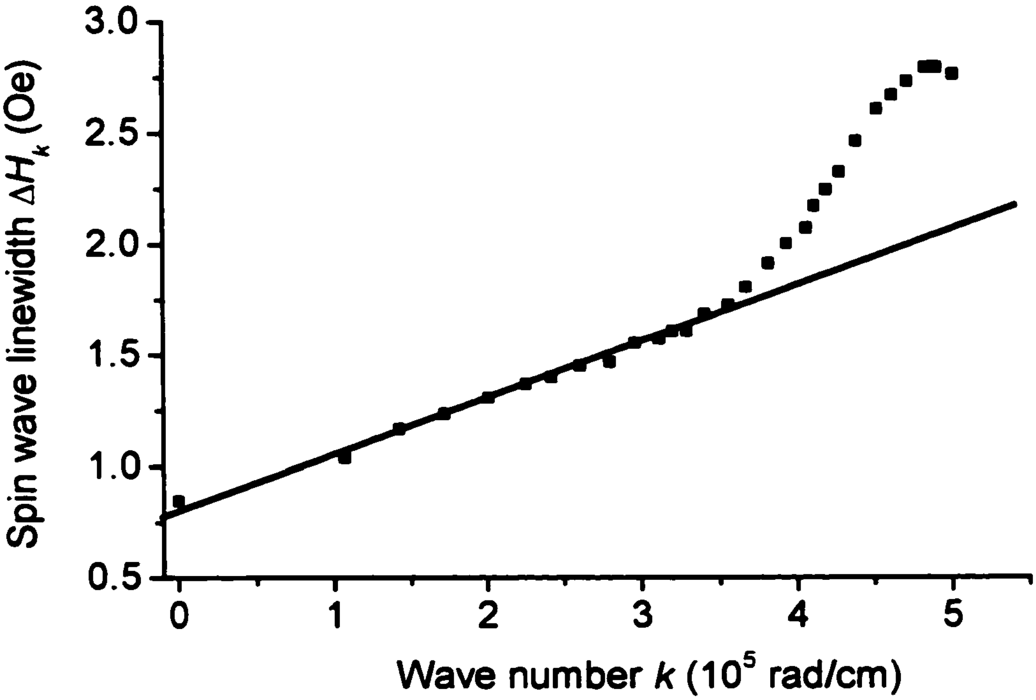


Figure 3.9. Spin wave linewidth $\Delta H_k$ as a function of spin wave wave number $k$ at 4.5 GHz in the G113 polycrystalline YIG sphere. The closed squares indicate the data, the straight line indicates theoretical fit.

# CHAPTER 4

# HIGH POWER MICROWAVE PROPERTIES OF LPE YIG THIN FILMS

This chapter gives the results of the spin wave instability threshold measurements in single crystal LPE YIG (110) oriented thin films. The 9 GHz parallel pumping measurements were performed for different diameter disk samples and for different film orientations with respect to the external static field. The spin wave linewidth analysis showed that the $k = 0$ extrapolated spin wave linewidth was 0.18 Oe, close to the lowest reported values for bulk single crystal YIG (Yakovlev *et al.* [1971]).

Section 4.1 gives an overview of the data on FMR linewidth and the specifics of the $h_{crit}$ measurements for LPE YIG disks. Section 4.2 presents experimental parallel pumping $h_{crit}$ results for normally magnetized disks of different diameter and gives a spin wave linewidth analysis of these results. Section 4.3 gives the corresponding results for parallel pumping for in-plane magnetized disks with the external static field along three main crystallographic axes, [100], [110], and [111]. The analysis of the data shows that although $h_{crit}$ depends on the static field direction, the spin wave linewidth does not depend on the spin wave propagation direction.

## 4.1. Overview

The investigated single crystal LPE YIG disk samples were fabricated in Prague, Czech Republic. As discussed in Chapter 3, these samples had various Ca additions. The FMR linewidth $\Delta H_0$ measurements at 9.53 GHz on the disks of various diameter and composition showed that (1) for normally magnetized disks, $\Delta H_0$ can increase with the increase in the disk diameter and (2) for in-plane magnetized disks, $\Delta H_0$ significantly depends on the direction of the static field relative to the crystallographic axes (Marysko *et al.* [2001]). For $H$ along the [100] axis, $\Delta H_0$ was about 0.5 Oe. For $H$ along the [110] axis, $\Delta H_0$ was about 1.0 Oe.

The 9 GHz parallel pumping measurements showed more consistent results than the FMR data. First, $\Delta H_{k=0}$ consistently decreased with increase in Ca content. Second, the deviation of the minimum $h_{crit}$ for the different samples with the same Ca content was an order of magnitude smaller than deviation in $\Delta H_0$ for the same samples. Overall, the $h_{crit}$ data presented below showed no effects that were observed for $\Delta H_0$. On the contrary, the minimum $h_{crit}$ was largest for the smallest diameter sample.

This is related to the fact that the number of the defects and inhomogeneities in the sample increases with the sample size. The number of the scattering centers increases and $\Delta H_0$ increases too. In the case of spin wave instability, the spin waves are excited in the local areas of the sample (Sparks [1964]). The lowest threshold is realized in the area with the most ideal structure. An increase in sample size increases the probability of the existence of such an area with the most ideal structure. Therefore, in contrast with $\Delta H_0$, a smaller sample size may yield a larger threshold. Therefore, in this case of insufficient macroscopic quality films, spin wave linewidth is a better measure of microwave loss than $\Delta H_0$.

The spin wave instability processes in thin ferrite films differ from these processes in bulk ferrite materials. Effects such as a butterfly curve fine structure and magnetostatic wave excitation (Kalinikos *et al.* [1985] and Wiese *et al.* [1994]) may be present. For the investigated LPE YIG films, the fine structure was not observed. This is presumably because the film thickness was relatively large and, moreover, undulation was observed. The data could be analyzed based on a bulk exchange spin wave approximation. The parallel pumping data also showed that the bulk spin wave approximation was valid for the data analysis.

The parallel pumping measurements were made at 8.99 GHz with the high Q cylindrical cavity described in Section 3.2. All of the $h_{crit}$ data were obtained by the visual method discussed in Section 3.3. Three samples with different diameter were investigated for perpendicular configuration and one of the samples was also measured for in-plane configuration. The small volume of the samples, especially for the smallest diameter sample, pushed the visual technique to the limit, but the accuracy was still adequate. A related problem is that high $k$ spin waves at low $H$ have a smaller coupling with the $k$ = 0 microwave magnetic field than low $k$ spin waves and the change in the pulse shape is less pronounced. Therefore, the parallel pumping measurements were done first for the different diameter samples in order to investigate the dependence of $h_{crit}$ on the film diameter. The external static field was normal to the film surface.

### 4.1. Parallel Pumping at 9 GHz in Normally Magnetized Films

Figure 4.1 shows the threshold $h_{crit}$ as a function of the external static magnetic field $H$ for parallel pumping at 9 GHz in the three normally magnetized LPE YIG disks. The values of the disk diameter $d$ are indicated in the graph. The focus is on the butterfly curve minimum and corresponding lowest $\Delta H_k$ values. The position of the minimum $h_{crit}$ for all three curves is at about 2.65 kOe. The curves were terminated where the sensitivity of the threshold detection became insufficient to obtain the data. The 3 and 4 mm diameter disks yield the same threshold for low $k$ spin waves. For these samples, there are complications below the $h_{crit}$ minimum that remain unexplained. They may be due to the variation of the microwave magnetic properties from sample to sample. It is interesting that $h_{crit}$ is notably larger for the smaller sample with $d$ = 1.5 mm, which is opposite to the FMR linewidth results. This can be related to the local nature of the spin wave instability processes which was discussed in the previous section.

The data in Fig. 4.1 were analyzed to obtain the spin wave linewidth $\Delta H_k$ dependence as a function of wave number $k$, based on the spin wave instability analysis for isotropic materials. Equation (3.6) relates $h_{crit}$ and $\Delta H_k$ for $\theta_k$ = 90°. The wave number value was obtained from Eq. (3.10) and the $H_c$ value which corresponds to the minimum of $h_{crit}$. The $H_c$ value calculated from Eq. (3.8) and standard parameters for YIG given in Section 3.4 was 2.69 kOe, which is slightly larger than the experimental $H_c$ of 2.65 kOe. For the perpendicular configuration, all anisotropy effects are ignored but they will be taken into account later for the case of in-plane magnetized disks.

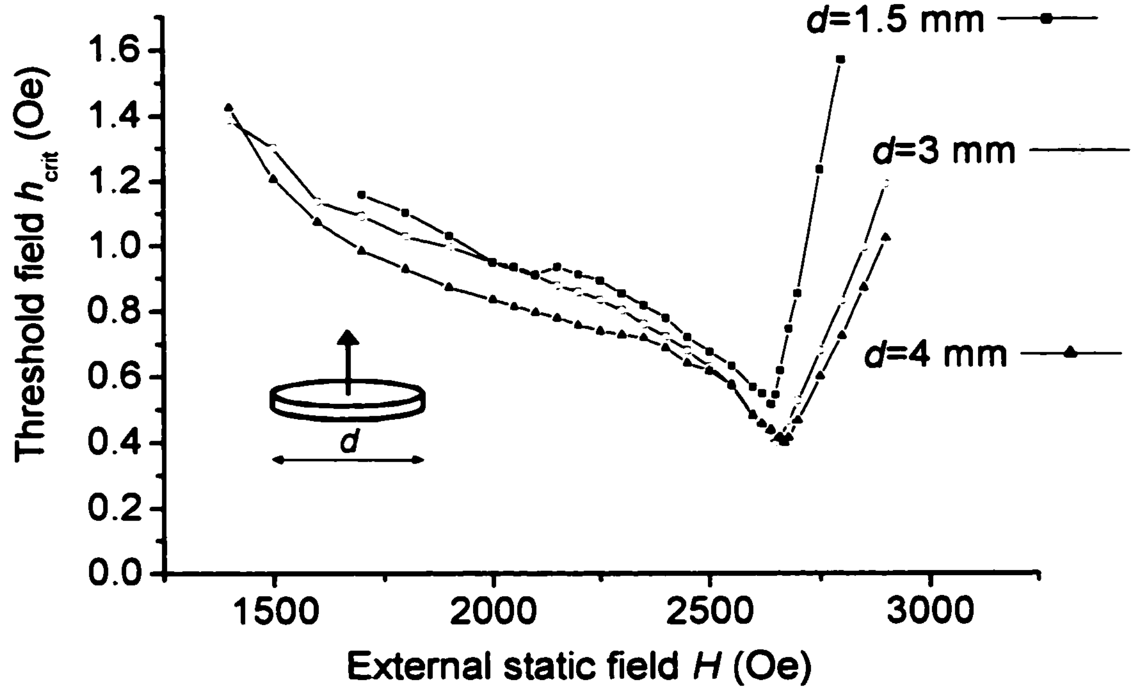


Figure 4.1. Spin wave instability threshold $h_{crit}$ as a function of the external static magnetic field $H$ for parallel pumping perpendicular to plane at 9 GHz in the LPE YIG disks. The values of the disk diameter $d$ are indicated in the graph.

Figure 4.2 shows the spin wave linewidth parameter $\Delta H_k$ as a function of the wave number $k$. From the formalism of Chapter 3, this corresponds to a spin wave frequency of 4.5 GHz and $\theta_k = 90°$. The $\Delta H_k$ values for the specific diameter samples are indicated by the same symbols as in Fig. 4.1. Straight solid lines indicate linear fits to the data. The $\Delta H_k$ response is linear and is described by Eq. (3.10). The zero intercepts are $\Delta H_{k=0} = 0.220 \pm 0.005$ Oe for $d = 1.5$ mm, $\Delta H_{k=0} = 0.176 \pm 0.004$ Oe for $d = 3$ mm, and $\Delta H_{k=0} = 0.184 \pm 0.006$ Oe for $d = 4$ mm. The slopes are $B = (9.5 \pm 0.2)\times10^{-7}$ Oe·cm/rad for $d = 1.5$ mm, $B = (9.8 \pm 0.1)\times10^{-7}$ Oe·cm/rad for $d = 3$ mm, and $B = (7.8 \pm 0.2)\times10^{-7}$ Oe·cm/rad for $d = 4$ mm. In the fits, only linear portions of the data were used. High $k$ points were excluded because of the demagnetizing effects. Low $k$ points were excluded because the bulk spin wave approximation does not work. The linear $\Delta H_k$ increase with $k$ in a pure bulk single crystal YIG is often taken as a signature of intrinsic three magnon confluence processes (Gurevich and Melkov [1996]).

One can see that the intersection of the straight lines with the vertical axis yields smaller value than the minimum $\Delta H_k$ value for each sample. As discussed by Sparks [1964], the excited spin waves which correspond to minimum $\Delta H_k$ have some non-zero $k$ value. The deviation from the linear behavior in Fig. 4.2 occurs for k < $5\times10^4$ rad/cm which is much larger than the magnetostatic mode limit $\pi/d$. The excited spin waves have even larger wave numbers so that they remain exchange spin waves and their group velocity is sufficiently large. Therefore, the real $\Delta H_{k=0}$ for $k = 0$ can be obtained by intersection of the linear fit with the vertical axis. The $\Delta H_{k=0}$ difference between three samples is smaller than the minimum $\Delta H_k$. One can conclude that the reason for the larger $\Delta H_{k=0}$ for the sample with $d = 1.5$ mm is related to the local

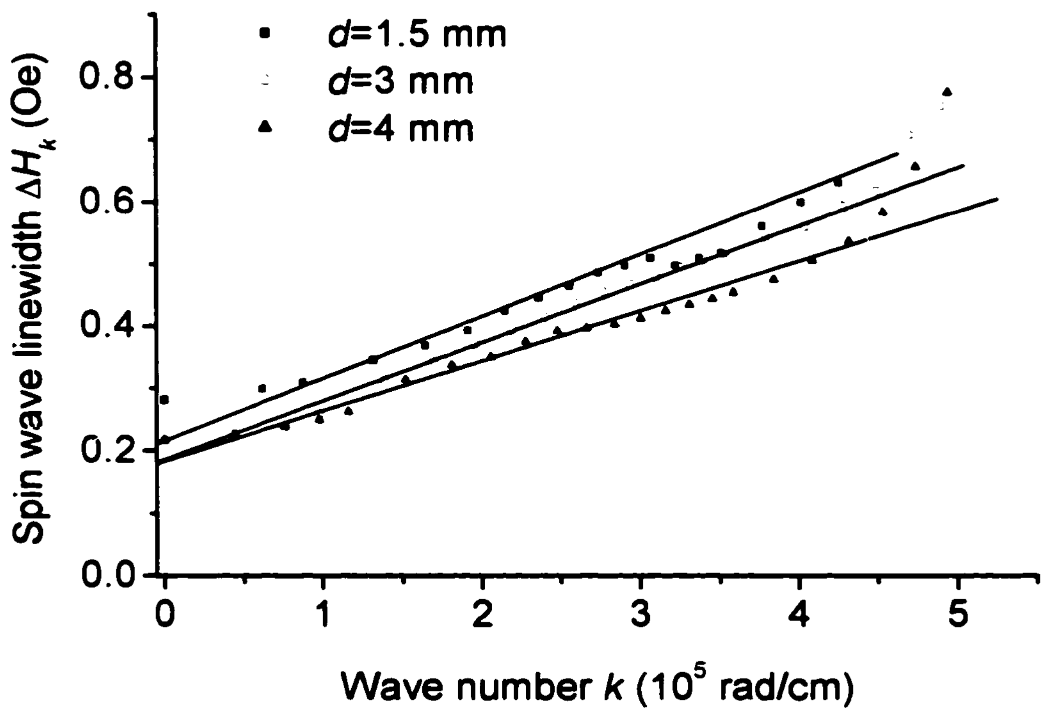


Figure 4.2. Spin wave linewidth $\Delta H_k$ as a function of spin wave wave number $k$ at 4.5 GHz in the LPE YIG disks. The values of the disk diameter $d$ are indicated in the graph. The solid straight lines indicate linear fits to the data.

nature of the spin wave instability processes. The other two samples yield exactly the same $\Delta H_{k=0}$ of 0.18 Oe and the minimum $\Delta H_k$ of 0.22 Oe. It implies that these samples have the same intrinsic microwave loss mechanisms and there is no lack of sensitivity if the sample diameter is at least 3 mm. The slight difference for larger $k$ values can be explained by the deviation in microstructure and possible non-uniform magnetization of the larger sample caused by edge effects.

If the minimum $\Delta H_k$ corresponds to some non-zero $k$, then the theoretical $H_{cl}$ which corresponds to $k = 0$ should be slightly larger than $H_c$ which corresponds to the minimum $h_{\text{crit}}$. For the 3 mm disk $H_c$ was 2.64 kOe. If one takes $H_{cl}$ = 2.68 kOe then the $k$ value for any given $\Delta H_k$ is larger and $\Delta H_{k=0}$ will be 0.14 Oe. This value is close to the theoretical limit predicted from an intrinsic Kasuya-Le-Craw two magnon-one phonon process, which is present even for an ideally pure YIG (Sparks [1964]). As a good approach to the value $\Delta H_{\text{KL}}$ for pure single crystal YIG one can take the spin-wave linewidth $\Delta H_{k=0}$ = 0.135 Oe measured at the parallel pumping frequency of 11.4 GHz which corresponds to the magnon frequency of 5.7 GHz (Le Craw and Spencer [1962]). This means that the investigated samples were of high quality and had structure similar to ideal YIG. Among all investigated samples, along with those not mentioned in the present study, the lowest minimum $\Delta H_k$ value of 0.18 Oe was obtained for the 3 mm disk sample with x = 0.016 where x is the Ca concentration per formula unit.

Because of the ambiguity in the choice of $H_{cl}$, it is always necessary to compare the minimum $\Delta H_k$ for different samples or configurations. The question of the wave number $k$ which corresponds to the minimum $\Delta H_k$ has not been clarified in the literature and will be discussed in Chapter 7. In order to keep consistency, throughout the present work it is assumed that the value of $H_{c1}$ is equal to the $H_c$ value which is found from the experiment.

The butterfly curve in Fig. 4.1 for the 3 mm disk was fitted to some $\Delta H_k$ function of $k$ and $\theta_k$. For $H$ below $H_c$, the $\Delta H_k$ fit was a linear function of $k$. For $H$ above $H_c$, the wave number is zero and the best fit is realized for the $(\sin 2\theta_k)^2$ function. Figure 4.3 shows the fit to the $h_{crit}$ data of Fig. 4.1 for the 3 mm LPE YIG disk. The squares show the experimental data. The solid line represents the fit $\Delta H_k$ function of the form (Wiese *et al.* [1994])

$$\Delta H_k(k) = \Delta H_{k=0} + Bk + C(\sin 2\theta_k)^2, \qquad (4.1)$$

with parameters $\Delta H_{k=0}$ = 0.18 Oe, $B = 9.8\times10^{-7}$ Oe·cm/rad, and $C$ = 0.25 Oe adjusted to match the data. The linear in $k$ part corresponds to the fit in Fig. 4.2. The values of these parameters for 9 GHz parallel pumping in bulk single crystal YIG are $\Delta H_{k=0}$ = 0.132 Oe, $B = 4.9\times10^{-7}$ Oe·cm/rad, and $C$ = 0.163 Oe (Yakovlev *et al.* [1971], Patton [1979]). One can see that $\Delta H_{k=0}$ is somewhat larger for the investigated LPE YIG films than for pure bulk YIG. The $B$ and $C$ parameters are about 2 times larger. The non-zero $C$ shows that $\Delta H_k$ increases when $\theta_k$ decreases from 90°. This observation was made even in the first work on parallel pumping by Schlömann *et al.* [1960].

Such a big value of the $C$ parameter in the normally magnetized films is related to the direction of the excited spin waves. When $k$ is non-zero, spin waves propagate at $\theta_k$ = 90°. The magnetization is normal to the plane of the film and disk and $\theta_k$ = 90° spin waves can propagate along any direction in the film plane because the azimuthal angle $\varphi_k$ is not specified. As discussed in Chapters 2 and 3, when $H$ increases past $H_c$, the wave number $k$ becomes small and $\theta_k$ decreases. The smallest $\theta_k$ of 53°

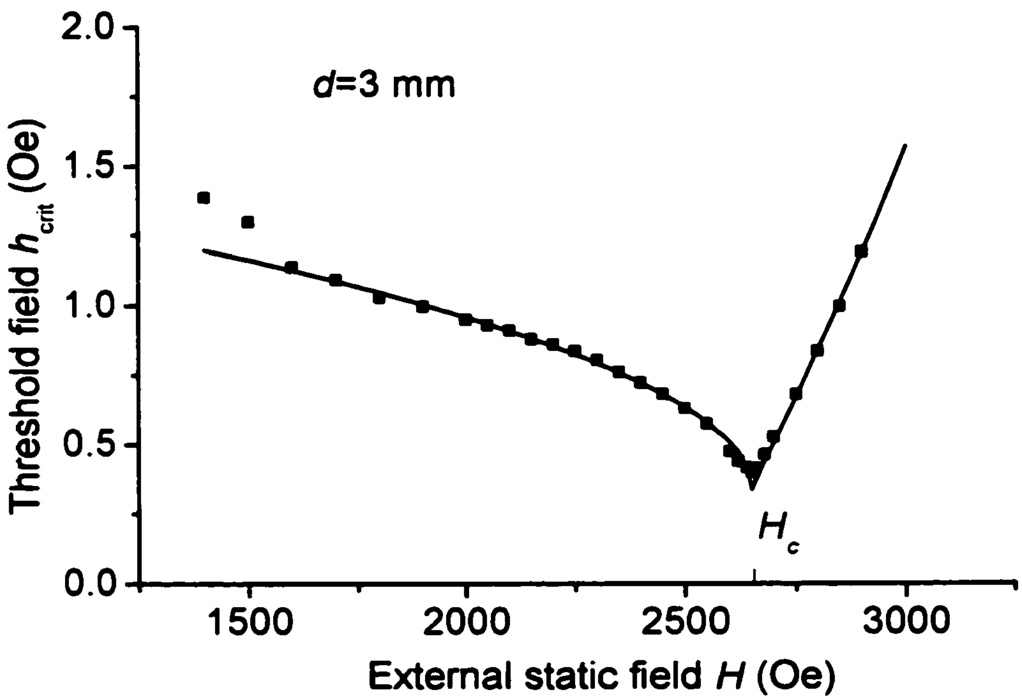


Figure 4.3. Spin wave instability threshold $h_{crit}$ as a function of the external static magnetic field $H$ for parallel pumping perpendicular to plane at 9 GHz in the 3 mm LPE YIG disk. The closed squares indicate experiment, the solid line indicates theoretical fit to the data. The field position of the butterfly curve minimum is at $H_c$.

corresponds to $H = 2.9$ kOe in Fig. 4.3. When $\theta_k$ is less than 90°, excited spin waves propagate at some non-zero angle to the film plane. This means that the spin wave propagation may be impeded by surface boundaries because spin waves do not propagate in the film plane. Similar effects will be considered for polycrystalline YIG in Chapter 5 where the grain boundaries act as scattering centers for spin waves. Moreover, these spin waves have small $k$. These arguments explain the large value of the $C$ parameter. The butterfly curve behavior above $H_c$ for an in-plane magnetized disk is different and will be discussed in the next section.

This section demonstrated the results of the parallel pumping measurements in the normally magnetized (110) LPE YIG disks. The $h_{crit}$ and $\Delta H_k$ data for three disks of different diameter were in agreement. In this case, spin waves with non-zero $k$ can propagate along any of the crystallographic axes, such as [100], [110], and [111]. If spin wave linewidth depends on the crystallographic direction, this dependence will not be distinguishable. But if a (110) film is magnetized in-plane along one of the crystallographic axes, spin waves will be excited only in the direction perpendicular to $H$ and in the plane of the film because film surface boundaries should impede spin wave excitation perpendicular to the film plane, especially for low wave numbers. The next section will consider parallel pumping in the in-plane magnetized LPE YIG film.

## 4.2. Spin Wave Linewidth Angular Dependence in In-plane Magnetized Films

As discussed in Section 4.1, FMR linewidth measurements on the in-plane magnetized (110) oriented LPE YIG films showed significant changes in $\Delta H_0$ if $H$ is applied along different crystallographic axes (Marysko *et al.* [2001]). The similar parallel pumping measurements were performed for the in-plane magnetized 3 mm disk. The objective of these measurements was to investigate the $\Delta H_k$ dependence on the orientation of $H$ with respect to crystallographic axes like for the in-plane FMR linewidth measurements.

Figure 4.4 shows $h_{crit}$ as a function of the external static magnetic field $H$ for parallel pumping at 9 GHz in the in-plane magnetized 3 mm LPE YIG disk. Parallel pumping butterfly curves are shown for $H$ along each of the three principal crystallographic axes, [100], [110], and [111]. The $H$ direction is indicated in the graph by these axes.

One can see that butterfly curves for these three orientations are quite similar except for a shift in $H$. The $h_{crit}$ response is very similar for $H$ along the [110] and [111] axes and is slightly different for $H$ along [100] axis. The minimum $h_{crit}$ and its field position $H_c$ are different for [100] and the two other orientations. The difference in the minimum $h_{crit}$ is about 5 % and the effect is small. For $H$ along [100], $H_c$ is largest. For $H$ along [111], $H_c$ is smallest. This is due to the effect of the small but not negligible cubic magnetocrystalline anisotropy. The anisotropy field in YIG is negative, the hard direction is along [100] and the easy direction is along [111]. When $H$ is applied along the easy direction, $H_c$ is smaller than when $H$ is applied along the hard direction. The data in Fig. 4.1 support these arguments.

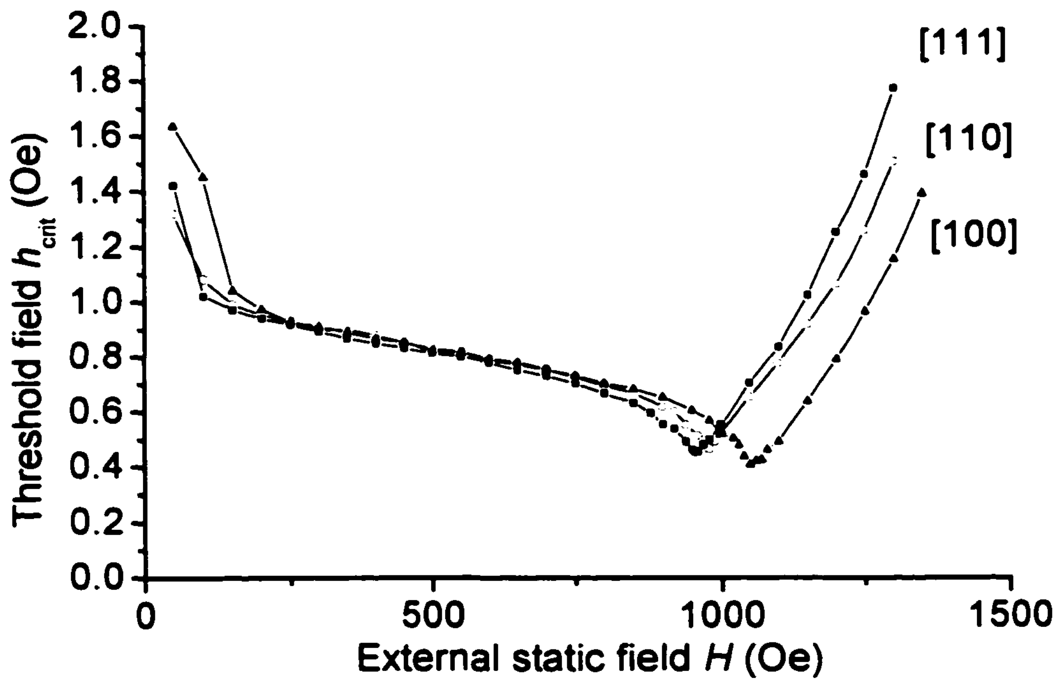


Figure 4.4. Spin wave instability threshold $h_{crit}$ as a function of the external static magnetic field $H$ for in-plane parallel pumping at 9 GHz in the 3 mm LPE YIG disk. The static field is applied along one of the three crystallographic axes which are indicated in the graph.

Consider first the position of the minimum $h_{crit}$ and the corresponding value of $H_c$. Although thin ferrite films may have additional types of growth induced anisotropy (Gurevich and Melkov [1996]), in the present work it is assumed that there is only cubic anisotropy similar to that in bulk single crystal YIG. The expression for $H_c$ can be obtained in the same way as Eq. (3.8) with anisotropy $H_A$ taken into account. The fields $H_c$ may be written explicitly only for $H$ along the hard [100] and easy [111] direction. These fields are given by

$$[100] \qquad H_c = \sqrt{(\omega/2|\gamma|)^2 + (2\pi M_s)^2} - 2\pi M_s - 2H_A + 4\pi N_z M_s \tag{4.2}$$

and

$$[111] \qquad H_c = \sqrt{(\omega/2|\gamma|)^2 + (2\pi M_s)^2} - 2\pi M_s + \frac{4}{3}H_A + 4\pi N_z M_s . \tag{4.3}$$

One can see that these two directions yield the different values of $H_c$. The difference in $H_c$ is equal to $10|H_A|/3$. The experimental $H_c$ values in Fig. 4.4 yield the anisotropy field $H_A = -28.5$ Oe. Note, that the value of the anisotropy field in bulk YIG is $H_A = -44 \pm 2$ Oe (Winkler [1980]).

Based on Eqs. (4.2) or (4.3), it is possible to find $4\pi M_s$ from the values of $H_c$ in Fig. 4.4. The value of the demagnetizing factor $N_z$ in the case of the oblate ellipsoid of revolution which resembles a disk may be written as (Osborn [1948])

$$N_z = \frac{1}{2(w^2-1)}\left(\frac{w^2}{\sqrt{w^2-1}}\sin^{-1}\left[\frac{\sqrt{w^2-1}}{w}\right] - 1\right), \tag{4.4}$$

where $w = d/t$ is the aspect ratio of the sample and $t$ is the sample thickness. Note that $N_z$ is the demagnetizing factor along the $H$ direction which is in-plane. For the 3 mm diameter disk, $N_z$ equals 0.003. Then Eq. (4.2) yields a $4\pi M_s$ value of 1620 G. This value is smaller than $4\pi M_s$ in bulk YIG. The same formalism can be applied to the normally magnetized disk in the previous section. In this case, $4\pi M_s$ is approximately 1610 G. The calculated $4\pi M_s$ values are very susceptible to $H_A$. One can conclude that these films have different properties than standard bulk YIG. Because of this, $4\pi M_s$ = 1610 G and $H_A$ = −28.5 Oe will be used in the analysis in this chapter.

The data in Fig. 4.4 were analyzed to obtain the spin wave linewidth $\Delta H_k$ dependence as a function of wave number $k$. The data in Fig. 4.4 show that anisotropy is important and therefore one can use the working equations from Chapter 2. Equation (3.4) does not include anisotropy and Eqs. (2.65) and (2.66) were used to derive the expression for $h_c$ and analyze the data. The expression for $h_c$ may be written as

$$h_c = \frac{\omega \Delta H_k}{\left|\omega_M \sin^2\theta_k \exp(2i\varphi_k) - |\gamma| M_s (A_{xx} - A_{yy})\right|}, \tag{4.5}$$

which follows from Eqs. (2.48), (2.49), and (2.66). For cubic anisotropy and the static magnetization $\mathbf{M}_s$ in the (110) plane, anisotropy tensor components $A_{xx}$ and $A_{yy}$ may be written as (Patton [1979])

$$A_{xx} = -2H_A(1 - 3\sin^2\theta_M)(1 - \frac{3}{2}\sin^2\theta_M) \tag{4.6}$$

and

$$A_{yy} = -2H_A(1 - \frac{3}{2}\sin^2\theta_M), \tag{4.7}$$

where the angle $\theta_M$ is the angle between the [100] axis and $\mathbf{M}_s$. The right handed ($x$, $y$, $z$) frame has an $x$-axis in the film plane, a y-axis perpendicular to the film, and a $z$-axis along $\mathbf{M}_s$ which is assumed to be parallel to $\mathbf{H}$. This assumption is valid when the anisotropy field is small compared to $H$.

The threshold field for the special case of the negative anisotropy field may be written as

$$h_c = \frac{\omega \Delta H_k}{\left| \omega_M \sin^2\theta_k \exp(2i\varphi_k) + 6|\gamma||H_A|\sin^2\theta_M (1 - \frac{3}{2}\sin^2\theta_M) \right|}. \tag{4.8}$$

Note that the term with $H_A$ changes sign when $\theta_M$ changes from 0 to 90°. This corresponds to the $\mathbf{M}_s$ rotation from the [100] axis to the [110] axis. The $H_A$ term in the denominator changes sign at $\theta_M$ = 57° which corresponds to the [111] axis. When $\mathbf{M}_s$ is along the [100] or [111] axis, the term with $H_A$ goes to zero and the threshold field $h_c$ is not a function of $\varphi_k$. In this case, the minimum threshold field $h_{crit}$ is realized for $\theta_k$ = 90° and Eq. (4.8) is the same as Eq. (3.6). When $\mathbf{M}_s$ is along the [110] axis, the threshold field is less than for the other two axes and realizes for $\theta_k$ = 90° and $\varphi_k$ = 90°. This direction is normal to the film plane. As discussed in the previous section, the excited spin waves cannot propagate in this direction.

The two conditions, the in-plane propagation of the spin waves and $\theta_k$ = 90°, force $\varphi_k$ to be 0 or 180°. In the case of the bulk YIG the minimum $h_{crit}$ is realized for $\mathbf{M}_s$ along the [110] axis, but in the investigated (110) films the $\mathbf{M}_s$ alignment along the [110] axis yields a higher $h_{crit}$ than other directions. It is clear that this statement is valid only for isotropic $\Delta H_k$. The data in Fig. 4.4 support these considerations. The $h_{crit}$ values are the highest for $\mathbf{M}_s$ along the [110] axis. In the case of $\mathbf{M}_s$ along the [111] axis, the excited spin waves do not propagate along any particular crystallographic direction because there is no main axis which is in the (110) plane and perpendicular to the [111] axis. Therefore, the analysis will focus only on $\mathbf{M}_s$ along the [110] and [100] axes. These directions correspond to the spin wave propagation directions along the [100] and

[110] axes, respectively. The $\Delta H_k$ values were obtained from the $h_{crit}$ data in Fig. 4.4 and Eq. (4.8) with the following parameters: $\theta_k = 90°$ for $\mathbf{M}_s$ along the [100] axis, $\theta_k = 90°$ and $\varphi_k = 0$ for $\mathbf{M}_s$ along the [110] axis, and $\theta_k = 90°$ for $\mathbf{M}_s$ along the [111] axis.

Figure 4.5 shows the spin wave linewidth parameter $\Delta H_k$ at the half pump frequency of 4.5 GHz as a function of wave number $k$ for $\theta_k = 90°$ spin waves. The symbols that show the data correspond to the same $H$ directions as in Fig. 4.4.

One can see that for very small $k$, the $\Delta H_k$ values for the spin waves propagating along the different axes are very close. The $\Delta H_k$ deviation for the same $k$ is less than 10 %. For $\mathbf{M}_s$ along the [100] axis and the excited spin waves along the [110] axis, the minimum $\Delta H_k$ is 0.21 Oe. For $\mathbf{M}_s$ along the [111] axis, the minimum $\Delta H_k$ is 0.23 Oe. For $\mathbf{M}_s$ along the [110] axis and excited spin waves along the [100] axis, the minimum $\Delta H_k$ is 0.22 Oe. If one neglects anisotropy in Eq. (4.8) this value will be 0.24 Oe. Note that above anisotropy considerations yield better agreement than if one neglects anisotropy. It is also clear that these considerations work only for relatively small wave numbers. For larger $k$, the condition of the in-plane spin wave propagation is less strict and, as it is shown in Fig. 4.4 and 4.5, the calculation of the $\Delta H_k$ values does not require a specific $\varphi_k$ direction. In such a case, when the $H_A$ term in Eq. (4.8) is neglected, the two curves for [100] and [110] axes in Fig. 4.5 would be very close for $k$ above $10^5$ cm$^{-1}$.

Figure 4.4 shows that the response for all three directions is similar. Below $H_c$, the butterfly curve behavior is similar to one shown in Fig. 4.1 for normally magnetized films. This behavior is determined by linear $\Delta H_k$ vs. $k$ response shown in Fig. 4.5. Above $H_c$, the butterfly curve behavior differs from one shown in Fig. 4.1. The origin of this difference follows from the fit to the data and surface boundary

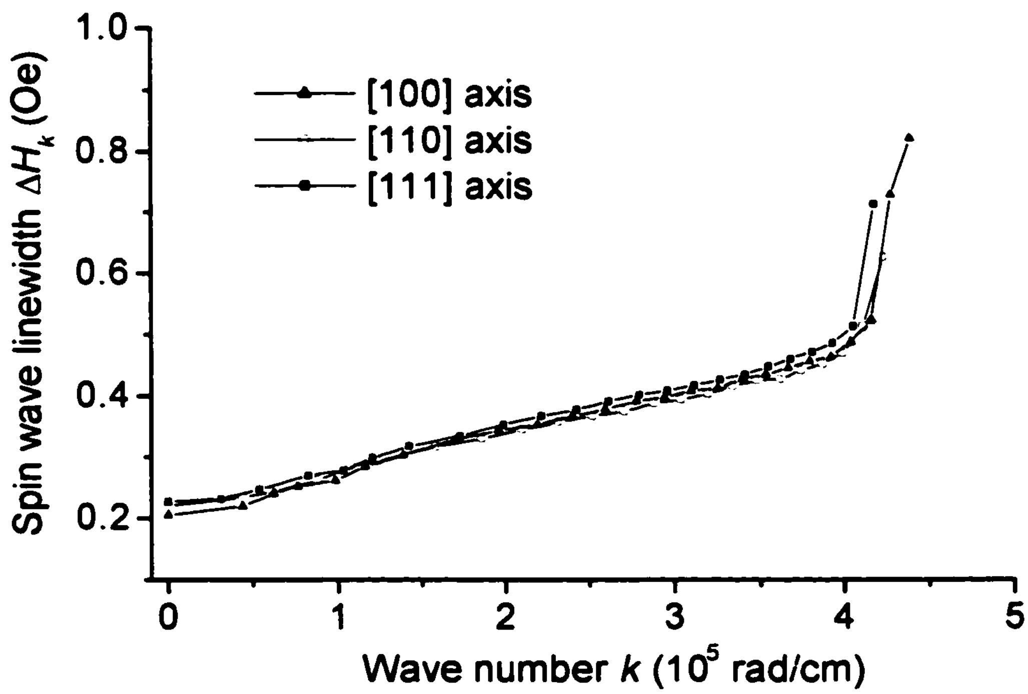


Figure 4.5. Spin wave linewidth $\Delta H_k$ as a function of spin wave wave number $k$ at 4.5 GHz for the in-plane magnetized 3 mm LPE YIG disk. The static field is along one of the crystallographic axes which are indicated in the graph.

considerations for the $C$ parameter developed in the previous section. The same fitting procedure of Eq. (4.1) was applied to the data in Fig. 4.4 for $\mathbf{M}_s$ along the [100] axis.

Figure 4.6 shows the fit to the $h_{crit}$ data of Fig. 4.4 for the 3 mm LPE YIG disk magnetized in-plane along the [100] axis. The squares show the experimental data. The solid line represents the fit of Eq. (4.1). This fit yields the parameters $\Delta H_{k=0}$ = 0.20 Oe, $B$ = $6.7\times10^{-7}$ Oe·cm/rad, and $C$ = 0.10 Oe.

The $\Delta H_{k=0}$ and $B$ values are similar to values for normally magnetized films. The $C$ value for the in-plane magnetized film is much smaller than $C$ = 0.25 Oe for the normally magnetized film. This fact has the following explanation. In the case of the in-plane magnetized film, when $\theta_k$ is less than 90°, the excited spin waves still propagate in the film plane. This means that the spin wave propagation is not impeded by surface boundaries and $C$ is even smaller than the $C$ value of 0.16 Oe for bulk single crystal YIG.

Recall that the data for the normally magnetized (110) films were analyzed with $H_A$ set to zero. If one uses Eq. (4.8) with $4\pi M_s$ = 1610 G and $H_A$ = −28.5 Oe to determine the minimum of $\Delta H_k$ then this value will be 0.21 Oe. If one compares this value with the minimum data for the in-plane magnetized film it will become clear $\Delta H_k$ in YIG films is independent on the direction of the $\theta_k$ = 90° spin waves with respect to the crystallographic axes. The origin of the dependence of $\Delta H_k$ on $\theta_k$ has not been clarified in the literature (W. Haubenreisser *et al.* [1976]).

The results and the analysis of the $h_{crit}$ data in this chapter showed the influence of the small magnetocrystalline cubic anisotropy and thin film geometry on parallel

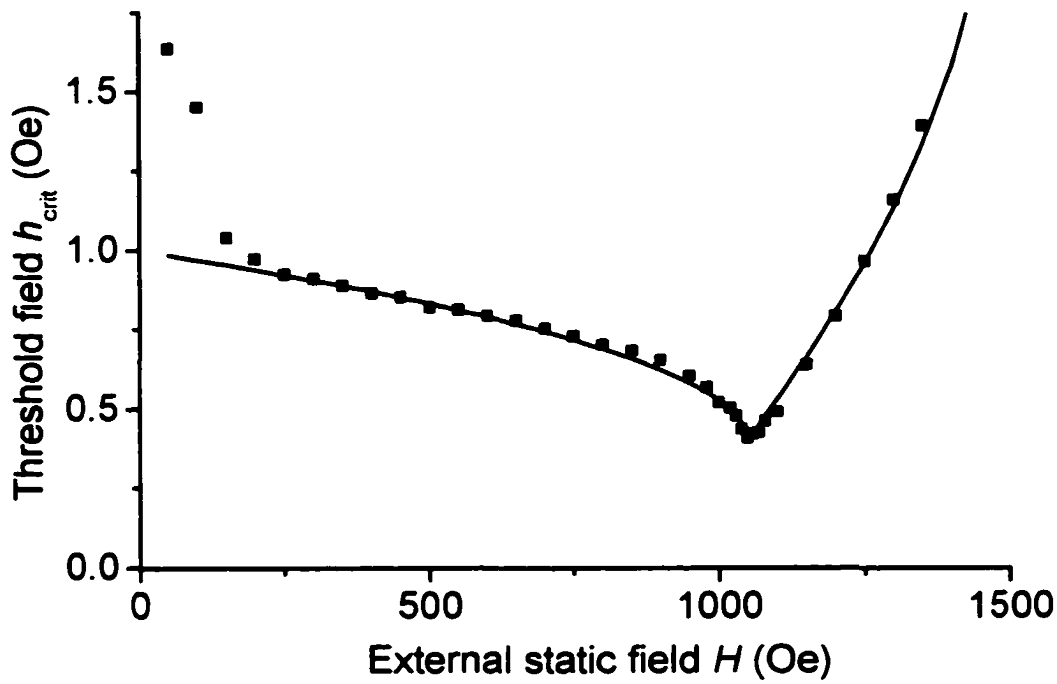


Figure 4.6. Spin wave instability threshold $h_{crit}$ as a function of the external static magnetic field $H$ for parallel pumping at 9 GHz in the 3 mm LPE YIG disk. The static field is applied in-plane along the [100] axis. The closed squares indicate experiment, the solid line indicates theoretical fit to the data.

pumping spin wave instability processes in single crystal (110) LPE YIG thin films. The important results are (1) the influence of surface boundaries on $h_{crit}$ and (2) the evidence that $\Delta H_k$ in the ferromagnet with small anisotropy is independent of the orientation of the spin wave propagation direction with respect to crystallographic axes. This information is important for the investigation of the spin wave instability processes in hexagonal ferrites with large easy-plane anisotropy, which is a topic of Chapter 6. The next chapter will consider the spin wave instability processes in bulk hipped polycrystalline YIG where grain boundaries increase $\Delta H_k$ in a similar way as surface boundaries in thin single crystal films.

# CHAPTER 5

# HIGH POWER MICROWAVE PROPERTIES OF POLYCRYSTALLINE HIPPED YIG

This chapter presents the results of the spin wave instability investigation in polycrystalline hipped YIG. The hipped YIG is assumed to have a very low microwave loss due to the absence of porosity and high material purity. The investigation of the microwave properties included FMR linewidth measurements at different frequencies and spin wave instability threshold measurements at 9 and 16.7 GHz.

The FMR linewidth data show that the dipole narrowed anisotropy line broadening theory of two magnon scattering (Schlömann [1958]) describe the data very well and the uniform precession of magnetization with $k \approx 0$ is truly uniform through the entire sample. The perpendicular pumping data at 9 GHz also support this statement. The parallel pumping data show that spin wave excitation for parallel pumping occurs independently in each individual grain. In polycrystalline ferrite samples, $\Delta H_k$ depends on a grain size and this dependence dominates over intrinsic losses (Patton [1970]). One of the models often evoked to explain such dependence is a transit time model. The application of the transit time model demonstrated that the intrinsic spin wave linewidth $\Delta H_k$ in hipped polycrystalline YIG bears some similarity to $\Delta H_k$ for single crystal YIG and depends on the grain size.

Section 5.1 shows the results of the FMR linewidth measurements. Section 5.2 presents the results of the parallel and perpendicular pumping $h_{crit}$ measurements at 9 GHz and the parallel pumping $h_{crit}$ measurements at 16.7 GHz. Section 5.3 discusses the results of the previous sections and presents a spin wave linewidth analysis based on the transit time model.

## 5.1. Ferromagnetic Resonance

Hipped polycrystalline YIG is a special ferrite material due to its extremely high density. This is an ideal situation to study two magnon scattering processes (Patton [1975]). The two magnon processes are forbidden in an ideal crystal by the momentum conservation law. They are allowed in a crystal with nonuniformities and their probabilities can be large. Such processes can be referred to as the scattering of magnons by nonuniformities. When the initial mode is the uniform mode, the treatment of these processes uses the low $k$ scattering approximation. In polycrystalline materials, the FMR linewidth $\Delta H_0$ is determined by two magnon processes and was calculated by Schlömann [1958]. The goal was to compare the predicted $\Delta H_0$ with the data. The measurements were done for hipped YIG which does not have a porosity contribution to $\Delta H_0$ due to high material density.

Ferromagnetic resonance fields and linewidths were measured for the hipped YIG samples listed in Table 3.2 for the in-plane and out of plane field geometry. All samples were measured at 9.5 GHz. The FMR linewidth in the sphere was also measured as a function of frequency. Standard shorted waveguide techniques were used (Green and Kohane [1964]). The sphere was positioned in the center of the waveguide at the distance $\lambda/2$ from the shorted end for measurements at particular frequency. The magnet was rotated to decrease the angle between applied static field $H$ and microwave field $\boldsymbol{h}$ so that overcoupling between the sphere and the waveguide was avoided.

Ferromagnetic resonance response was measured at room temperature in the X-band with a shorted waveguide method. Table 5.1 shows the sample shape, FMR field

Table 5.1. Summary of FMR field position, linewidth, and gyromagnetic ratio for the hipped YIG sphere and disk at 9.53 GHz.

| Sample shape | FMR field $H_0$ (kOe) | FMR Linewidth $\Delta H_0$ (Oe) | Gyromagnetic ratio $\lvert\gamma\rvert/2\pi$ (MHz/Oe) |
|---|---|---|---|
| Sphere | 3.47 | 13 | 2.75 |
| Disc (in-plane) | 2.89 | 22 | 2.77 |
| Disc (out of plane) | 4.64 | 14 | 2.77 |

$H_0$, FMR linewidth $\Delta H_0$, and the absolute value of the gyromagnetic ratio $|\gamma|/2\pi$ for the hipped YIG sphere and disk at 9.53 GHz. The reported FMR linewidth $\Delta H_0$ corresponds to the difference between the values of the static field for which the imaginary part of the susceptibility equals half its maximum value. The $\Delta H_0$ measurements for the in-plane magnetized disk were performed with microwave field in and out of the disk plane and the $\Delta H_0$ values were identical.

The linewidth of the sphere is 13 Oe. This is remarkably low considering the poor surface polish observed under the microscope. In a perfectly dense material, there should be no contribution to $\Delta H_0$ from porosity (Winkler [1981]). If the material is polycrystalline, the linewidth will be dominated by anisotropy broadening. According to Schlömann's theory [1958], the dipole narrowed anisotropy line broadening of the sphere may be written as

$$\Delta H_0 = 2.07\left((2H_A)^2/4\pi M_s\right)G(\omega/\omega_M), \tag{5.1}$$

where

$$G(x) = \frac{x^2 - x\;3 + 19\;360}{\sqrt{(x-1\;3)^3(x-2\;3)}}. \tag{5.2}$$

The $G(x)$ function describes the density of the low $k$ spin wave states that participate in two magnon scattering. For the YIG sphere, with the parameters $4\pi M_s$ = 1825 G, $|\gamma|/2\pi$ = 2.8 GHz/kOe, and $H_A$ = −44 Oe, Eqs. (5.1) and (5.2) yield $\Delta H_0$ = 12.9 Oe, which is in excellent agreement with the measured value.

The linewidth of the disc is similar to that of the sphere for the out of plane external static field. For the in-plane static field, it is almost twice this value. The higher value for in-plane $H$ is consistent with two magnon scattering considerations. For the in-plane

$H$, there is a higher density of spin wave modes which are degenerate with the uniform mode as compared to the out of plane $H$. The distribution of the internal field due to nonuniform demagnetizing fields is also higher for the in-plane configuration. As one can see from Table 3.2, the disk was thick and the ellipsoid approximation was poor. For the in-plane magnetized disk, the rotational symmetry was absent which increased the field inhomogeneity. These considerations lead to larger two magnon linewidth broadening. The effects of the orientation of the static field and field inhomogeneity will also be considered in the next section, where parallel pumping data are presented.

The dipole narrowed anisotropy line broadening model can be further tested if $\Delta H_0$ is measured as a function of frequency. Figure 5.1 shows the FMR linewidth $\Delta H_0$ as a function of the frequency $f$ from 9.5 to 18 GHz for the hipped YIG sphere. The squares indicate the experimental data. The solid line indicates the dipole narrowed anisotropy line broadening calculation of Eqs. (5.1) and (5.2). The linewidth measurement error was on the order of 10% which explains the scatter in the data. One can see that there is a good agreement between experiment and theory. A similar frequency dependence was observed for frequencies below 10 GHz in polycrystalline YIG with the small amount of residual porosity which led to larger $\Delta H_0$ (Röschmann [1975]).

## 5.2. Spin Wave Instability Threshold Measurements

This section presents results on parallel and perpendicular pumping $h_{crit}$ measurements at 9 GHz and parallel pumping $h_{crit}$ measurements at 16.7 GHz. The parallel pumping measurements at 9 GHz were performed on the sphere and the disk for

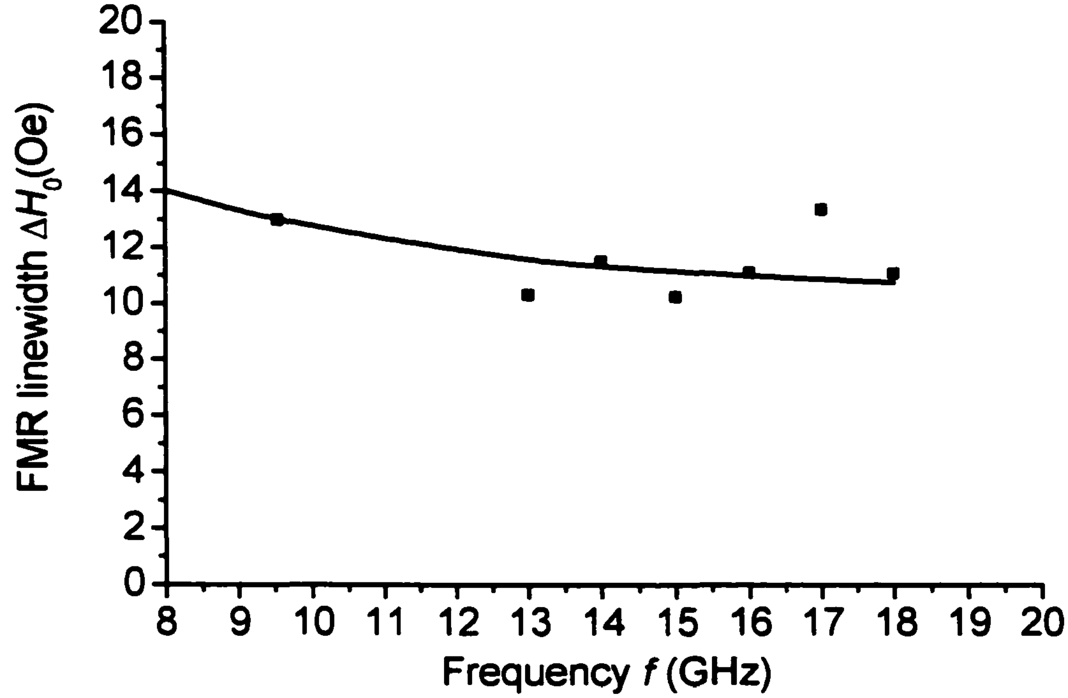


Figure 5.1. FMR linewidth $\Delta H_0$ as a function of the frequency $f$ for the hipped YIG sphere. The closed squares indicate the data. The solid line indicates the dipole narrowed anisotropy line broadening calculation of Eqs. (5.1) and (5.2).

the same configurations as in the previous section. For all $h_{crit}$ measurements, the threshold was determined by the visual method. Figure 5.2 shows the spin wave instability threshold $h_{crit}$ as a function of the external static magnetic field $H$ for parallel pumping at 9 GHz in the hipped YIG sphere and the disk. The closed squares correspond to the sphere, the open circles correspond to the in-plane magnetized disk, and the triangles correspond to the normally magnetized disk.

There are similar features of the butterfly curves for the sphere and the normally magnetized disk to the example data in Fig. 3.7 for the polycrystalline sphere. The different minimum $h_{crit}$ regions originate from the different demagnetizing fields for each configuration. The butterfly curve minimum shows a flat $h_{crit}$ region response which is most pronounced for the sphere. For the sphere, the flat region is in the field interval of 1.45 to 1.6 kOe. For the in-plane magnetized disk, it is in the field interval of 0.85 to 1.34 kOe. For the normally magnetized disk, it is in the field interval of 2.00 to 2.50 kOe. A similar butterfly curve and flat region were shown in Fig. 3.6 for the example data. A discussion of the flat $h_{crit}$ region will be developed shortly.

As discussed in the previous section, the disk was thick and the ellipsoid approximation was not reliable. Figure 5.2 shows that the butterfly curve for the in-plane magnetized disk significantly differs from the other two curves. It supports the idea that the in-plane magnetized disk is not uniformly magnetized because there is no symmetry around $H$. The uniformity of the magnetization is somewhat better for the normally magnetized disk. The sphere is completely uniformly magnetized when $H$ is greater than the demagnetizing field. Therefore, the data for the in-plane magnetized disk will be omitted from the further analysis.

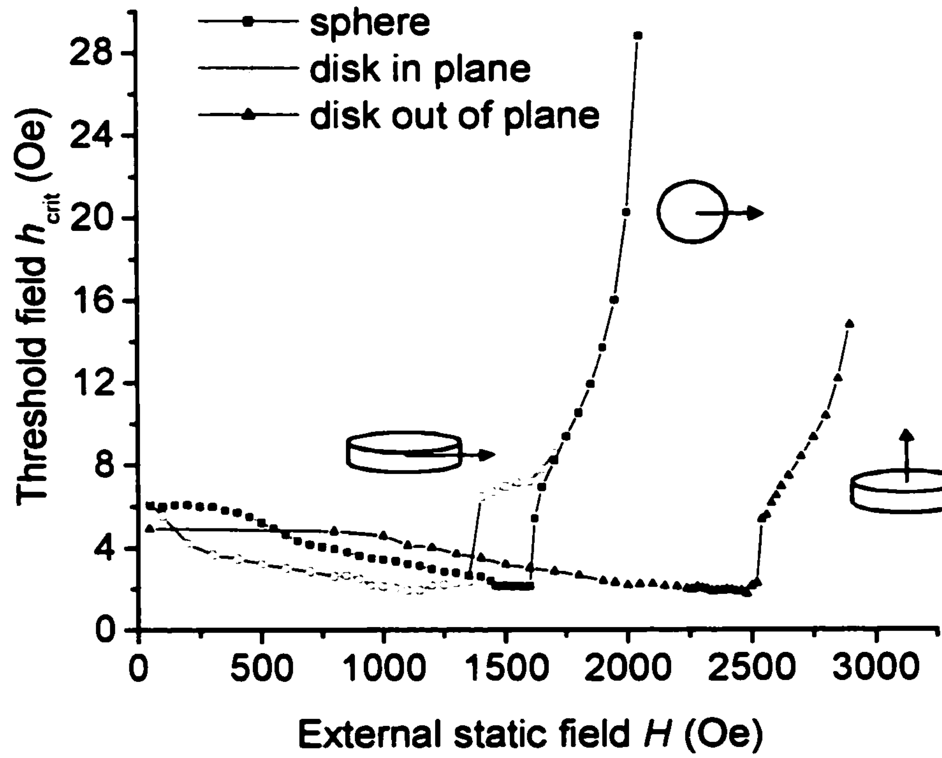


Figure 5.2. Spin wave instability threshold $h_{crit}$ as a function of the external static magnetic field $H$ for parallel pumping at 9 GHz in the hipped YIG sphere and disk. The closed squares correspond to the sphere, the open circles correspond to the in-plane magnetized disk, and the triangles correspond to the normally magnetized disk.

All aspects of the example data analysis apply to the butterfly curve features in Fig. 5.2. Based on the procedure developed in Section 3.4, the data in Fig. 5.2 were analyzed to obtain the spin wave linewidth $\Delta H_k$ as a function of the wave number $k$. The wave number value can be obtained from Eq. (3.10). The $H_c$ value was taken to correspond not to the minimum of $h_{crit}$, but to the left field value of the flat $h_{crit}$ region where $h_{crit}$ starts to consistently increase. Equation (3.4) relates $h_{crit}$ and $\Delta H_k$ for $\theta_k$ = 90°. For this situation, all anisotropy effects are ignored because the material is isotropic.

Figure 5.3 shows the spin wave linewidth parameter $\Delta H_k$ at the half pump frequency of 4.5 GHz as a function of wave number $k$ for $\theta_k$ = 90° spin waves. The symbols which show the data are the same as in Fig. 5.2. The straight solid lines indicate the fit to the linear part of the data from Eq. (3.11). The fit parameters were $\Delta H_{k=0}$ = 1.18 Oe and $B = 2.52\times10^{-6}$ Oe·cm/rad for the sphere. For the disk, the fit gave $\Delta H_{k=0}$ = 1.06 Oe, $B = 2.39\times10^{-6}$ Oe·cm/rad. One can see that the $\Delta H_k$ response is almost identical with the slightly different $\Delta H_{k=0}$ values. The minimum $\Delta H_k$ values were 1.22 Oe for the sphere and 1.25 Oe for the disk. The $\Delta H_k$ increase at $k > 4\times10^5$ rad/cm is related to the presence of domains in the sample at low field.

The inhomogeneous field distribution for the in-plane and normally magnetized disk obstructs the analysis of the $h_{crit}$ data as it is shown in Fig. 5.2. For the sphere, it is possible to perform an extensive $h_{crit}$ investigation and a data analysis. Therefore, the further data and analysis will be given for the sphere only.

Consider the $h_{crit}$ response on the right side of the butterfly curve in Fig. 5.2. It can be fitted by the formula $\Delta H_k = 3.5+2.5\cos^2\theta_k$ (Oe). Note that the value of 3.5 Oe is much greater than $\Delta H_{k=0}$ for the sphere. This formula describes the jump in $h_{crit}$. This

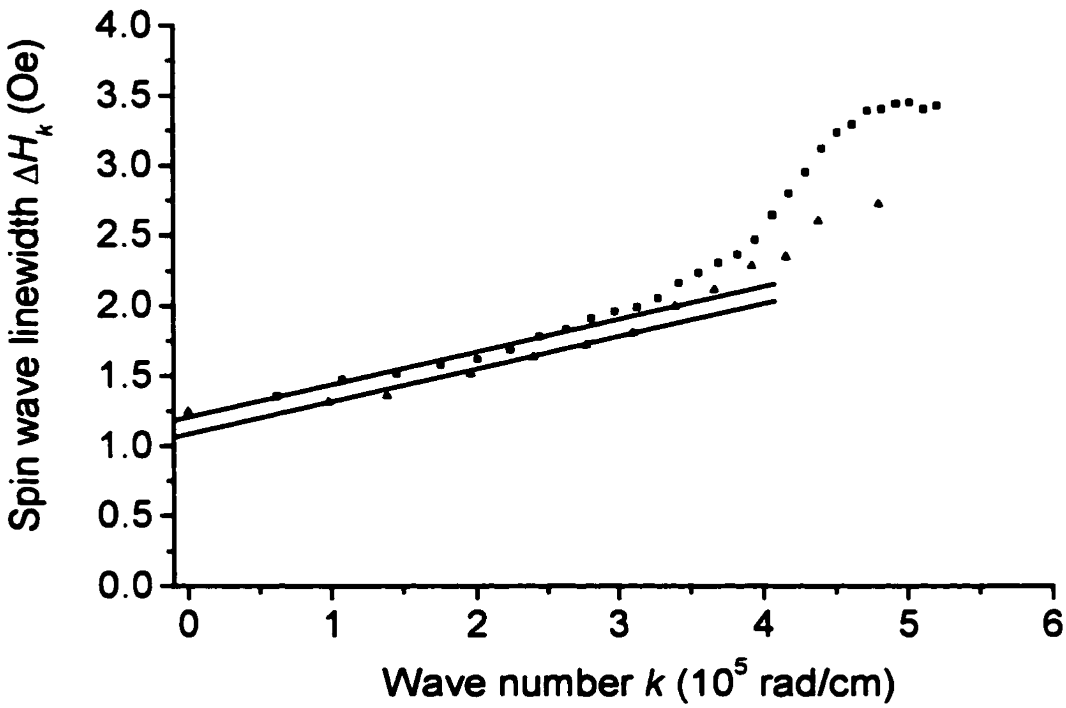


Figure 5.3. Spin wave linewidth $\Delta H_k$ as a function of spin wave wave number $k$ at 4.5 GHz in the hipped YIG. The squares correspond to the sphere, the triangles correspond to the normally magnetized disk. The straight solid lines indicate the linear fit to the data.

jump is present for all three butterfly curves. This behavior will be considered later in the discussion section. Consider the flat $h_{crit}$ region in Fig. 5.2 which is well pronounced for the sphere and broadened for the in-plane and normally magnetized disk. In the case of the disk the broadening comes from the demagnetizing effects. The origin of this flat region will be discussed only for the sphere.

Figure 5.4 shows a selected part of the butterfly curve from Fig. 5.2 for parallel pumping at 9 GHz in the hipped YIG sphere. The vertical lines correspond to the calculated $H_c$ positions for $H$ oriented along one of the crystallographic axes as if parallel pumping were done in single crystal YIG as discussed in Section 4.2. These values were calculated from Eqs. (4.2) and (4.3) with the parameters specified above for hipped YIG. The $H_c$ value for $H$ along the easy [111] axis is 1.48 kOe. The $H_c$ value for $H$ along the hard [100] axis is 1.63 kOe. The difference between these values is equal to the width of the flat region. The 30 Oe offset is attributed to the deviation of the sample shape from an ideal sphere.

The existence of the flat region is indicative that the spin wave excitation occurs independently in each grain. The overall minimum threshold corresponds to the specific grain with the specific minimum threshold. The number of the grains is large and their orientation includes a large number of possible directions. Therefore, the butterfly curve becomes a minimum of the large number of the butterfly curves for all grains. This implies that internal magnetic states of the different grains are different and these states depend on the grain orientation.

Along with the parallel pumping measurements, the spin wave instability processes in the hipped YIG sphere were investigated by the perpendicular pumping technique,

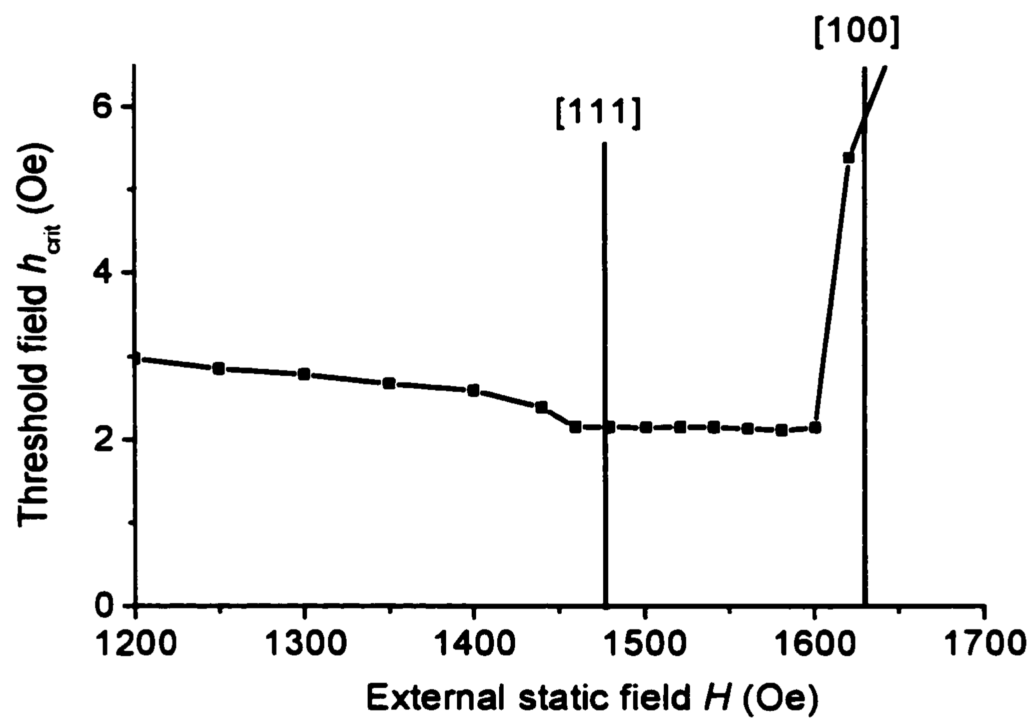


Figure 5.4. Spin wave instability threshold $h_{crit}$ as a function of the external static magnetic field $H$ for parallel pumping at 9 GHz in the hipped YIG sphere. The vertical lines correspond to the calculated $H_c$ positions for $H$ oriented along the [111] or [100] crystallographic axes, as indicated in the graph.

when the microwave field $h$ is applied perpendicular to $H$. As a result of this pumping configuration, the microwave field $h$ drives the uniform mode $a_0$ and the energy is transferred to spin waves through this mode (Suhl [1957]). This technique is also called subsidiary absorption. In the parallel pumping configuration, spin waves are excited directly by $h$.

Figure 5.5 shows the spin wave instability threshold $h_{crit}$ as a function of the external static magnetic field $H$ for perpendicular pumping at 9 GHz in the hipped YIG sphere. The squares correspond to the experiment. The solid line corresponds to the $h_{crit}$ calculation based on a constant $\Delta H_k$ of 1.8 Oe. The entire calculated curve was shifted to the left by 40 Oe to provide a better match. The solid curve starts from the value of the demagnetizing field which is about 600 Oe. Similar data were obtained by Patton *et al.* [1969].

The $h_{crit}$ calculation was based on the theory developed in Chapter 2. The formula for a specific threshold $h_c$ follows from Eqs. (2.65)-(2.68) and the linear polarization of the microwave field $h$. The expression for the spin wave instability threshold $h_{crit}$ in the case of perpendicular pumping in an isotropic ferrite sphere may be written as

$$h_{crit} = \min_{\theta_k}\left\{\frac{2\omega\,\Delta H_k(\omega^2 - (|\gamma|H)^2)}{\omega_M \sin 2\theta_k\left[\omega^2 + (|\gamma|H)\left(\sqrt{\omega^2 + (\omega_M \sin^2\theta_k)^2} - \omega_M \sin^2\theta_k\right)\right]}\right\}. \quad (5.3)$$

This expression was already minimized over $\varphi_k$. The obtained $\varphi_k$ value is the same as the azimuthal angle of the linear polarized microwave field $h$. One can see that it is impossible to minimize Eq. (5.3) analytically. The minimization over $\theta_k$ was performed numerically with the material parameters specified above for hipped YIG. The details of such numerical minimization were discussed in Section 2.4.

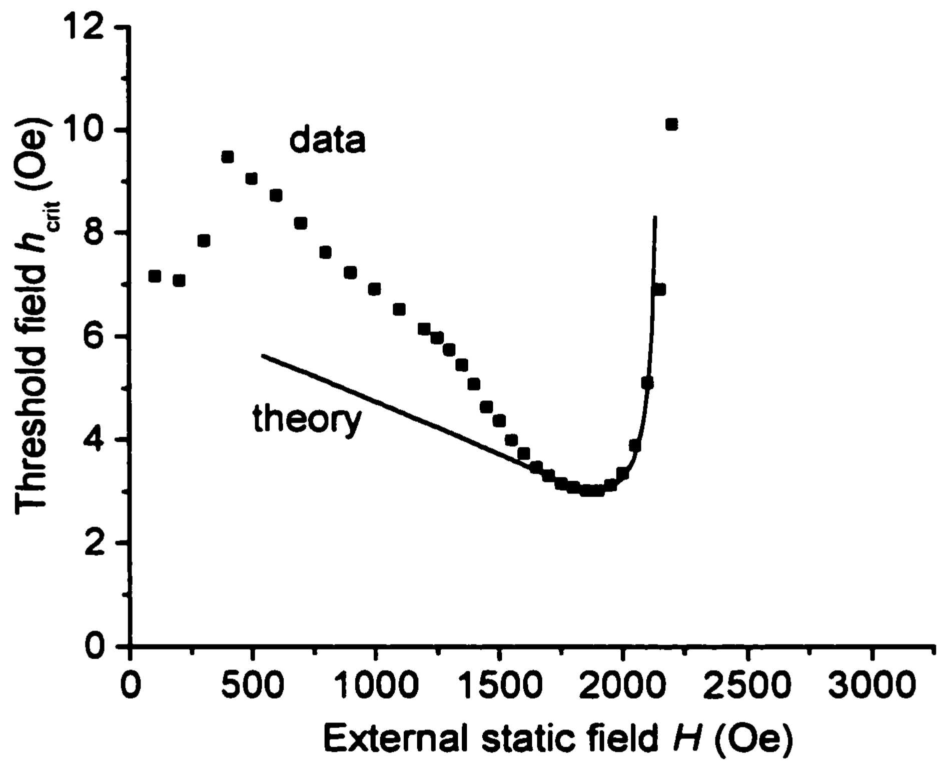


Figure 5.5. Spin wave instability threshold $h_{crit}$ as a function of the external static magnetic field $H$ for perpendicular pumping at 9 GHz in the hipped YIG sphere. The closed squares correspond to the data, the solid line corresponds to the calculated $h_{crit}$ based on a constant $\Delta H_k$ of 1.8 Oe.

The solid line in Fig. 5.5 represents the result of such minimization. In the minimum of $h_{crit}$, the angle $\theta_k$ is 35°. As $H$ decreases, $\theta_k$ slowly approaches 45°. As $H$ increases, $\theta_k$ decreases. One can see that the theoretical fit agrees well with the data for low $k$. The corresponding spin wave linewidth is 1.8 Oe. As $k$ increases, the spin wave linewidth increases too, and the experimental $h_{crit}$ is larger than the theoretical fit. The $\Delta H_k$ vs. $k$ dependence is not linear and requires further assumptions. There is a distinct kink in the data at $H$ = 1.2 kOe. This effect may be due to the kink effect for perpendicular pumping (Patton and Jantz [1979] and Wiese *et al.* [1995]). In order to provide a theoretical fit in this case, it is necessary to assume and model the $\Delta H_k$ dependence on $k$ and $\theta_k$ when one performs the minimization of Eq. (5.3). Consider the 40 Oe shift in $H$ which is required to fit the data. As shown in Fig. 5.4 for parallel pumping, the theoretical position of the flat region is also shifted by about 30 Oe towards larger $H$. The assumption is that the non-ideal shape of the spherical sample causes this discrepancy.

The region of the constant $\Delta H_k$ of 1.8 Oe, where the data matches theory, corresponds to the $\theta_k$ interval of 19° to 43°. In the parallel pumping data, these angles yield much larger $\Delta H_k$. Also, there is no flat region in the perpendicular pumping data. This can be explained by the fact that energy is transferred to the spin waves from the uniform mode. This uniform mode response also determines the FMR linewidth. Therefore, the dipole-dipole narrowing works for the uniform mode in the case of perpendicular pumping too.

The spin wave instability processes in the hipped YIG sphere were also investigated by a parallel pumping technique at 16.7 GHz. Figure 5.6 shows the spin wave instability threshold $h_{crit}$ as a function of the external static magnetic field $H$ for

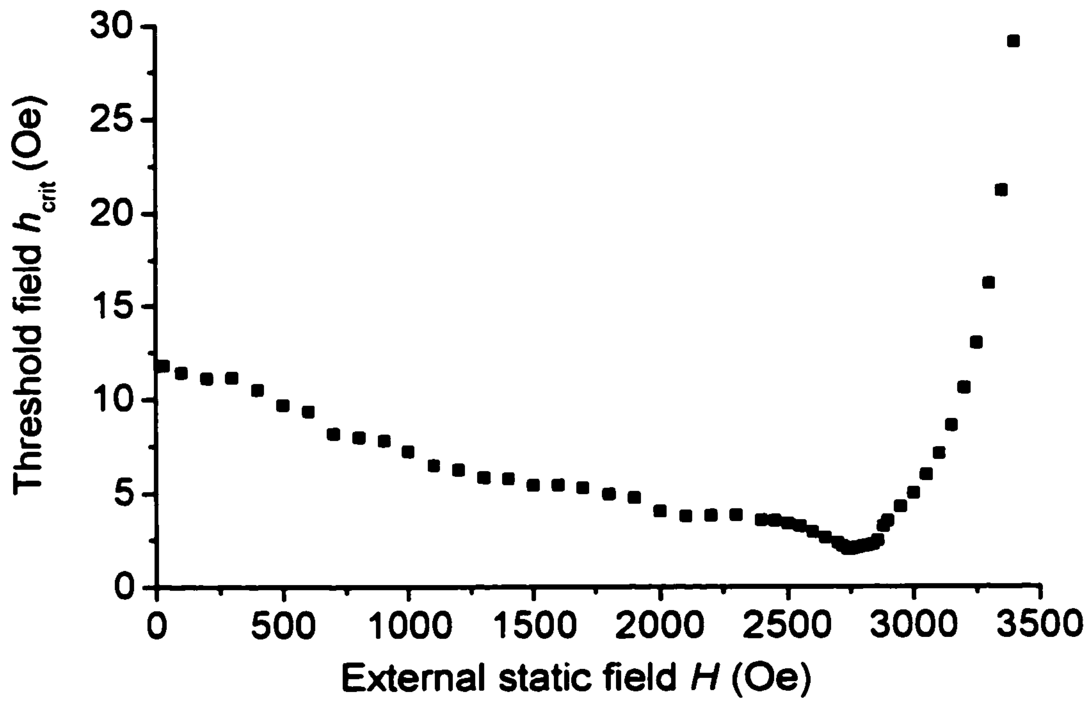


Figure 5.6. Spin wave instability threshold $h_{crit}$ as a function of the external static magnetic field $H$ for parallel pumping at 16.7 GHz in the hipped YIG sphere.

parallel pumping at 16.7 GHz in the hipped YIG sphere. One can see that there is a distinct $h_{crit}$ minimum. The data in Fig. 5.6 were analyzed in the same way as the $h_{crit}$ data at 9 GHz for the sphere in Fig. 5.2. The $H_c$ value was taken to correspond to the minimum of $h_{crit}$. The experimental $H_c$ was 2.74 kOe, the theoretical value from Eq. (3.8) was 2.82 kOe. If one takes into account the 30 Oe offset due to the deviation of the sample shape from an ideal sphere, as in Fig. 5.4, the experimental $H_c$ value corresponds to $H$ along the [1 1 1] direction, which is an easy axis.

Figure 5.7 shows the spin wave linewidth parameter $\Delta H_k$ at the half pump frequency of 8.35 GHz as a function of wave number $k$ for $\theta_k$ = 90° spin waves. The closed squares show the data. The straight solid line indicates a fit to the linear part of the data from Eq. (3.11). The fit parameters were $\Delta H_{k=0}$ = 0.47 Oe and $B$ = $2.54\times10^{-6}$ Oe·cm/rad. The minimum $\Delta H_k$ value was 0.61 Oe. The $\Delta H_k$ increase at large $k$ values is related to the presence of domains in the sample. The slight dip at $k \approx 3.5\times10^{5}$ rad/cm does not have a reasonable explanation. The $h_{crit}$ response on the right side of the butterfly curve in Fig. 5.6 can be described by the fit formula $\Delta H_k = 0.7+2.2\cos^2\theta_k$ (Oe). Note that the value of 0.7 Oe is close to $\Delta H_{k=0}$, opposite to the 9 GHz parallel pumping data.

### 5.3. Transit Time Spin Wave Linewidth in Polycrystalline YIG

The data in the previous section showed that spin wave excitation for parallel pumping occurs independently in each individual grain. Another feature is an unusual $\Delta H_k$ decrease when frequency increases from 9 GHz to 16.7 GHz. This decrease

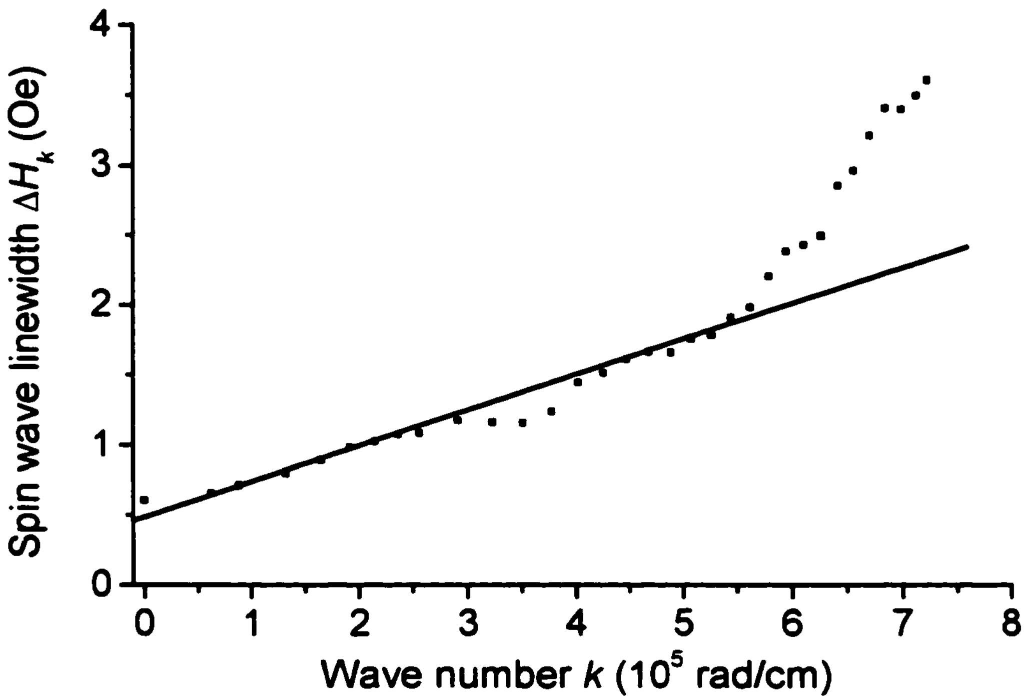


Figure 5.7. Spin wave linewidth $\Delta H_k$ as a function of spin wave wave number $k$ at 8.35 GHz in the hipped YIG sphere. The closed squares correspond to the data. The straight solid line indicates the linear fit to the data.

contradicts the linear frequency dependence of $\Delta H_k$ observed in single crystal YIG. In polycrystalline ferrite samples there is a dependence of $\Delta H_k$ on a grain size which dominates over intrinsic losses (Patton [1970]). One of the models often evoked to explain such dependence is a transit time model. In this model, a spin wave propagation lifetime is determined by the grain size and group velocity. It is important for this model that grains act independently, which one can clearly see from Fig. 5.4. This effect does not appear to be important for FMR linewidth and perpendicular pumping.

The FMR linewidth data show that the dipole narrowed anisotropy line broadening theory of two magnon scattering (Schlömann [1958]) describes the data very well and the uniform precession of magnetization with $k \approx 0$ is truly uniform through the entire sample. The perpendicular pumping data at 9 GHz also support this statement. There are no indications, opposite to the case of parallel pumping, that anisotropy affects the $h_{crit}$ response. The microwave field drives the uniform mode and the uniform mode excites spin waves.

However, in the case of parallel pumping at 9 GHz the spin wave excitation occurs in each grain individually. This causes the appearance of the flat $h_{crit}$ region. The static field position of this flat $h_{crit}$ region agrees well with the independent grain excitation model. For small wave numbers, the overall minimum threshold corresponds to the specific grain with the specific minimum threshold. For parallel pumping at 16.7 GHz, the flat $h_{crit}$ region still exists at the predicted position but is distorted. In this case, the pronounced minimum $h_{crit}$ exists at the $H_c$ value which corresponds to $H$ along the [111] easy direction. The origin of such behavior is yet unknown. One can conclude that in the case of the parallel pumping, when the uniform mode is not involved, the dipole narrowing does not work and does not affect the exchange spin waves. These spin waves are excited independently in each grain.

Consider now the spin wave linewidth response. The data for perpendicular pumping at 9 GHz yield the constant $\Delta H_k$ value of 1.8 Oe for small $k$. This value is significantly larger than minimum $\Delta H_k$ for parallel pumping in both sphere and disk. This difference is related to the $\Delta H_k$ increase when $\theta_k$ decreases, which was found for parallel pumping. The response for small $k$ varies significantly with $\theta_k$ and has not been clarified even for single crystal YIG. Therefore, the analysis will focus only on spin waves with non-zero $k$ and $\theta_k = 90°$. These spin waves are excited by parallel pumping at $H<H_c$.

The $\Delta H_k$ response for spin waves with $\theta_k = 90°$ is described by Eq. (3.11). The parameters in this equation were determined in the previous sections. Note that the $\Delta H_k$ vs. $k$ dependence is similar for the sphere and the disk at 9 GHz. This is not surprising because these samples were fabricated from the same material. The spin wave linewidth is a measure of internal microwave magnetic properties and is not sensitive to the sample shape or surface quality (Sparks [1964]).

Consider the $\Delta H_k$ response for the sphere at 9 GHz. The $\Delta H_{k=0}$ value of 1.18 Oe is much larger than in single crystal YIG, although grains are supposed to have single crystal structure. This large $\Delta H_{k=0}$ can be analyzed based on a transit time model (Vrehen *et al.* [1969] and Patton [1970]). In this model, the lifetime of the excited spin wave is limited by the transit time for the spin wave mode across an individual grain,

$$\tau_k = d_0 / | v_g |, \tag{5.4}$$

where $d_0$ is the average grain size and $v_g$ is the spin wave group velocity. The spin wave linewidth is inversely proportional to the grain size. According to Eq. (2.64), the transit time linewidth $\Delta H_t$ may be written as

$$\Delta H_t = 2/|\gamma|\tau_k = 2|v_g|/(|\gamma|d_0). \tag{5.5}$$

The expression for the group velocity follows from Eq. (3.7) and is given by

$$v_g = \frac{\partial \omega_k}{\partial k} = \frac{2|\gamma|Dk}{\omega_k}\left(\omega_H + |\gamma|Dk^2 + \frac{1}{2}\omega_M \sin^2\theta_k\right). \tag{5.6}$$

Note that Eq. (5.6) predicts the linear $\Delta H_k$ vs. $k$ dependence since the expression in brackets stays constant as $H$ decreases below $H_c$ and $k$ increases.

The calculations of the grain size based on the linear $\Delta H_k$ vs. $k$ dependence and the value of the $B$ parameter yielded an unrealistic grain size of 80 μm for both 9 and 16.7 GHz data. The reason for such discrepancy is that $B$ for hipped YIG is only 2.5 times larger than $B$ for single crystal YIG films discussed in Chapter 4. Therefore, the linear $\Delta H_k$ increase may be determined by the contribution of the intrinsic three magnon processes as in single crystal YIG.

As discussed above, the excited spin waves have a specific minimum nonzero wave number $k_{min}$ which corresponds to minimum $\Delta H_k$. The first data point in Fig. 5.3 corresponds to a $k_{min}$ value of $6\times10^4$ cm$^{-1}$ and $\Delta H_k$ of 1.25 Oe. From Eq. (5.5) with $\Delta H_k$ = 1.25 Oe and $v_g$ given by Eq. (5.6) one obtains the average grain size $d_0$ = 21 μm, a typical grain size for polycrystalline YIG. A transit time analysis for the 16.7 GHz data in Fig. 5.7 with $k_{min} = 5\times10^4$ cm$^{-1}$, $\Delta H_k$ = 0.61 yields $d_0$ = 21 μm, consistent with the results for the 9 GHz data in Fig. 5.3. Note that in this case the minimum possible $k = \pi/d_0$ is much smaller than $k_{min}$. Vrehen *et al.* [1969] argued that $k_{min}$ is of the order of $2\pi/d_0$. This assumption would yield an unrealistic grain size of 2 μm. It is important to note that the grain size $d_0$ of 21 μm calculated from the transit time model is larger than the average grain size of 8 μm. The general yet unresolved question is how to determine the minimum $k$ value of spin waves which are excited in the parallel pumping experiment. This question will be discussed in Chapter 7.

The agreement of the transit time model with the data between 9 GHz and 16.7 GHz data is good. The decrease of the minimum $\Delta H_k$ with increasing frequency from 9 to 16.7 GHz agrees with the transit time model too. Note that the minimum $\Delta H_k$ value of 0.61 Oe is similar to the intrinsic spin wave losses. Recall that in Chapter 4 the minimum $\Delta H_k$ for single crystal YIG was about 0.2 Oe for 9 GHz parallel pumping data. If one assumes a linear $\Delta H_k$ vs. frequency dependence, the corresponding minimum $\Delta H_k$ value for 16 GHz parallel pumping data will be 0.4 Oe, which is close to $\Delta H_k$ of 0.61 Oe for hipped YIG. Therefore, in order to find the truly intrinsic minimum $\Delta H_k$ in hipped YIG, the parallel pumping experiment should be performed at a higher frequency, e.g. 36 GHz. It is also important to find the minimum wave number $k_{\min}$ which corresponds to minimum $\Delta H_k$. These topics will be discussed in Chapter 7.

# CHAPTER 6

# HIGH POWER MICROWAVE PROPERTIES OF SINGLE CRYSTAL ZN-Y HEXAGONAL FERRITE

This chapter presents the results of the spin wave instability investigation in easy plane Zn-Y hexagonal ferrite plates with large magnetocrystalline anisotropy. Anisotropic ferrite plates and slabs are important for microwave applications. An extensive spin wave instability theory for anisotropic ferrites was developed in Chapter 2. The last two chapters presented high power microwave properties of ferrites with small anisotropy, such as single crystal YIG and isotropic dense polycrystalline hipped YIG. The purpose of this chapter is to look at high power microwave properties of highly anisotropic ferrites such as hexagonal Zn-Y ferrite materials with planar anisotropy. The spin wave instability thresholds and critical modes expected for this situation were calculated in Chapter 2. The experimental results for parallel pumping at 9 and 16.7 GHz in in-plane magnetized Zn-Y plates will be presented first and the results for more complicated pumping configurations will be presented later.

Recent high power measurements on single crystal *c*-plane disks of easy plane Zn-Y hexagonal ferrite at 9 GHz gave parallel pump and subsidiary absorption $\Delta H_k$ values which were a factor of two or more greater than the low power FMR linewidth $\Delta H_0$ and the high power resonance saturation $\Delta H_k$ (Cox *et al.* [2001]). However, higher frequency parallel pumping data at 16.6 GHz (Green and Healy [1963]) and at 36 GHz (Gurevich *et al.* [1999]) for Zn-Y platelets and spheres give spin wave linewidths which are consistent with the FMR results. One objective of the parallel pumping work was to elucidate this problem. It is possible to explain this discrepancy in $\Delta H_k$ by size effects at 9 GHz, related to the transit time model which played an important role for polycrystalline YIG in Chapter 5. At 16.7 GHz, there were no considerable size effects and experimental butterfly curves were in a reasonable agreement with the developments of Chapter 2. The simple theoretical analysis will be presented only for the parallel pumping data.

The more complicated pumping situations include in-plane oblique pumping, where $H$ is rotated in the plate plane, and out of plane oblique pumping, where $H$ is rotated in the plane perpendicular to the plate. The full power of the general spin wave instability theory of Chapter 2 was applied to the 16.7 GHz oblique pumping data. The theoretical model was consistent with the data. As a result of the data analysis, a "magnetic stress" effect was found. The results of the analysis show that $\Delta H_k$ is independent of the spin wave propagation direction and increases with an increase in the magnetic stress caused by the static magnetization deviation from the easy plane.

Section 6.1 describes the sample geometry and the results of the FMR characterization. Section 6.2 establishes working equations for the parallel pumping data analysis. In this section, the results of the parallel pumping measurements at 9 and 16.7 GHz are presented and the sample size effect is discussed. Sections 6.3 and 6.4 present the in-plane and out of plane 16.7 GHz oblique pumping $h_{crit}$ data and analysis, respectively.

## 6.1. Sample Geometry and FMR Characterization

The focus of this section is to introduce the sample geometry, establish a coordinate frame for the data analysis of the next sections, and obtain working parameters for Zn(Mn)-Y and Zn-Y hexagonal ferrite samples from the FMR measurements. The material properties and static magnetic characteristics of easy-plane hexagonal ferrite Zn(Mn)-Y and Zn-Y samples were discussed in Section 3.1. All samples were made of these two materials in the form of plates with the hexagonal *c* plane in the plane of the plate. The samples for the measurements consisted of thin rectangular and circular plates fabricated from bulk single crystal Zn(Mn)-Y and Zn-Y. The main focus of high power measurements is on the Mn-substituted Zn(Mn)-Y. The data for Zn-Y are used as a reference point.

It is necessary to introduce a coordinate frame in order to define demagnetizing factors, which are important parameters in the spin wave instability analysis, and establish the geometry of the problem following the formalism of Chapter 2. For the FMR analysis, parallel pumping, and in-plane oblique pumping, this coordinate frame will be a laboratory and precession frame at the same time since $\mathbf{H}$ is applied in the plane of the plate. In this case, the easy plane coincides with the plate plane and $\mathbf{M}_s$ is parallel to $\mathbf{H}$. The geometry for out of plane oblique pumping was established in Section 2.4.

The geometry of the problem for the FMR analysis is shown in Fig. 6.1. The plate is in the $y$-$z$ plane of the $(x, y, z)$ coordinate frame. The external static field $\mathbf{H}$ is applied along the $z$-axis. The linearly polarized microwave field $\mathbf{h}(t)$ is applied along the $y$-axis. This microwave field configuration was used for the FMR measurements. The $(x, y, z)$

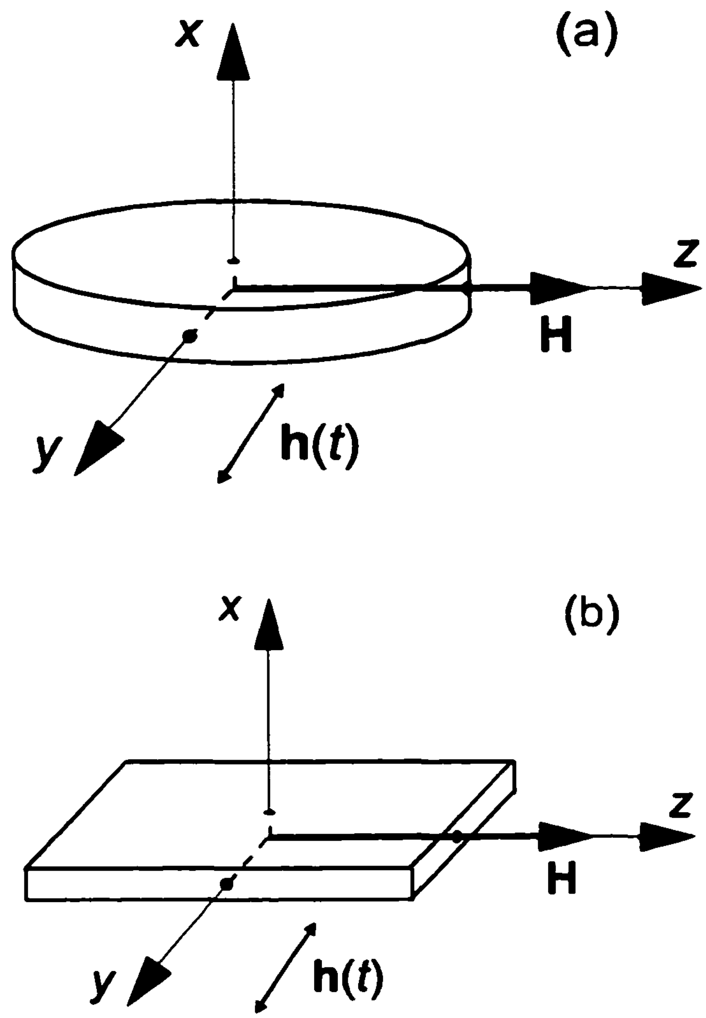


Figure 6.1. Geometry for the easy plane plate FMR analysis. The disk (a) or the slab (b) is in the $y$-$z$ plane of the ($x$, $y$, $z$) coordinate frame. The external static field $\mathbf{H}$ is along $z$. The linearly polarized microwave field $\mathbf{h}(t)$ is along $y$.

coordinate frame in Fig. 6.1 serves to define the demagnetizing factors $N_x$, $N_y$, and $N_z$. For a disk, $N_y$ equals $N_z$ and demagnetizing factors can be found from Eq. (4.4). For a thin slab, Eq. (4.4) is not directly applicable and demagnetizing factors were found from Appendix B in Gurevich and Melkov [1996]. Note that the condition $N_x+N_y+N_z = 1$ should hold for any ellipsoidal sample shape.

Table 6.1 shows geometrical properties of the samples from Table 3.3, which include thickness $t$, in-plane dimensions (diameter $d$ for disks, length $a$ and width $b$ for slabs), and calculated demagnetizing factors $N_x$, $N_y$, and $N_z$. The demagnetizing factors will be important parameters for the FMR and $h_{crit}$ data analysis.

The geometry of the problem for parallel and in-plane oblique pumping in a disk is shown in Fig. 6.2. The disk is in the $y$-$z$ plane of the ($x$, $y$, $z$) coordinate frame. The external static field $\mathbf{H}$ is applied along the $z$-axis. The linearly polarized microwave field $\mathbf{h}(t)$ is applied in the $y$-$z$ plane at an angle $\theta_h$ relative to $\mathbf{H}$. For parallel pumping, $\theta_h$ is 0 and $\mathbf{h}(t)$ is along $z$. In-plane and out of plane oblique pumping measurements were performed only for disks. The parallel pumping geometry for a slab is the same as in Fig. 6.1(b) with $\mathbf{h}(t)$ along $z$.

As indicated above, FMR half power linewidth measurements were made on most of the samples and at nominal frequencies close to both of the parallel pump frequencies. These data were obtained by a standard shorted waveguide technique at low power (Green and Kohane [1964]). All FMR measurements were made with $H$ in-plane. The purpose of the FMR measurements was to check the anisotropy field parameter value and measure FMR linewidth. The resonance condition for the easy-plane plates with the field $H$ in the plate plane follows from Eqs. (2.37)-(2.40) and may be written as

Table 6.1. Summary of Zn(Mn)-Y and Zn-Y sample properties.

| Sample | Material | Sample shape | Thickness (mm) | In-plane size (mm) | $N_x$ | $N_y$ | $N_z$ |
|---|---|---|---|---|---|---|---|
| S1 | Zn(Mn)-Y | disk | 0.34 | 2.39 | 0.81 | 0.095 | 0.095 |
| S2 | Zn(Mn)-Y | disk | 0.19 | 2.32 | 0.88 | 0.058 | 0.058 |
| S3 | Zn(Mn)-Y | disk | 0.14 | 1.52 | 0.87 | 0.065 | 0.065 |
| S4 | Zn(Mn)-Y | disk | 0.09 | 2.32 | 0.94 | 0.029 | 0.029 |
| S5 | Zn(Mn)-Y | slab | 0.09 | 1.62×0.72 | 0.87 | 0.11 | 0.024 |
| S6 | Zn(Mn)-Y | slab | 0.05 | 1.44×0.64 | 0.90 | 0.08 | 0.016 |
| SP1 | Zn-Y | disk | 0.43 | 2.53 | 0.78 | 0.109 | 0.109 |
| SP2 | Zn-Y | disk | 0.20 | 2.50 | 0.89 | 0.057 | 0.057 |
| SP3 | Zn-Y | disk | 0.13 | 1.81 | 0.90 | 0.052 | 0.052 |

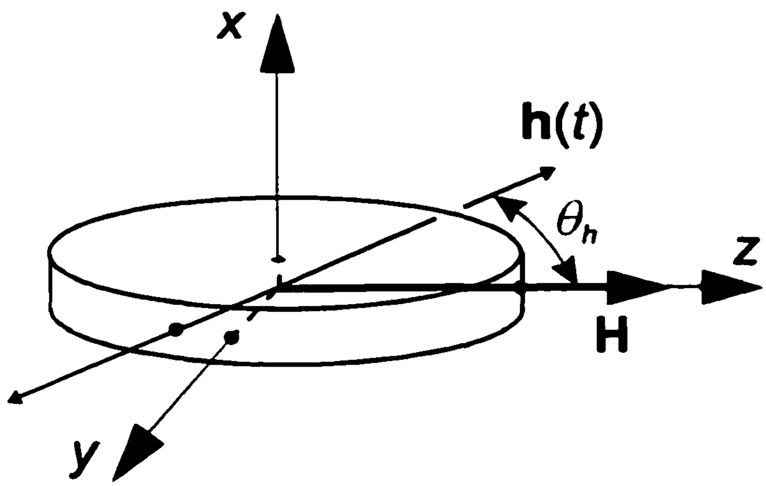


Figure 6.2. Geometry for parallel and in-plane oblique pumping in an easy plane disk. The disk is in the $y$-$z$ plane of the $(x, y, z)$ coordinate frame. The external static field **H** is along $z$. The linearly polarized microwave field $\mathbf{h}(t)$ is in the $y$-$z$ plane at an angle $\theta_h$ relative to **H**. For parallel pumping, $\theta_h$ is 0 and $\mathbf{h}(t)$ is along $z$.

$$\omega_0 / |\gamma| = \sqrt{(H + 4\pi M_s(N_y - N_z))(H - 4\pi M_s(N_x - N_z) + H_A)}. \quad (6.1)$$

Equation (6.1) can be used to check the $H_A$ values which were obtained from the VSM measurements. Measurements of the FMR response at a constant frequency $f_0$ yield an FMR field $H_0$. The values of $4\pi M_s$ were found from the VSM measurements, presented in Section 3.1, and were assumed to be the same for the samples made from the same material. Because of the disagreement in the literature (McKinstry [1991], Truedson [1993], and Hurben [1996]) the value of $|\gamma|/2\pi$ was assumed to be 2.8 GHz/kOe to avoid additional errors. Then one can estimate $H_A$ based on the parameters specified above, the demagnetizing factors in Table 6.1, and Eq. (6.1).

Table 6.2 summarizes the FMR field position $H_0$, FMR linewidth $\Delta H_0$, and calculated anisotropy field $H_A$ for Zn(Mn)-Y and Zn-Y samples at 9.52 and 17.5 GHz frequencies. For an $h_{crit}$ data analysis, only one $H_A$ value will be used for the samples made of the same material. The smaller $N_z$ values correspond to thin samples that resemble an ellipsoid better than thick samples. Therefore, for Zn(Mn)-Y, an $H_A$ value of –9.4 kOe will be used throughout this work. This $H_A$ value is in agreement with Table 6.2 and the VSM data. This value was also cited by Hurben *et al.* [1997]. For Zn-Y, an $H_A$ value of –8.75 kOe will be used throughout this work. This value corresponds to the $H_A$ value for the sample SP3 and also was cited by Truedson [1993].

Consider the FMR linewidth values in Table 6.2. For Zn-Y, $\Delta H_0$ increases as the diameter or frequency increases. This increase is a feature of the eddy current losses and was investigated in detail by Truedson [1993]. These losses are related to conductivity. Note that dc conductivity measurements also showed nonzero conductivity in pure Zn-Y. For Zn(Mn)-Y, $\Delta H_0$ is similar for all samples at 9.52 GHz and increases linearly with

Table 6.2. Summary of FMR field position $H_0$, linewidth $\Delta H_0$, and anisotropy field $H_A$ for Zn(Mn)-Y and Zn-Y samples.

| | FMR frequency 9.52 GHz | | | FMR frequency 17.5 GHz | | |
|---|---|---|---|---|---|---|
| Sample | $H_0$ (Oe) | $\Delta H_0$ (Oe) | $H_A$ (kOe) | $H_0$ (Oe) | $\Delta H_0$ (Oe) | $H_A$ (kOe) |
| Zn(Mn)-Y S1 | 962 | 11 | -9.39 | 2908 | 18 | -8.86 |
| Zn(Mn)-Y S2 | 949 | 13 | -9.32 | 2807 | 20 | -9.20 |
| Zn(Mn)-Y S3 | 931 | 13 | -9.61 | 2762 | 20 | -9.5 |
| Zn(Mn)-Y S4 | 916 | 13 | -9.58 | - | - | - |
| Zn(Mn)-Y S5 | 755 | 10 | -9.37 | - | - | - |
| Zn(Mn)-Y S6 | 796 | 12 | -9.38 | 2602 | 15 | -9.54 |
| Zn-Y SP1 | 1049 | 23 | -8.26 | 2987 | 36 | -8.38 |
| Zn-Y SP2 | 989 | 23 | -8.57 | - | - | - |
| Zn-Y SP3 | 972 | 16 | -8.75 | - | - | - |

frequency. This agrees with the linear dependent frequency loss mechanism. The $\Delta H_0$ values are much smaller for Zn(Mn)-Y than for Zn-Y because of the negligible conductivity in Zn(Mn)-Y, as discussed in Section 3.1.

Table 6.2 shows that when $H_A$ and $4\pi M_s$ are large compared to $H$ and samples are not very thin, demagnetizing factors calculated from Eq. (4.4) do not describe the reality precisely. The $h_{crit}$ data in Section 5.2 for the hipped YIG disk also showed that thick disks could not be well enough approximated by an ellipsoid. One may also assume that a disk or slab sample is not uniformly magnetized. Therefore, the concept of demagnetizing factors and the assumption of a uniformly magnetized sample should be used only as approximate models.

This section established sample geometry and presented the results of the FMR measurements. The objective of these measurements was the determination of the anisotropy field $H_A$, the FMR linewidth $\Delta H_0$, and the analysis of the demagnetizing factor concept. The anisotropy field and the demagnetizing factors will be important parameters in the spin wave instability analysis in this chapter. The FMR linewidth is a measure of microwave loss and will be compared with the spin wave linewidth. The next section will present results of parallel pumping measurements in Zn(Mn)-Y and Zn-Y .

### 6.2. Parallel Pumping in Zn-Y – Size Effects

Consider a thin plate single domain ferrite sample with easy plane anisotropy in the plane of the plate. The sample is magnetized to saturation by an external applied uniform static magnetic field **H** which is in the plane of the plate. A linearly polarized microwave pumping field **h** is applied parallel to **H** and parametric spin waves at a frequency $\omega_k$ = $\omega/2$ are excited above some field dependent threshold microwave field amplitude $h_{crit}$. The threshold microwave field amplitude for this geometry follows from Eqs. (2.65-2.68) and may be written as (Nazarov *et al.* [2002])

$$h_c(\theta_k,\varphi_k) = \frac{\Delta H_k \omega}{|\gamma||4\pi M_s \sin^2\theta_k \exp(2i\varphi_k) + |H_A||}. \tag{6.2}$$

As discussed in Section 2.3, Eq. (6.2) gives $h_c$ for particular spin waves with polar and azimuthal propagation angles $\theta_k$ and $\varphi_k$. These angles are defined in a standard right handed ($x$, $y$, $z$) coordinate system shown in Fig. 6.2 with an $x$-axis which is perpendicular to the plate and a $z$-axis parallel to the in-plane static field **H**.

As evident from Eq. (6.2), if the spin wave relaxation rate and corresponding linewidth is independent of the spin wave wave number $k$ and the angles $\theta_k$ and $\varphi_k$, the critical field $h_{crit}$ will be minimum for $\theta_k = 90°$ and $\varphi_k = 0$. Note that this spin wave propagation direction is *perpendicular* to the plate. One important implication from the data to follow is that thin plate surface boundary effects can increase the threshold for this type of critical mode and force the wave vector for the excited spin wave in plane. These effects were discussed in Chapter 4 for thin 10 μm YIG films.

The range of available spin waves at $\omega_k = \omega/2$ may be defined from the appropriate spin wave dispersion relation of Eq. (2.79) for easy plane hexagonal ferrites in the case of $\theta_H = \theta_M = 90°$,

$$(\omega_k/|\gamma|)^2 = [H - 4\pi M_s N_z + Dk^2][H - 4\pi M_s N_z + Dk^2 - H_A]$$
$$+ 4\pi M_s \sin^2\theta_k [H - 4\pi M_s N_z + Dk^2 - H_A \sin^2\varphi_k], \tag{6.3}$$

where $N_z$ is the demagnetizing factor in the direction of the static field **H**. For a thin plate with **H** in-plane, the demagnetizing factor $N_z$ is close to zero.

Figure 6.3 shows the principal spin wave dispersion branches from Eq. (6.3) for the indicated values of $\theta_k$ and $\varphi_k$ and labeled as A, B, C, and C′. The horizontal dashed lines indicate constant frequency cuts at 9/2 = 4.5 GHz and 16.7/2 = 8.35 GHz. For the dispersion evaluations, $\gamma$ was set to the free electron value, with $|\gamma|/2\pi$ = 2.8 GHz/kOe and the internal field $H-4\pi M_s N_z$ was set to 100 Oe. The anisotropy field parameter $H_A$ was set to −9.4 kOe and the saturation induction $4\pi M_s$ was set to 2.33 kG, based on data described in the previous section for Zn(Mn)-Y. Reliable values for the exchange parameter $D$ in Zn-Y are scarce. Mita and Shimizu [1973 and 1975] cite values of 7-$9\times10^{-9}$ Oe·cm$^2$/rad$^2$ for a spin wave propagation direction along the $c$-axis and values about 50 times smaller for propagation in the $c$-plane. Curves A, B, and C were evaluated for $D = 5\times10^{-9}$ Oe·cm$^2$/rad$^2$, the well known value for yttrium iron garnet (Gurevich and Melkov [1996]). The C′ curve was obtained for a 50 times smaller $D$-value and is included to show the effect of the reduced exchange (Mita and Shimizu [1973 and 1975]). The 4.5 and 8.35 GHz horizontal cuts correspond to half frequency spin waves for the 9 and 16.7 GHz pumping frequencies in the experiment.

The purpose of Fig. 6.3 is to show the possible critical spin wave modes which may play a role in the parallel pumping experiment. From the above discussion and Eq. (6.2), one would expect the minimum threshold critical mode to lie on curve B ($\theta_k = 90°$ and $\varphi_k$ = 0) at the appropriate horizontal line frequency cut point. As noted above, however, curve B corresponds to a **k** vector which is perpendicular to the plate plane. If, for some reason, such modes were pushed to a higher threshold, branch C provides an alternative

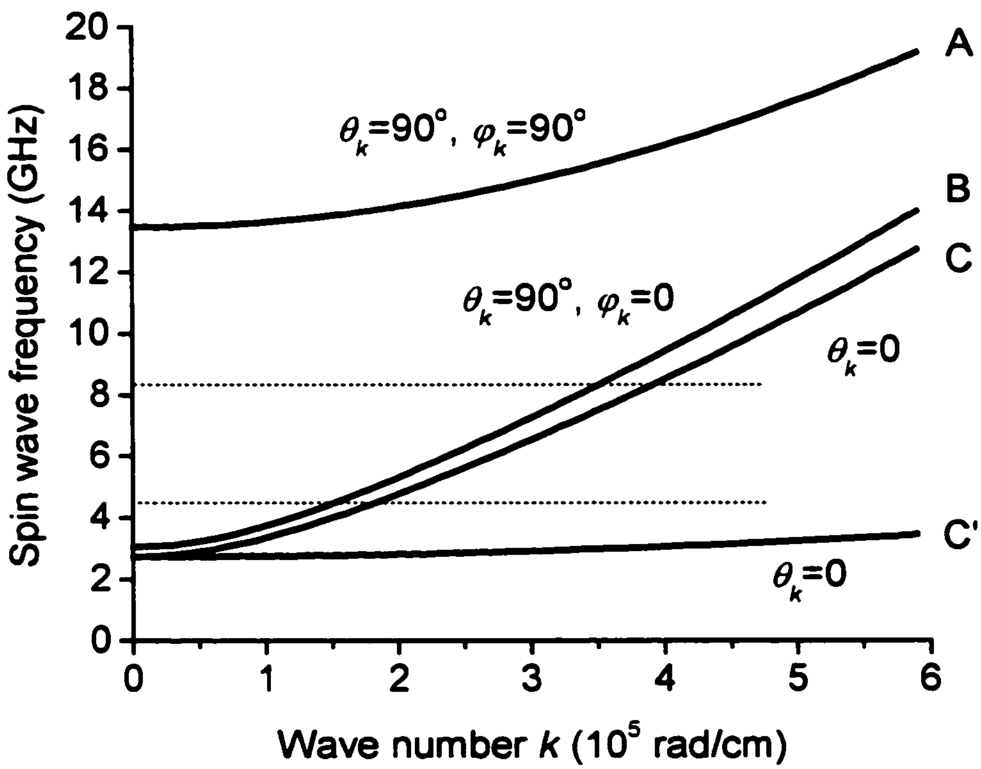


Figure 6.3. Schematic bulk spin wave dispersion diagram for a Zn-Y easy plane plate with the static internal in-plane field set to 100 Oe. The graph shows four dispersion curves of spin wave frequency vs. wave number $k$. The angles $\theta_k$ and $\varphi_k$ indicated for each curve designate the polar and azimuthal spin wave propagation angles. The dashed lines correspond to the half frequency spin waves at 4.5 and 8.35 GHz which are excited in the 9 GHz and 16.7 GHz parallel pumping experiments. Curves A, B, and C are for an exchange parameter $D = 5\times10^{-9}$ Oe·cm$^2$/rad$^2$. Curve C′ was calculated for an exchange value $D' = D/50$.

critical mode point for which the wave vector **k** is in plane. Since parallel pumping generally favors half frequency spin waves at $\theta_k = 90°$, one might think that a critical mode jump to curve A would be preferred. From Eq. (6.2), however, one can see that a critical mode point on curve A would have the highest possible threshold.

The above scenario would be changed significantly if there is a reduced exchange for a critical mode **k** vector in the c-plane and the plane of the slab. A reduced exchange would bend down curve C significantly, as indicated by the C′ curve. The large increase in $k$ which would then result from a jump from curve B to C′ would make such a jump highly unlikely.

The parallel pumping measurements were performed at 9 and 16.7 GHz. For the 9 GHz high Q cavity measurements, the system yielded direct data on cavity loss vs. microwave field amplitude similar to the results in Fig. 3.5. The experimental $h_{crit}$ results were obtained directly from these computer generated plots by the extrapolation method. Because of the small filling factors, the nonlinear response was generally quite weak and the accuracy of the $h_{crit}$ determinations was about 15%. Care was taken to make sure that the cavity response at power levels slightly above threshold was not affected by sample heating.

At 16.7 GHz, the larger filling factors made it possible to use a much more rapid and accurate visual determination of the thresholds. In this approach, one simply notes the value of the incident power at the point where the trailing edge of the pulse shows a visible nonlinear response, as shown in Fig. 3.4. Due to the larger filling factor, the accuracy of these threshold determinations was significantly higher than those at 9 GHz, and gave $h_{crit}$ values with an error of about 5%. The pulse shape based $h_{crit}$ determination technique and the low Q cavity eliminated any problems with sample heating.

The results of the parallel pumping measurements are summarized in Table 6.3. The table lists minimum $h_{crit}$ values for both measurement frequency ranges. The table also gives computed values of the spin wave linewidth $\Delta H_k$ from Eq. (6.2). For 16.7 GHz, these $\Delta H_k$ values correspond to the expected minimum threshold critical modes with $\theta_k$ = 90° and $\varphi_k = 0$, as discussed above. For 9 GHz, the listed $\Delta H_k$ values correspond to $\theta_k = 0$. This change is related to the size effects noted in the introduction and discussed in detail below. The results for rectangular samples S5 and S6 are given for fields parallel to the "long" and "short" sides of the slabs, as indicated. For these samples, the linewidths were obtained for static fields parallel to the "long" dimension.

The key measurement result from Table 6.3 concerns the minimum $h_{crit}$ values. At 16.7 GHz, these data show no significant change from sample to sample. At 9 GHz, however, these minimum $h_{crit}$ values show large sample-to-sample changes. Moreover, the main correlation appears to be with the lateral size. A smaller size generally gives a larger threshold. There is no apparent correlation with thickness. Note, for example, that samples S1, S2, and S4 all have about the same lateral size and similar 9 GHz $h_{crit}$ values, even though the thicknesses for these samples vary by a factor of four. Sample S3 has a smaller diameter and a larger threshold. For the rectangular samples S5 and S6, the minimum $h_{crit}$ values also change with the field direction from along the long side to along the short side.

The second important result from Tables 6.2 and 6.3 concerns connections between the computed spin wave linewidths and the measured FMR linewidths. If one adopts the

Table 6.3. Zn(Mn)-Y and Zn-Y high power properties.

| Sample | Minimum $h_{crit}$ at 16.7 GHz (Oe) | Minimum $\Delta H_k$ at 8.35 GHz (Oe) | Minimum $h_{crit}$ at 9 GHz (Oe) | Minimum $\Delta H_k$ at 4.5 GHz (Oe) |
|---|---|---|---|---|
| Zn(Mn)-Y S1 | 6.1 | 12 | 1.0 | 2.9 |
| Zn(Mn)-Y S2 | 6.5 | 12.8 | 0.9 | 2.6 |
| Zn(Mn)-Y S3 | 6.6 | 13.0 | 1.8 | 5.3 |
| Zn(Mn)-Y S4 | 6.4 | 12.6 | 1.2 | 3.5 |
| Zn(Mn)-Y S5 | long 6.6<br>short 6.6 | long 13.0<br>short 13.0 | long 2.2<br>short 3.5 | long 6.4<br>short 10.2 |
| Zn(Mn)-Y S6 | - | - | long 3.0<br>short 3.5 | long 8.8<br>short 10.2 |
| Zn-Y SP1 | 5.1 | 9.7 | 1.0 | 3.5 |

usual assumption of a linewidth which scales with frequency, one would expect the 8.35 GHz $\Delta H_k$ values extracted from the 16.7 GHz minimum $h_{crit}$ data to be close to the 9.5 GHz FMR linewidths. One would also expect the FMR linewidths at 17.5 GHz to be somewhat larger than these values. Both expectations are satisfied by the data in Tables 6.2 and 6.3. The 4.5 GHz $\Delta H_k$ values extracted from the 9 GHz minimum $h_{crit}$ data are not consistent with this expectation. Some of these linewidths are larger and some are smaller. As noted above, the 9 GHz minimum $h_{crit}$ data vary from sample to sample and appear to be correlated with lateral size.

Overall, the data in Tables 6.2 and 6.3 for Zn(Mn)-Y give (1) 16.7 GHz thresholds and spin wave linewidths which are consistent with the 17.5 GHz and 9.5 GHz linewidth results and are sample independent, and (2) 9 GHz thresholds and spin wave linewidths which vary from sample to sample and show no clear correlation with the FMR linewidth results. These very different results for the 16.7 and 9 GHz high power data will have important consequences for the size effect discussion of the next section.

Compare now the high power response of pure Zn-Y with the high power response of Zn(Mn)-Y. The FMR data of Table 6.2 for pure Zn-Y show that the FMR linewidth in pure Zn-Y is defined by eddy current losses (Truedson [1993]). The high power data of Table 6.3 show that $\Delta H_k$ in pure Zn-Y is similar to $\Delta H_k$ in Zn(Mn)-Y for both high and low frequencies. A similar size effect was discovered at low frequency in pure Zn-Y, although it was somewhat smaller. This implies that the spin wave linewidth in pure Zn-Y is not affected by the eddy current loss mechanism. This observation is important for the future investigation of the loss mechanisms in easy plane hexagonal ferrites. From now on in this chapter, the data and the analysis will be presented only for Zn(Mn)-Y.

Consider first the $h_{crit}$ response at 16.7 GHz. The results of parallel pumping measurements are shown in Figs. 6.4 and 6.5. The solid circles in Figs. 6.4 show the 16.7 GHz data for disks S1, S2, and S4. The solid circles in Figs. 6.5 show the 16.7 GHz data for sample S5. For S5, data are shown for both the long and the short field directions, as indicated. The solid lines in the figures show the theoretical response from Eq. (6.2) and the minimization procedure described in Section 2.4. The spin wave linewidth $\Delta H_k$ was set to constant values of 12 Oe for S1, 12.8 Oe for S2, 12.6 Oe for S4, and 13 Oe for both orientations of S5, the same as listed in Table 6.3. The demagnetizing field was set to 850 Oe for S1, 650 Oe for S2, 400 Oe for S4, 50 Oe for S5 long, and 200 Oe for S5 short. These demagnetizing factors correspond to $N_z$ values of 0.36 Oe for S1, 0.28 Oe for S2, 0.17 Oe for S4, 0.02 Oe for S5 long, and 0.09 Oe for S5 short. One can see that these are much larger than given in Table 6.1. The discussion on this difference will be developed shortly.

The most important result in Figs. 6.4 and 6.5, compared to the 9 GHz data, is the nearly textbook response found experimentally for parallel pumping at 16.7 GHz. Recall that the critical modes are at half frequency, or 8.35 GHz. One can see that all the samples have the same response in this frequency range. The jump in the data at low $H$ is attributed to demagnetizing effects. Above this field, the sample is saturated and the model calculations can be compared to the data.

Consider Fig. 6.4(a) as an example. The measured $h_{crit}$ drops from about 7.5 Oe at $H$ = 300 Oe to about 6 Oe at $H$ = 1000 Oe and then is approximately constant up to $H \sim$ 1500 Oe. There is a distinct kink at $H \sim$ 1500 Oe, followed by an increase and truncation at $H \sim$ 1700 Oe.

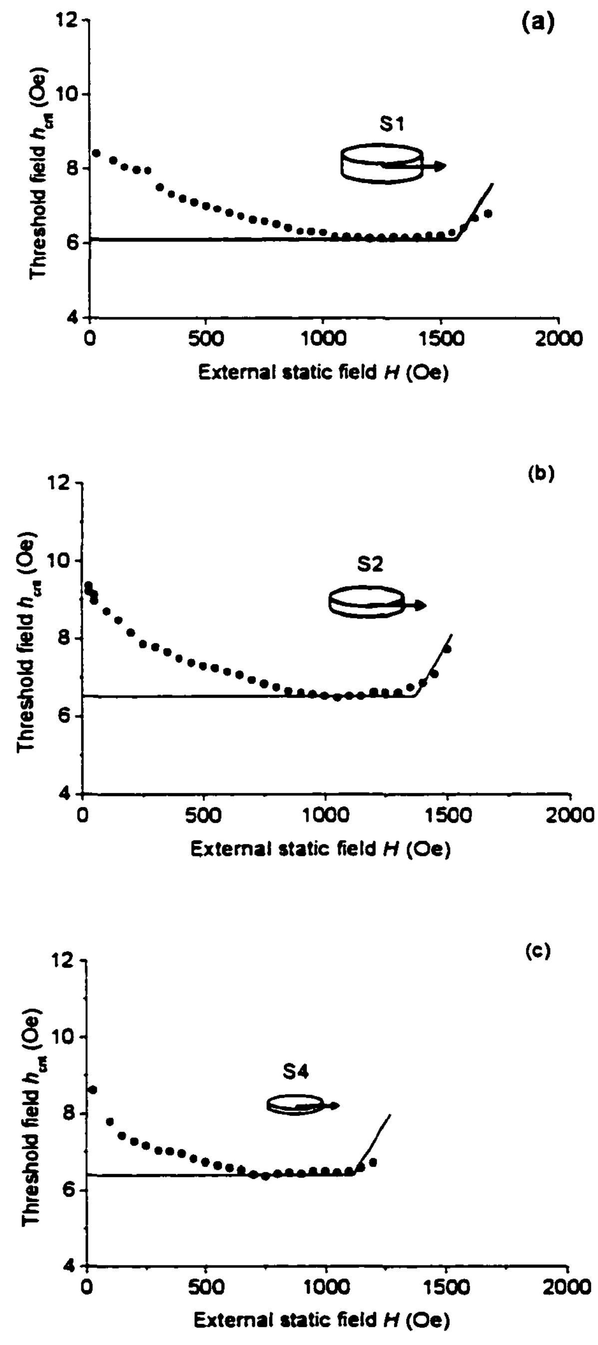


Figure 6.4. Parallel pumping threshold $h_{crit}$ as a function of the external static field $H$ for the in-plane magnetized Zn(Mn)-Y disks S1 (a), S2 (b), and S3 (c) with 16.7 GHz microwave excitation. The data and theory are shown by the solid circles and solid lines, respectively. The numerical calculations were done for constant spin wave linewidth $\Delta H_k$ values of 12 Oe for S1, 12.8 Oe for S2, and 12.6 Oe for S4. The demagnetizing field $H_{dem}$ was set to 850 Oe for S1, 650 Oe for S2, and 400 Oe for S4.

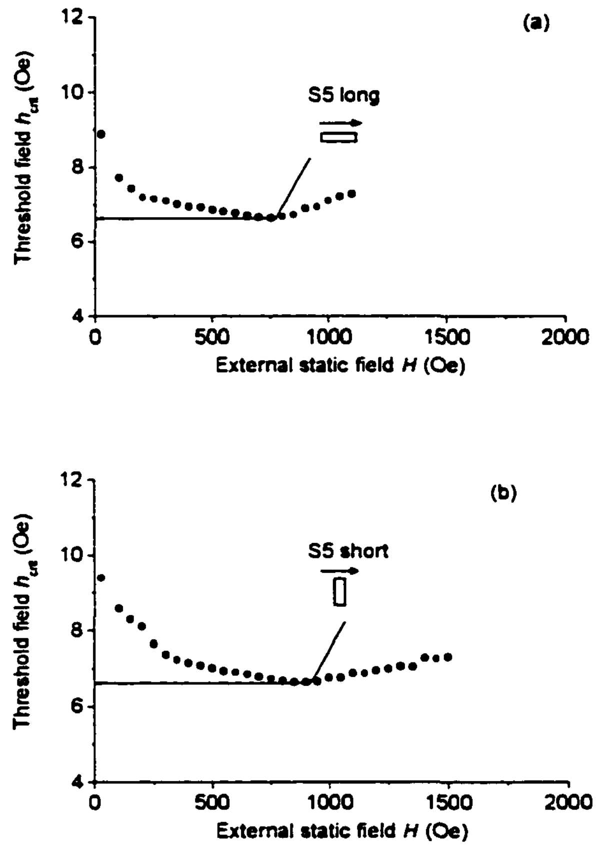


Figure 6.5. Parallel pumping threshold $h_{crit}$ as a function of the external static field $H$ for the in-plane magnetized Zn(Mn)-Y rectangular slab S5 with 16.7 GHz microwave excitation. The labels "S5 long" and "S5 short" indicate the static field orientation along the long (a) and short (b) sides of the rectangular plate, as indicated. The data and theory are shown by the solid circles and solid lines, respectively. The numerical calculations were done for the constant spin wave linewidth $\Delta H_k$ value of 13 Oe for both orientations. The demagnetizing field $H_{dem}$ was set to 50 Oe for S5 long and 200 Oe for S5 short.

The calculated curve for $\Delta H_k$ = 12 Oe provides a good match to the data from $H$ ~ 1000 Oe up to the truncation point. The kink at $H$ ~ 1500 Oe corresponds to the point where the half frequency spin waves are forced to $k = 0$ as discussed in Section 2.4. The increase in the calculated $h_{crit}$ above this kink field point is due to a decrease in the $\theta_k$ for the critical modes. The $h_{crit}$ versus field curve then truncates at $H$ ~ 1700 Oe as the critical mode goes to $\theta_k = 0$. There are no critical modes available for instability at higher fields. The match up of the theory to the data from the kink point to the truncation field provides proof positive that the critical modes lie on curve B in Fig. 6.3. Otherwise, there would be no kink in the response. This means that the minimum threshold spin waves below the kink point have $\theta_k = 90°$ and $\varphi_k = 0$ and a **k** which is perpendicular to the static field and the disk plane.

One can also see that although butterfly curves in Figs. 6.4 and 6.5 look similar, there are important differences in the $h_{crit}$ response. First, the distinct $h_{crit}$ minimum exists only for sample S5 magnetized in a long direction shown in Fig. 6.5(a). The somewhat less distinct $h_{crit}$ minimum can be seen in Figs. 6.4(c) and 6.5(b). This minimum is completely obscured for the S1 disk in Fig. 6.4(a) and is not pronounced for S2 in Fig. 6.4(b). This is due to the distribution of the demagnetizing fields because these samples are not ellipsoids. The similar situation was observed for the thick polycrystalline YIG disk in Chapter 5, where the flat region of $h_{crit}$ was also present. This region was caused by the non-uniformly magnetized sample. As discussed in the previous section, the field inhomogeneity is Zn-Y is even bigger due to larger values of $4\pi M_s$ and $H_A$. The influence of the inhomogeneous demagnetizing fields will be very important in the analysis of oblique pumping data presented in the next two sections.

Note that that the $N_z$ values obtained from the $h_{crit}$ minimum positions in Fig. 6.5 for both orientations of S5 are very close to $N_z$ values in Table 6.1. This will also hold for S4 if one places the kink point at the $h_{crit}$ minimum at $H$ ~ 750 Oe in Fig. 6.4(c). The increase in the measured $h_{crit}$ as the field $H$ falls below the $h_{crit}$ minimum positions may be attributed to an increase in $\Delta H_k$ with $k$ for Zn-Y (Gurevich *et al.* [1999]). Such an increase in $k$ is evident from Fig. 6.3. The point at which the 8.35 GHz dashed line cut crosses the ($\theta_k = 90°$, $\varphi_k = 0$) dispersion branch line (curve B) determines the critical mode $k$ value. This intersection point moves to higher $k$ as the field is decreased and curve B moves down.

The analysis of the $\Delta H_k$ vs. $k$ dependence is presented for the $h_{crit}$ data in Figs. 6.4(c), 6.5(a), and 6.5(b), where an $h_{crit}$ minimum is distinct. The wave number value can be obtained from Eq. (3.10) for $D = 5\times10^{-9}$ Oe·cm$^2$/rad$^2$. The $H_c$ value was taken to correspond to the minimum of $h_{crit}$. Equation (6.2) relates $h_{crit}$ and $\Delta H_k$ for $\theta_k = 90°$ and $\varphi_k = 0$.

Figure 6.6 shows the calculated $\Delta H_k$ vs. $k$ response for the Zn(Mn)-Y disk S4 and rectangular plate S5. At $k$ larger than $3.5\times10^5$ rad/cm, $H$ is less than the demagnetizing field and $\Delta H_k$ increases due to the domain formation. Therefore, the maximum $k$-dependent $\Delta H_k$ is about 14.5 Oe. The important feature is the exact match in the data for the two orientations of S5. At $k$ larger than $2.5\times10^5$ rad/cm all three curves coincide. This is expected for the samples made of same material, as shown in Chapters 4 and 5.

The data are very similar to the $\Delta H_k$ vs. $k$ data for 36 GHz parallel pumping (Gurevich *et al.* [1999]). The quadratic $\Delta H_k$ increase is a signature of the possible four magnon processes. The important result is that the $k$ contribution to the spin wave

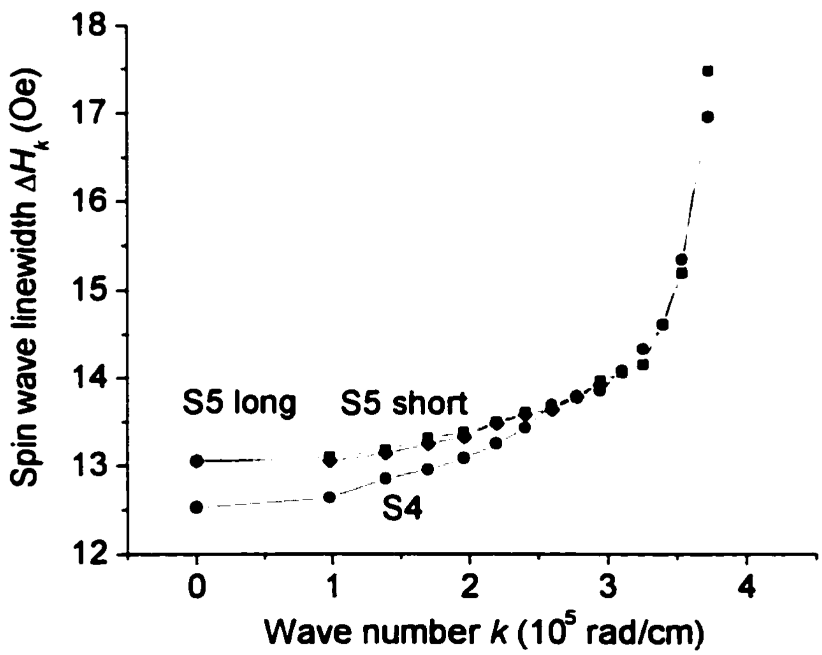


Figure 6.6. Spin wave linewidth $\Delta H_k$ vs. wave number $k$ for Zn(Mn)-Y disk S4 and rectangular plate S5. The static field was in plane and the pumping frequency was 16.7 GHz. The labels "S5 long" and "S5 short" indicate the static field orientation along the short and long sides of the rectangular plate, as indicated.

linewidth is significantly lower than $\Delta H_{k=0}$, which ranges from 12 to 13 Oe in Zn(Mn)-Y. The difference at low $k$ may be related to sample dimensions. This effect for 16.7 GHz data is small but it will be significant for the low frequency $h_{crit}$ data.

As noted, the above data and the fit of the calculated curve to the data constitute a nearly textbook hexagonal ferrite butterfly curve response. These results are in strong contrast with the data for 9 GHz. Figure 6.7 shows representative 9 GHz results on $h_{crit}$ as a function of $H$ for parallel pumping in the disk sample S1 and the rectangular plate sample S5. The icons and arrows show the relative lateral sizes and field orientations for the samples. Butterfly curve data for the S5 slab are shown for static fields along the long and short sides of the rectangle, as indicated.

The low field limit of the data in each case corresponds to the saturation field for that particular sample. This field is smallest for the rectangle with the field parallel to the long edge, intermediate for the rectangle with the field along the short edge, and largest for the relatively thick disk sample. The jump in $h_{crit}$ below $H \sim 300$ Oe for sample S1 is due to this effect and is at the same field point as in Fig. 6.4(a). The ranges of static fields for the data on each sample are all about the same. This confirms the fact that the threshold data are for about the same range of internal fields defined by the critical mode limits discussed above. The S5 data sets truncate at some high field limit as discussed above. The high field limit for S1 was set by the proximity of the magnetostatic mode resonances for fields above about 650 Oe. These particular data were selected to demonstrate the effect of sample size on the thresholds at 9 GHz. As Table 6.3 shows, the other samples give minimum $h_{crit}$ values which range between 0.9 and 3.5 Oe, the same range as the data in the figure. As noted in the introduction, a larger lateral size

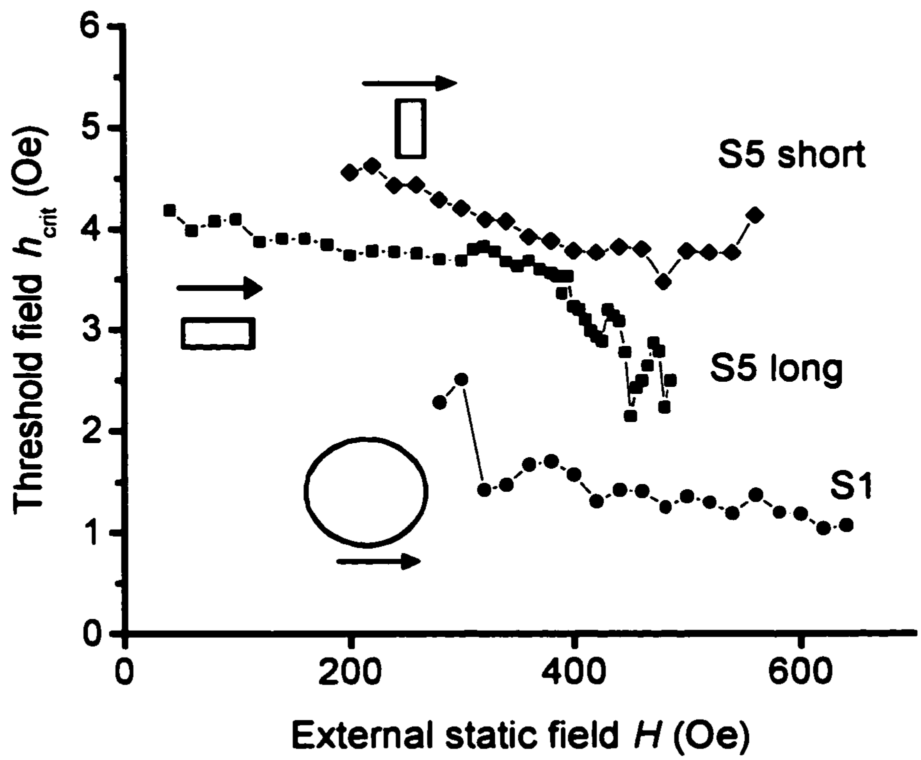


Figure 6.7. Data on the parallel pumping spin wave instability threshold $h_{crit}$ as a function of the external static field $H$ for the Zn(Mn)-Y disk S1 and rectangular plate S5. The static field was in plane and the pumping frequency was 9 GHz. The labels "S5 long" and "S5 short" indicate the static field orientation along the short and long sides of the rectangular plate, as indicated.

generally corresponds to a lower threshold. The data in Fig. 6.7 and Table 6.3 constitute the proof of this effect.

There is one final experimental point to note from the data in Fig. 6.7. For sample S5, with $H$ along the long edge of the slab, one can see several distinct dips at the high field end of the butterfly curve. When S5 has the field along the short side, the data appear to show one somewhat less pronounced dip. The presence of these dips, in combination with the overall lateral size correlations for the 9 GHz thresholds, will be the starting point for the discussion below. These results support qualitative and quantitative arguments for critical modes in the 9 GHz measurements which have an in-plane wave vector, rather than the out-of-plane **k** from the theory and the data at 16.7 GHz.

The data in Figs. 6.4, 6.5, and 6.7 and Table 6.3 show important contrasts between the high power response in the 9 GHz low frequency and the 16 GHz high frequency ranges. The 16.7 GHz data show (1) an almost textbook $h_{crit}$ versus $H$ response, (2) no significant effect of sample size or thickness, and (3) a $\Delta H_k$ versus $k$ response which matches previous data for Zn-Y. The data and the correlation with theory indicate that the critical modes have wave vectors which are perpendicular to the $c$-plane plates. In contrast, the 9 GHz data show a strong sample-to-sample variation in the $h_{crit}$ values and the butterfly curve profiles. The thresholds depend on the lateral sample size but not the thickness.

One way to reconcile the lateral sample size dependence for the $h_{crit}$ response at 9 GHz is to make an *ad hoc* assumption that the critical modes have **k** vectors which lie in the plane of the plates, even though the bulk theory gives a minimum threshold for a perpendicular **k** direction. There are two related arguments to support such an assumption. First, the lateral size dependence for $h_{crit}$ suggests that the critical modes lie in plane. Arguments are given below to support this suggestion. Second, the bulk theory gives only a 20% increase in $h_{crit}$ as one moves the critical mode wave vector from perpendicular ($\theta_k = 90°$, $\varphi_k = 0$) to in plane ($\theta_k = 0°$). If there are factors which push the critical mode **k** vector in plane, the effect would not have to be very large to override the bulk prediction.

One can envision a transit time effect to push the critical mode **k** in plane. Transit time models have often been invoked to explain the dependence of $h_{crit}$ on grain size in polycrystalline ferrites as discussed in Section 5.3. The basic idea is that some dimension $d$ in combination with the group velocity $v_g$ of the mode can define a transit time $T_d = d/v_g$. If $T_d$ is less than the intrinsic relaxation time $T_k$, then the dimension $d$ limits the lifetime of the mode instead of intrinsic processes. For spin wave instability considerations, one would then replaces the intrinsic spin wave linewidth $\Delta H_k = 2/|\gamma| T_k$ with a transit time limited linewidth parameter $\Delta H_T = 2/|\gamma| T_d = 2v_g/|\gamma| d$.

In the present context, this transit time model can push the critical modes in plane. As listed in Table 6.1, the lateral size $L$ is typically greater than the sample thickness, so that the transit time limited $\Delta H_k$ for modes propagating in plane will be smaller. From the data given above, the average threshold follows the relation $\langle h_{crit} \rangle = C/L$, where $C$ is on the order of 0.3 Oe·cm. From Eq. (6.2) with critical modes on branch C in Fig. 6.3 with $\theta_k = 0°$, the transit model gives

$$C = \frac{2\omega v_g}{|\gamma|^2 H_A}. \tag{6.4}$$

A match to the empirical $C$ value noted above requires a group velocity on the order of $8\times10^6$ cm/s. Such group velocities are in the range expected for low $k$ magnetostatic modes in the relatively thick plates used in the current measurements.

Even though the above model offers a plausible argument for in-plane critical modes and sample size dependent thresholds which agree qualitatively with the data, there are still many unresolved problems. Why, for example, do these effects occur at 9 GHz but not at 16.7 GHz? As the threshold data and theoretical comparisons in Fig. 6.4 show, the 16.7 GHz response matches expectations from the bulk spin wave theory. A second question concerns the wave numbers for the critical modes. The critical modes for the 16.7 GHz data clearly have wave numbers which range from near zero at the butterfly curve minimum up to values on the order of $3\text{-}4\times10^5$ rad/cm at low field. These values, as well as the upturn in threshold as the field is reduced are consistent with the bulk theory as well as the detailed measurements at 36 GHz (Gurevich *et al.* [1999]).

For the transit time arguments to apply at 9 GHz, however, one requires low $k$ modes. The usual high $k$ exchange dominated critical modes which explain the 16.7 GHz data have very low group velocities and scattering lifetimes which are well above the intrinsic spin wave lifetimes. One possible signature for the presence of low $k$ critical modes at 9 GHz is given by the structure in the butterfly curve data in Fig. 6.7 for the rectangular sample S5. When the field is parallel to the long side, there are three pronounced equidistant dips over the field interval 400 - 480 Oe and a smaller dip at about 380 Oe. When the field is along the short side, there is a single dip at about 480 Oe. Such structure is the usual signature for low wave number standing mode resonances related to the sample dimensions (Wiese *et al.* [1994]).

One of the goals of the work on Zn-Y was the investigation of oblique pumping and application of the general spin wave instability theory developed in Chapter 2. The sample size effect at 9 GHz and proximity of the butterfly curves to the FMR field position made the investigation of oblique pumping impossible at this frequency. This resulted in the $h_{crit}$ measurements at 16.7 GHz where butterfly curves were independent of samples, except for demagnetizing effects. The analysis of these measurements validated the assumption that at 16.7 GHz the sample size effect is not important and it is possible to investigate oblique pumping. Now the parallel pumping results will be extended to more complicated pumping configurations.

### 6.3. In-plane Oblique Pumping

The example calculations in Section 2.4 were done for out of plane oblique pumping at 17 GHz in Zn-Y. The results of parallel pumping measurements in the previous section demonstrated that size effects are important at 9 GHz but not at 16.7 GHz and that oblique pumping could be investigated at 16.7 GHz. The next logical step would be out of plane oblique pumping $h_{crit}$ measurements. These measurements were performed and will be discussed in the next section. The out of plane oblique pumping $h_{crit}$ measurements involve non-collinear $\mathbf{M}_s$ and $\mathbf{H}$ and reveal certain details that require investigation of a simpler pumping configuration such as oblique pumping in the in-plane magnetized Zn-Y plate. But even simpler in-plane and out of plane perpendicular pumping data and analyses will be presented first.

Because of the demagnetizing effects discussed above one can learn the physics of oblique pumping from samples with small demagnetizing fields. Unfortunately, these samples are thin and fragile. Moreover, as discussed in Chapter 4, thin film geometry can affect the spin wave instability processes in thin films. Therefore, the measurements were performed on the intermediate thickness sample S2. The three main interests of the oblique pumping investigation were (1) the match between the data and the theory of Chapter 2, (2) the $\Delta H_k$ dependence on wave vector **k**, and (3) the effect of non-collinear $\mathbf{M}_s$ and **H** on spin wave damping $\Delta H_k$.

Figure 6.8 shows the data on the spin wave instability threshold field $h_{crit}$ as a function of $H$ for parallel, perpendicular in-plane, and perpendicular out of plane pumping in the Zn(Mn)-Y S2 disk at a pumping frequency of 16.7 GHz. The icons and arrows show the field orientations for the sample. The figure shows results for three different orientation of the microwave field $h$ along the $x$, $y$, and $z$ axes, as indicated. The disk is in the $y$-$z$ plane of the $(x, y, z)$ laboratory frame shown in Fig. 6.3. The field **H** is along the $z$-axis. Figure 6.8 also shows the results of the corresponding numerical calculations. The solid lines in the figure show the theoretical response from Eqs. (2.65)-(2.68) and the minimization procedure described in Section 2.4, based on the parameters specified above for the Zn(Mn)-Y S2 disk with one exception. In order to provide better fit to the data, the demagnetizing factors were set to $N_z = N_y = 0.13$ and $N_x = 0.74$. The spin wave linewidth $\Delta H_k$ was set to a constant value of 12.8 Oe for all three calculated curves, the same as listed in Table 6.3.

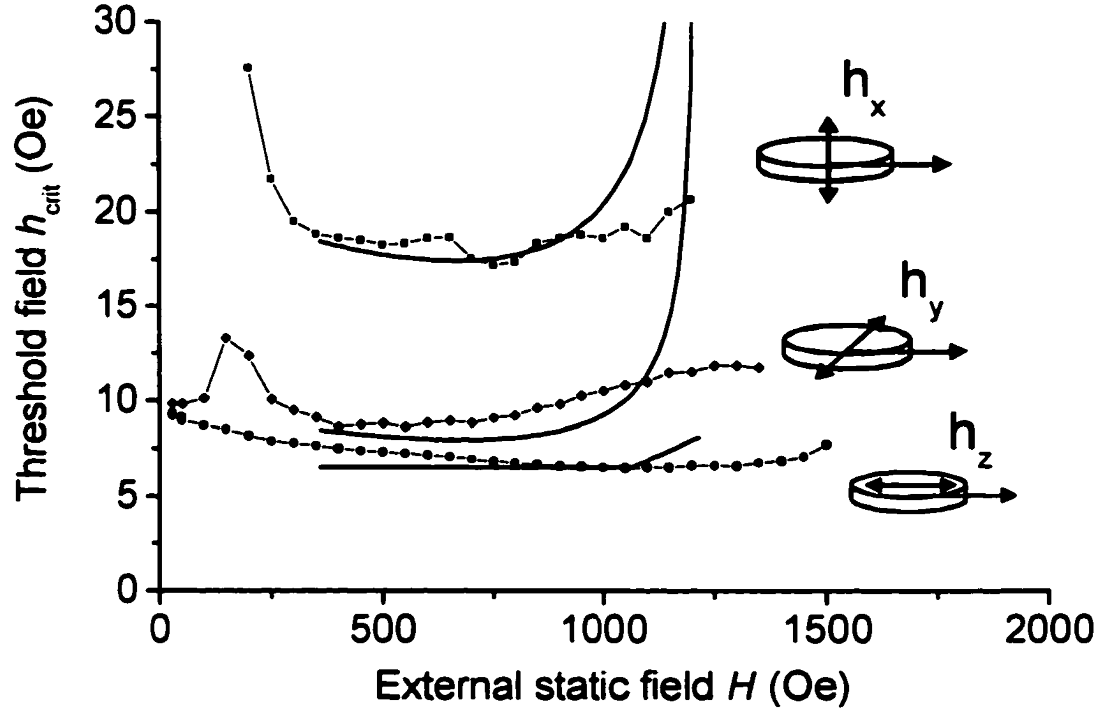


Figure 6.8. Parallel, perpendicular in-plane, and perpendicular out of plane pumping threshold $h_{crit}$ as a function of the external static field $H$ for Zn(Mn)-Y sample S2 with 16.7 GHz microwave excitation. The field $H$ is applied in-plane as it is shown in Fig. 6.2. The graphs show results for three different orientation of the microwave field $h$, as indicated. The solid lines show results of numerical calculations with $N_z = N_y = 0.13$ and $N_x = 0.74$. The spin wave linewidth $\Delta H_k$ was set to a constant value of 12.8 Oe.

Consider the experimental and calculated $h_{crit}$ response in Fig. 6.8. The parallel pumping response was discussed in detail in the previous section. One can see that for all three curves the data are in qualitative agreement with the calculated $h_{crit}$. The specific feature of the data for the in-plane and out of plane perpendicular pumping is a peak at low $H$, which is not predicted by theory. The peak field position is limited by $H \sim 300$ Oe. The peak is not present for the parallel pumping data. This peak probably originates from demagnetizing effects that impede the excitation of the uniform mode. The demagnetizing factors for S2 from Table 6.1 correspond to the demagnetizing field $H_{dem}$ of 150 Oe. One may conclude from the peak position that the real $H_{dem}$ is about 300 Oe. The demagnetizing factors used in the calculated curves in Fig. 6.8 correspond to this value of $H_{dem}$. The modified demagnetizing factors $N_z = N_y = 0.13$ and $N_x = 0.74$ will be used from now on in the calculations for S2.

The extension of all three butterfly curves above the theoretical cut off field $H_{cut} \sim 1200$ Oe is related to the inhomogeneous demagnetizing fields that were discussed in the previous section. Beyond that, the same $\Delta H_k$ of 12.8 Oe describes the $h_{crit}$ values well. Consider now the critical mode behavior for perpendicular in-plane and perpendicular out of plane pumping configurations. The important result of the numerical calculations is that the calculated critical modes $(k, \theta_k, \varphi_k)$ are exactly the same for these two perpendicular pumping curves and they will be presented and discussed next for an in-plane oblique pumping case. This result is not obvious because the different microwave field polarization not only changes the amplitude of the uniform mode but it also changes its polarization, which is defined by $x$ and $y$ components. These $h_{crit}$ data provide an important evidence that the theory of the uniform mode excitation describes the real data well enough!

Now the simplest pumping configurations are explored. They show that there is no unexplained differences in the $h_{crit}$ response for perpendicular in-plane and perpendicular out of plane pumping configurations and one can proceed to the results of the in-plane oblique pumping investigation.

Figure 6.9 shows the spin wave instability threshold field $h_{crit}$ as a function of $H$ for in-plane oblique pumping in the Zn(Mn)-Y S2 disk at a pumping frequency of 16.7 GHz. The figure shows the oblique pumping butterfly curve data for $\theta_h$ values of 90°, 60°, 45°, 30°, and 0, as indicated. The disk is in the $y$-$z$ plane of the ($x$, $y$, $z$) laboratory frame shown in Fig. 6.2. The field **H** is along the $z$-axis. The angle $\theta_h$ is an in-plane angle between $H$ and the linearly polarized microwave field **h**(t).

Consider the $h_{crit}$ response in Fig. 6.9. Note that butterfly curves for $\theta_h = 90°$ and $\theta_h = 0$ were already shown in Fig 6.8. At zero field, all curves start from the same $h_{crit}$ value. This is related to the fact that in the experiment, the field $H$ was rotated, at zero field the sample was unsaturated, and all $\theta_h$ configurations were identical. The low field peak for $\theta_h = 90°$ is slightly smaller for $\theta_h = 60°$. The sharp increase in $h_{crit}$ at $H \sim 300$ Oe as $H$ decreases is pronounced for all curves and originates from the presence of domains, the same as in Fig. 6.8. Note also that the butterfly curves for $\theta_h = 30°$ and $\theta_h = 45°$ are almost identical and yield the lowest minimum $h_{crit}$ among all $\theta_h$ values. This unusual effect will be discussed shortly. Now one can explore the data in Fig. 6.9.

Figure 6.10 shows the spin wave instability threshold field $h_{crit}$ data of Fig. 6.8 as a function of $H$ for in-plane oblique pumping in the Zn(Mn)-Y S2 disk at a pumping

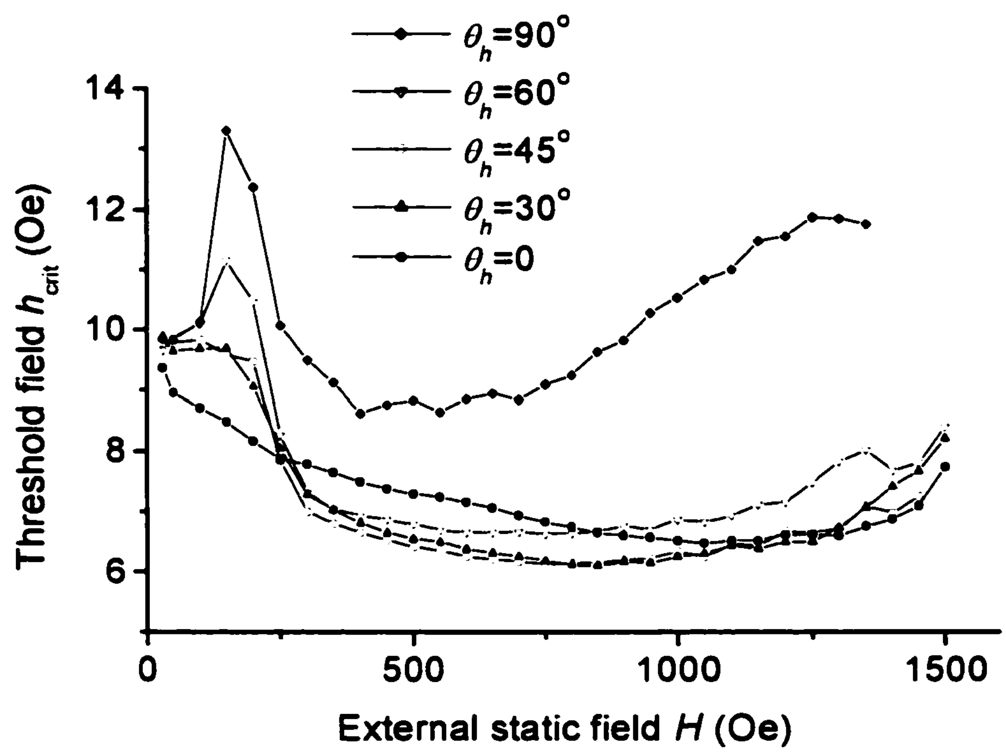


Figure 6.9. In-plane oblique pumping threshold $h_{crit}$ as a function of the external static field $H$ for the Zn(Mn)-Y sample S2 with 16.7 GHz microwave excitation. The field $H$ is applied in-plane as it is shown in Fig. 6.2. The graphs show results for values of $\theta_h$, the in-plane angle between $H$ and microwave field $h$, as indicated.

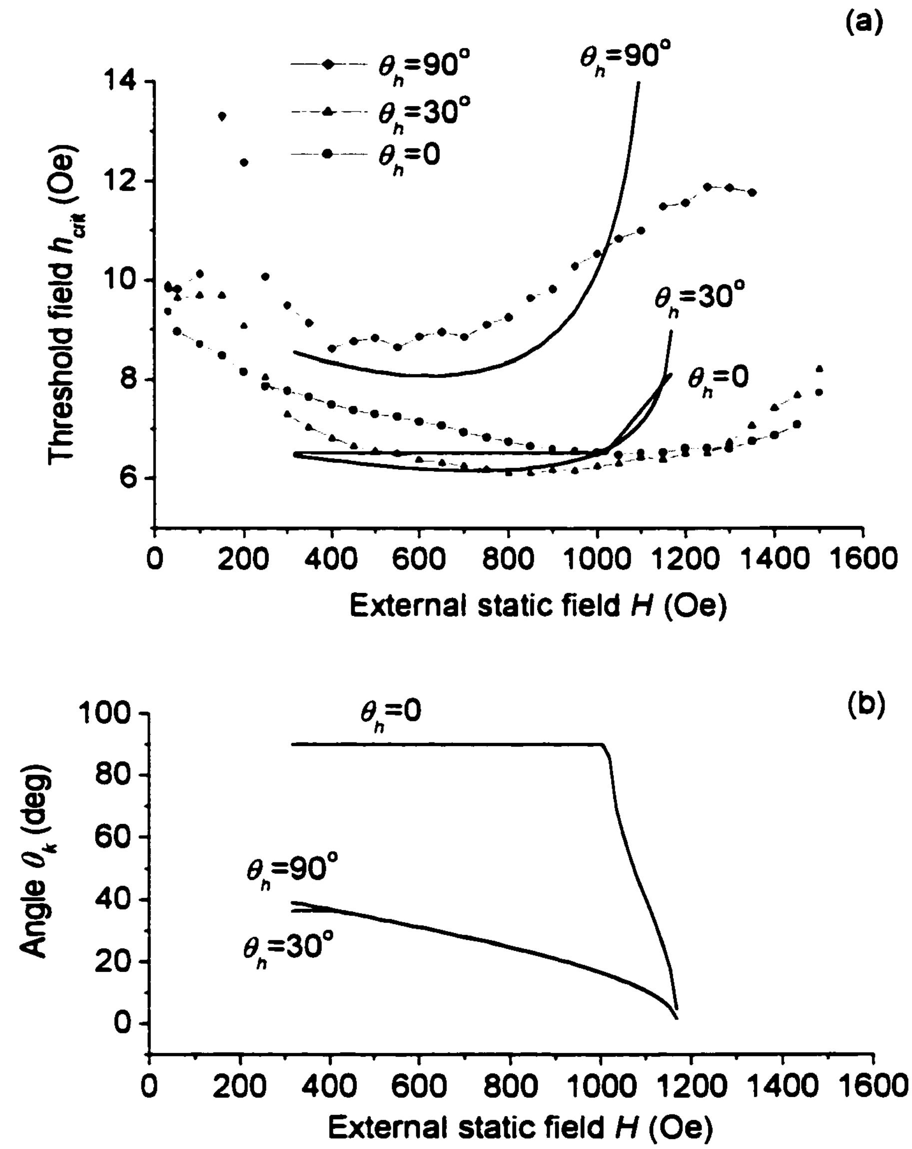


Figure 6.10. In-plane oblique pumping threshold $h_{crit}$ as a function of the external static field $H$ for the Zn(Mn)-Y sample S2 with 16.7 GHz microwave excitation. The graphs show (a) first order spin wave instability threshold field $h_{crit}$ vs. $H$ and (b) polar spin wave propagation angle $\theta_k$ vs. $H$. The graphs show results for values of $\theta_h$, the in-plane angle between $H$ and microwave field $h$, as indicated. The symbols show the data, the solid lines show the results of the numerical calculations. For the numerical calculations, the spin wave linewidth $\Delta H_k$ was set to a constant value of 12.8 Oe.

frequency of 16.7 GHz. The figure shows oblique pumping butterfly curve data for $\theta_h$ values of 90°, 30°, and 0. The solid lines in the figure show the theoretical response, calculated from Eqs. (2.65)-(2.68) and the minimization procedure of Section 2.4, based on the parameters specified above for the Zn(Mn)-Y S2 disk and modified demagnetizing tensor components. The graphs show (a) first order spin wave instability threshold field $h_{crit}$ vs. $H_{ext}$ and (b) polar spin wave propagation angle $\theta_k$ vs. $H_{ext}$. The spin wave linewidth $\Delta H_k$ was set to a constant value of 12.8 Oe for all calculated curves.

The calculated curves in Fig. 6.10(a) show some limited correlation with the data. The deviation between the calculated and experimental $h_{crit}$ is no more than 10 % in the field range from 300 Oe to 1050 Oe for all $\theta_h$ values. The important feature of Figs. 6.9 and 6.10(a) is the theoretical prediction that the minimum threshold realizes not for pure parallel or perpendicular pumping, but for oblique pumping. One can see that a $\theta_h$ value of 30° yields the lowest $h_{crit}$ curve. This phenomenon has never been observed in small anisotropy single crystal YIG. This oblique pumping minimum $h_{crit}$ has important practical applications for microwave ferrite devices.

Figure 6.10(b) shows the polar spin wave propagation angle $\theta_k$ vs. $H_{ext}$. One has the same response for $\theta_h$ values of 30° and 90° except for a small deviation at low fields. The $\theta_k$ response is completely different for $\theta_h = 0$ (parallel pumping) and was discussed in the previous section. The other critical mode parameters $k$ and $\varphi_k$ showed a similar response. Numerical calculations showed that for $\theta_h > 25°$ the wave number was independent of $H$ and was zero valued. The $\varphi_k$ value was close to 90°, as opposed to the values of zero or 180° for $\theta_h = 0$, discussed in Section 2.4. The zero $k$ values mean that it is possible to omit the $k$-dependence of $\Delta H_k$ in the $h_{crit}$ numerical calculations for the in-plane oblique pumping.

The same critical mode behavior for $\theta_h > 0$ implies that there is a certain transition angle $\theta_h$ at which the critical mode switches from the nearly parallel pumping critical mode with $\varphi_k = 0$ and nonzero $k$ to the oblique pumping critical mode with $\varphi_k \sim 90°$ and zero $k$. The numerical calculations showed that this transition occurs in the $\theta_h$ interval of 15° to 25°.

The further analysis was developed to investigate the combined effect of parallel and perpendicular pumping which produce oblique pumping. As discussed in Chapter 2, parallel pumping works directly through the $z$-component of the microwave field and perpendicular pumping works through the uniform mode. It is possible to separate and investigate numerically their contribution to $h_{crit}$. The $h_{crit}$ vs. $H$ curves were calculated for separate contribution of $h_z = h\cos\theta_h$ and $h_y = h\sin\theta_h$ for $\theta_h = 30°$. The calculations showed that each independent threshold is larger than the combined one which is shown in Fig. 6.10 (a). The fact that the oblique pumping $h_{crit}$ is smaller than the pure parallel pumping $h_{crit}$ or the pure perpendicular pumping $h_{crit}$ has the following explanation.

As was discussed by Liu and Patton [1982], the threshold for oblique pumping $h_{crit,obl}$ may be estimated as

$$\frac{1}{h_{crit,obl}} = \max\left(\frac{\cos\theta_h}{h_{crit,par}} + \frac{\sin\theta_h}{h_{crit,per}}\right), \tag{6.5}$$

where $h_{crit,par}$ is the parallel pumping threshold for $\theta_h = 0$ and $h_{crit,per}$ is the perpendicular pumping threshold for $\theta_h = 90°$. Simple estimates show that $h_{crit,obl}$ can be less than $h_{crit,par}$ and $h_{crit,per}$. This decrease can be seen in Fig. 6.10(a), which means that the parallel and perpendicular $h$ components act cooperatively to produce spin wave instability.

Another important consequence of the data analysis in Fig. 6.10 is the $\Delta H_k$ independence of the propagation direction for $k \sim 0$. The minimum $h_{crit}$ data for $\theta_h = 0$ yields $\Delta H_k$ of 12.8 Oe for ($k \sim 0$, $\theta_k = 90°$, $\varphi_k = 0$) critical mode. The minimum $h_{crit}$ data for $\theta_h = 30°$ yields $\Delta H_k$ of 12.8 Oe for ($k \sim 0$, $\theta_k \sim 30°$, $\varphi_k = 90°$) critical mode. Therefore, one can assume that $\Delta H_k$ does not significantly depend on the propagation direction for low wave numbers in Zn-Y. This result contradicts the conclusion made by Gurevich *et al.* [1999] for 36 GHz measurements. However, the 36 GHz measurements were done for the out of plane oblique pumping configuration when $\mathbf{M}_s$ is out of plane. This pumping configuration has different angles $\theta_H$ between $H$ and the disk normal. The butterfly curves for the similar out of plane oblique pumping configuration will be shown in the next section. The in-plane oblique pumping results suggest that $\Delta H_k$ is independent on the propagation direction when $\mathbf{M}_s$ is in-plane. The $\Delta H_k$ angular dependence when $\mathbf{M}_s$ is pulled out of the plane will be discussed below.

### 6.4. Out of Plane Oblique Pumping

The out of plane oblique pumping measurements were performed for the same pumping configuration as in Chapter 2. The effect of rotating the field $H$ which is shown in Fig. 2.4. is considered below. As one decreases $\theta_H$, the meaningful butterfly curve range increases, which corresponds to the transition from parallel pumping to oblique pumping. The results of the theoretical $h_{crit}$ and critical mode calculations for this geometry were shown in Fig. 2.5 and discussed in Section 2.4. The main difference is that in the experiment, disk samples had a finite thickness and this was taken into account through nonzero demagnetizing fields, the same way as in the previous section.

The out of plane oblique pumping measurements were performed on three disk samples S1, S2, and S4. The results of these measurements are summarized in Figs. 6.11-6.13. Figure 6.11 shows the oblique pumping $h_{crit}$ vs. $H$ data for S1 at 16.7 GHz for $\theta_H$ values of 90°, 42°, 7°, and 0, as indicated. Figure 6.12 shows the oblique pumping $h_{crit}$ vs. $H$ data for S2 at 16.7 GHz for $\theta_H$ values of 90°, 45°, 20°, 10°, 5°, and 0, as indicated. Figure 6.13 shows the oblique pumping $h_{crit}$ vs. $H$ data for S4 at 16.7 GHz for $\theta_H$ values of 90°, 45°, 10°, and 0, as indicated. The disk samples are in the $X$-$Y$ plane of the ($X$, $Y$, $Z$) laboratory frame shown in Fig. 2.4. The field **H** is in the $Y$-$Z$ plane and at an angle $\theta_H$ to the $Z$-axis. The linearly polarized microwave field **h**(t) is along $Y$.

In the experiment for the data in Figs. 6.11 and 6.13, the maximum $H$ value was 8.5 kOe. The data for S1 and S4 are shown for demonstration purposes to compare with the numerical results presented in Section 2.4 and to analyze the effect of the disk thickness. One can see that the data in Figs. 6.11-6.13 show some agreement with the results of the numerical $h_{crit}$ evaluations in Fig. 2.5(a). According to prediction from Section 2.4, when $\theta_H$ decreases, the meaningful butterfly curve range increases. There are also some unpredicted features. (1) The large peaks at low $H$ for small $\theta_H$ are not predicted by the theory. The low field peak is less pronounced for S1. (2) The minimum $h_{crit}$ is larger for very small $\theta_H$ of 0 and 5° than for other $\theta_H$ values. (3) There is a dip at $H \sim 11$ kOe for S2 and $\theta_H = 0$. The $\theta_H = 0$ value was not considered in the numerical calculations and this dip will be discussed later.

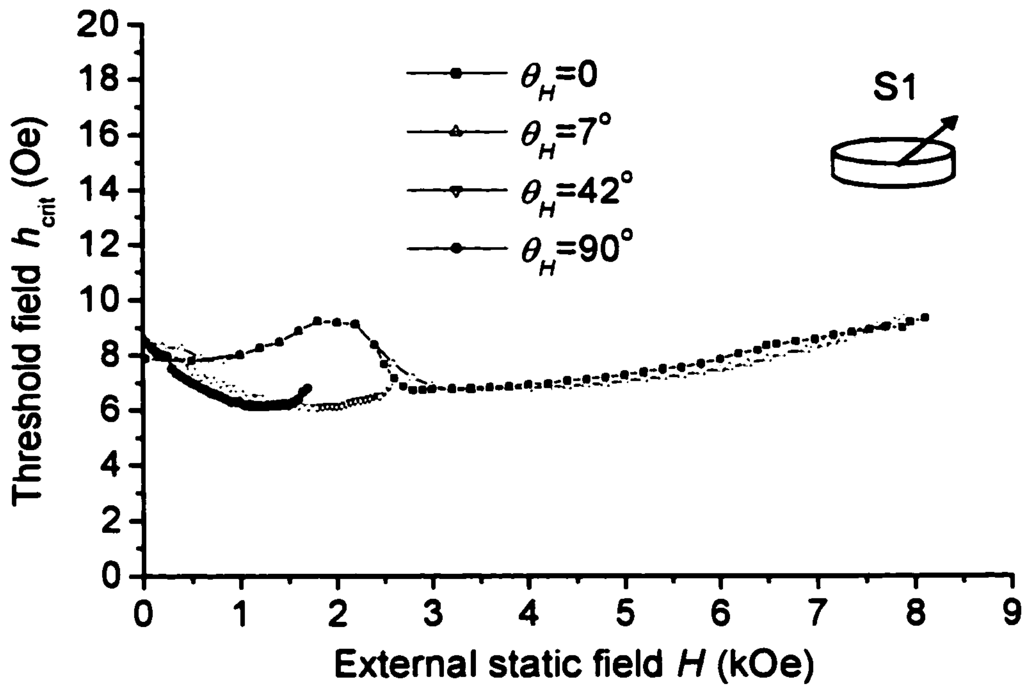


Figure 6.11. Out of plane oblique pumping threshold $h_{crit}$ as a function of the external static field $H$ for the Zn(Mn)-Y sample S1 with 16.7 GHz microwave excitation. The graphs show results for values of $\theta_H$, the field angle relative to the disk normal, as indicated. The microwave field $\mathbf{h}(t)$ is applied in-plane as shown in Fig. 2.4.

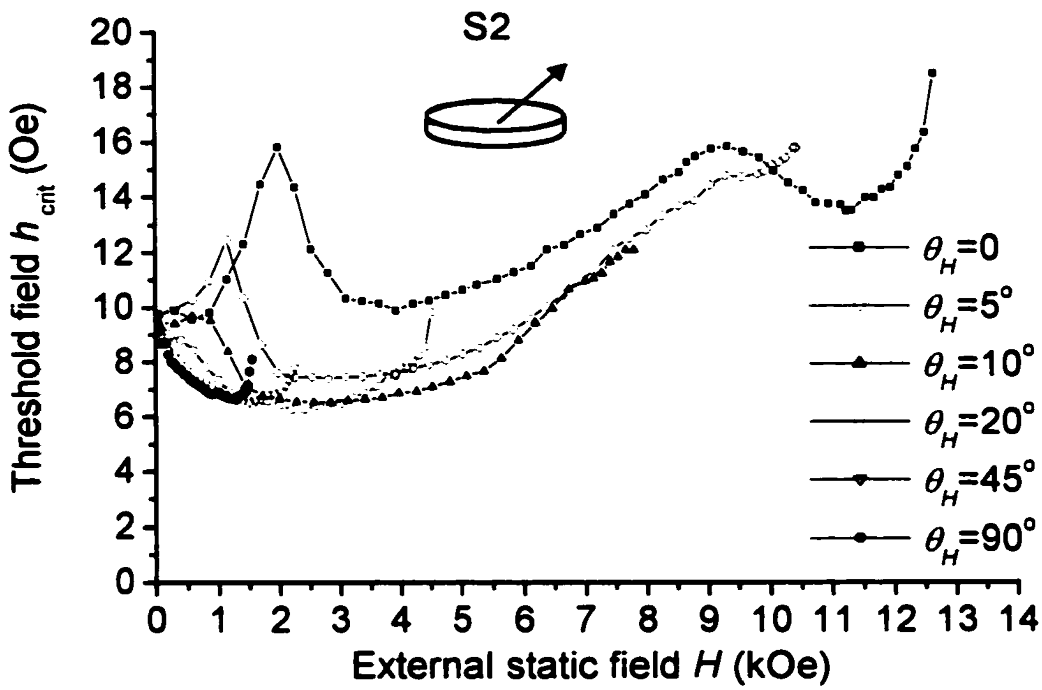


Figure 6.12. Out of plane oblique pumping threshold $h_{crit}$ as a function of the external static field $H$ for the Zn(Mn)-Y sample S2 with 16.7 GHz microwave excitation. The graphs show results for values of $\theta_H$, the field angle relative to the disk normal, as indicated. The microwave field $\mathbf{h}(t)$ is applied in-plane as shown in Fig. 2.4.

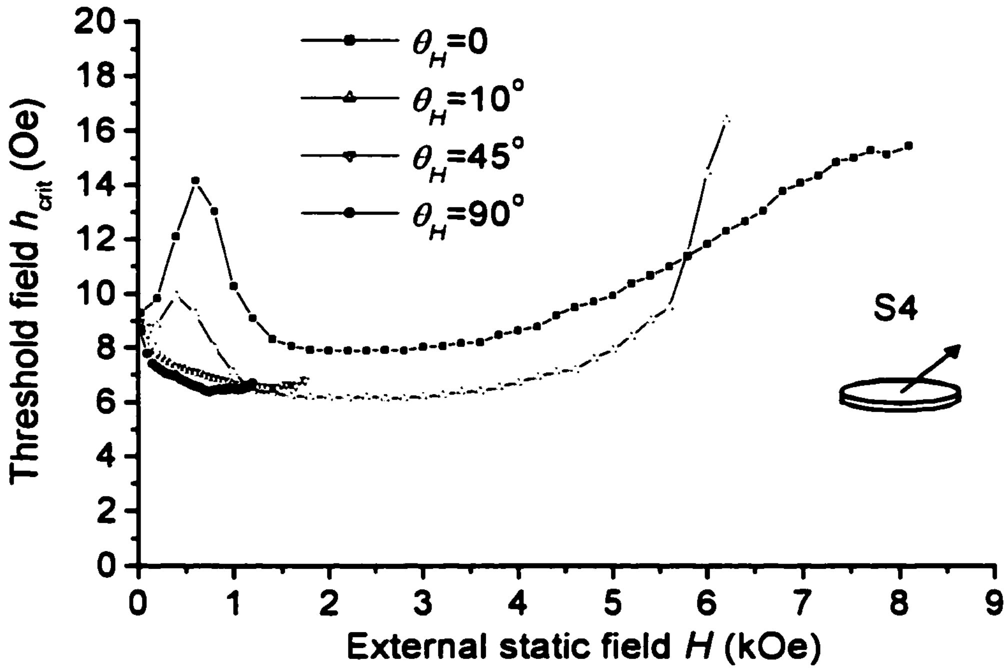


Figure 6.13. Out of plane oblique pumping threshold $h_{crit}$ as a function of the external static field $H$ for the Zn(Mn)-Y sample S4 with 16.7 GHz microwave excitation. The graphs show results for values of $\theta_H$, the field angle relative to the disk normal, as indicated. The microwave field $\mathbf{h}(t)$ is applied in-plane as shown in Fig. 2.4.

The $h_{crit}$ response at large $\theta_H$ values of 90° and 45° is determined by pumping which is close to parallel and the $k$–dependent spin wave linewidth discussed in Section 6.2. At small angles, when pumping becomes truly oblique, the $h_{crit}$ response shows large peaks at low fields for both samples. These peaks originate from the transition from unsaturated to saturated states. In the infinitely thin easy plane disk, the saturation field is close to zero for any $H$ direction. The real samples have nonzero saturation fields. The increase in sample thickness increases the saturation field. This effect can be seen in graphs. The peak is positioned at about 2 kOe for S1 and S2 and at about 700 Oe for S4.

The extensive experimental investigation and data analysis were performed for the S2 disk only. As shown in Fig. 6.12, $\theta_H$ is a very critical parameter for the butterfly curves, especially for $\theta_H$ below 20°. A 1-2° deviation from $\theta_H = 0$ may significantly change a butterfly curve. Note that in the experiment, the precision of the $H$ orientation was better than 1°, but the position of the sample with respect to a sample holder could deviate by up to 3°. This means that the $\theta_H = 0$ curve in Fig. 6.12 may correspond to an actual value of $\theta_H = 3°$. Therefore, adjustments in the numerical calculations were made to account for this possible error in $\theta_H$.

Figure 6.14 shows the spin wave instability threshold field $h_{crit}$ as a function of $H$ for out of plane oblique pumping in the Zn(Mn)-Y S2 disk at a pumping frequency of 16.7 GHz. The figure shows oblique pumping butterfly curve data for $\theta_H$ values of 90°, 20°, 10°, 5°, and 0, as indicated. The solid lines in the figure show the theoretical response from Eqs. (2.65)-(2.68) and the minimization procedure of Section 2.4, based on the parameters specified above for the Zn(Mn)-Y S2 disk and modified demagnetizing tensor components. The results of the numerical calculations are shown for $\theta_H$ values of

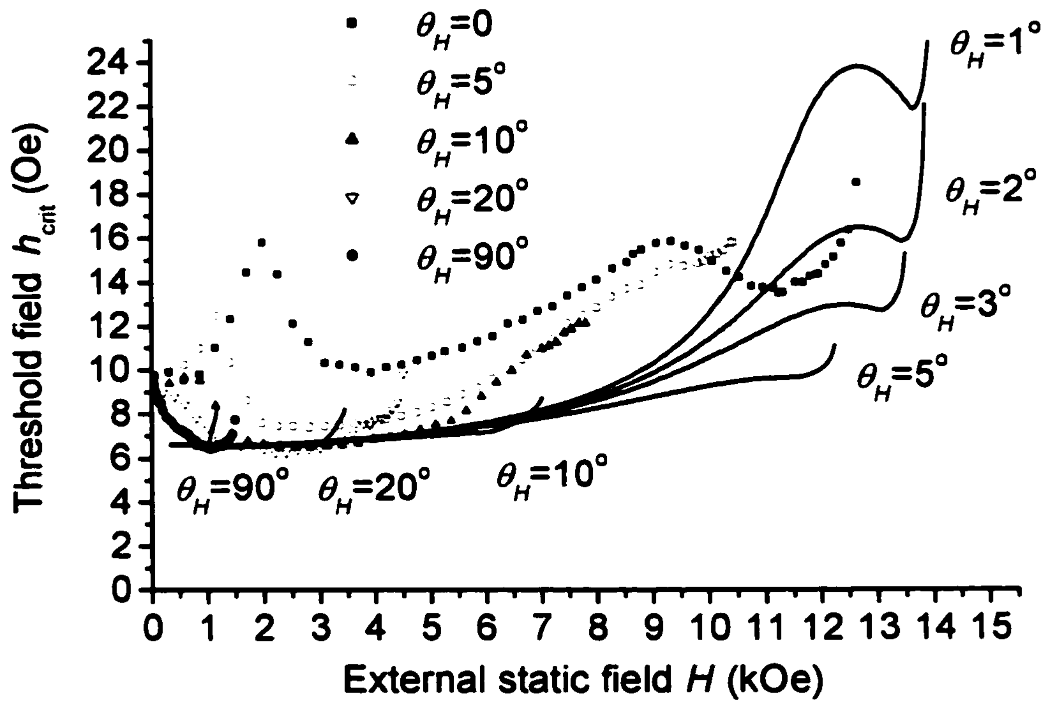


Figure 6.14. Out of plane oblique pumping threshold $h_{crit}$ as a function of the external static field $H$ for the Zn(Mn)-Y sample S2 with 16.7 GHz microwave excitation. The solid lines indicate results of numerical calculations. The graphs show the data for values of $\theta_H$, the field angle relative to the disk normal, as indicated. The spin wave linewidth $\Delta H_k$ was set to a constant value of 12.8 Oe for all calculated curves.

90°, 20°, 10°, 5°, 3°, 2°, and 1°, as indicated. The spin wave linewidth $\Delta H_k$ was set to a constant value of 12.8 Oe for all calculated curves.

One can see that the $h_{crit}$ response can be described by the theory reasonably well only for $\theta_H$ values greater than 20°. At $\theta_H$ = 10°, the theoretical curve terminates at smaller $H$ values than the data. However, at $\theta_H$ = 5°, the theoretical curve terminates at larger $H$ values than the data. One can see that at $\theta_H$ = 0 the data cannot be described by numerical calculations for any $\theta_H$ values in the range of 0 - 5°. Another important feature in Fig. 6.14 is the significant increase of the maximum experimental $h_{crit}$ for $\theta_H$ = 10° and $\theta_H$ = 5° compared to the calculated maximum $h_{crit}$. These apparent disagreements between the data and the theory cannot be explained by the error in $\theta_H$ only. More speculations are required to understand the $h_{crit}$ response for the out of plane oblique pumping.

Consider now the $h_{crit}$ data for $\theta_H$ = 0. First, the peak at $H \sim 2$ kOe is similar to the low field peak for $\theta_h$ = 90° in Fig. 6.10. Second, the minimum $h_{crit}$ is about 10 Oe, similar to the minimum $h_{crit}$ of about 8.5 Oe for $\theta_h$ = 90° in Fig. 6.10. The calculated minimum $h_{crit}$ is much smaller. Third, the observed dip at $H \sim 11$ kOe is also present in calculated curves for $\theta_H > 3°$. Fourth, a small error in $\theta_H$ is extremely critical for $\theta_H$ = 0. It is obvious that if the sample has an ideal disk shape and $\theta_H$ is exactly zero, at low $H$ the $\mathbf{M}_s$ will lie close to the disk plane and the $\mathbf{M}_s$ direction in the disk plane will be completely arbitrary!

This situation corresponds to an arbitrary angle $\theta_h$ for the in-plane oblique pumping $h_{crit}$ data in Fig. 6.10. In such a case the pumping angle $\theta_h$ in Fig. 6.10 may have any value in the range of 0 to 90°. The low $H$ similarity between the $h_{crit}$ data for $\theta_H = 0$ in Fig. 6.14 and $\theta_h = 90°$ in Fig. 6.10 suggests that the disk was slightly rotated along the $Y$ axis, which is shown in Fig. 2.4. This rotation comes from the alignment difficulties in the experiment and is assumed to be less than 3°. Note that this deviation does not change the static field geometry of the problem except for slight deviation in $\theta_H$. The deviation from the pumping configuration in Fig. 2.4 only changes the direction of $\mathbf{h}$ in the disk plane while $\mathbf{h}$ is still in-plane. This change can be taken into account by modification in the microwave field orientation with respect to $H$.

This modification is demonstrated in Fig. 6.15 for the representative case of $\theta_H = 3°$ and $\varphi_h$ values of 0, 45°, 75°, and 90°, as indicated. The case $\theta_H = 3°$ and $\varphi_h = 0$ corresponds to the calculated curve in Fig. 6.14 for $\theta_H = 3°$. One can see that the adjustment in $\varphi_h$ can account for the increase in the minimum $h_{crit}$ with the $\theta_H$ decrease.

Another discrepancy between the data and calculations in Fig. 6.14 is related to the termination field $H_{cut}$ where an $h_{crit}$ butterfly curve terminates. As discussed in Chapter 2, $H_{cut}$ is determined exclusively by the spin wave dispersion and is independent of the direction of the microwave field or pumping configuration. One may change some material parameters to match the calculated $H_{cut}$ with the data but this way is non-physical and does not have any grounds. The extensive numerical calculations made that investigated possible changes in the pumping configuration were performed. The variable parameters were the field angle $\theta_H$ and the microwave field azimuthal angle $\varphi_h$, which is the angle in the $X$-$Y$ plane between the $Y$ axis and $\mathbf{h}$ in Fig. 2.4. In the case of the in-plane oblique pumping, the angle $\varphi_h$ is

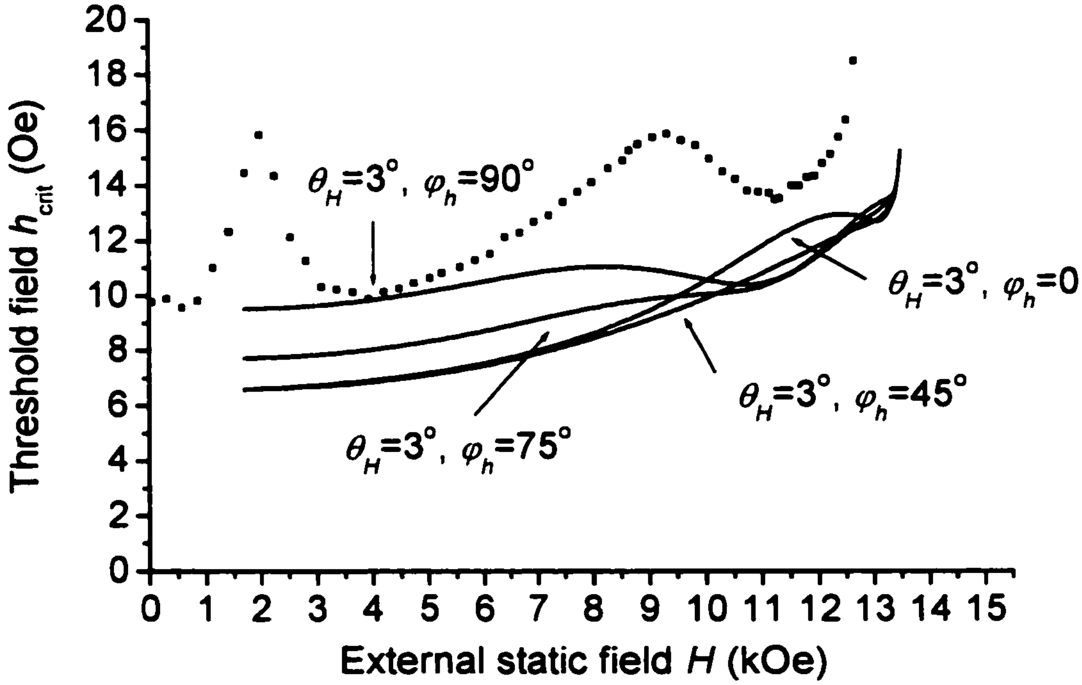


Figure 6.15. Out of plane oblique pumping threshold $h_{crit}$ as a function of the external static field $H$ for the Zn(Mn)-Y sample S2 with 16.7 GHz microwave excitation. The closed squares show the data for $\theta_H = 0$, the field angle relative to the disk normal. Solid lines indicate results of numerical calculations for $\theta_H = 3°$ and $\varphi_h$ values of 0, 45°, 75°, and 90°, as indicated. The spin wave linewidth $\Delta H_k$ was set to a constant value of 12.8 Oe for all calculated curves.

the same as $\theta_h$ in Fig. 6.10. First, the $\varphi_h$ value was chosen so that the solid line goes through the minimum $h_{crit}$ data in Fig. 6.14, as it is demonstrated in Fig. 6.15. Second, the $\theta_H$ value was chosen to provide the best $H_{cut}$ fit and keep all features of the $h_{crit}$ data curve.

Figure 6.16 shows the $h_{crit}$ data from Fig. 6.12 for the $\theta_H$ values of 20°, 10°, 5°, and 0. The solid lines indicate the results of numerical calculations where $\theta_H$ and $\varphi_h$ were fit parameters. The $\theta_H$ and $\varphi_h$ values indicated in the figure provide the best possible fit. The spin wave linewidth $\Delta H_k$ was set to a constant value of 12.8 Oe for all four calculated curves. The $h_{crit}$ data for $\theta_H = 20°$ and the corresponding fit for $\theta_H = 19°$ and $\varphi_h = 30°$ slightly differ from the observed trend for other curves. This deviation is caused by the relatively large $\theta_H$ value. In this case, the $h_{crit}$ data have similar features to the $h_{crit}$ data for the $\theta_H = 90°$ parallel pumping case. This particular $\theta_H = 20°$ case will be dismissed from the further analysis because it is affected by inhomogeneous demagnetizing fields discussed for parallel pumping.

The important feature of the data for $\theta_H$ values of 10°, 5°, and 0 and corresponding fitting curves is that the fitting $\theta_H$ values do not differ much from the experimental $\theta_H$ values. The maximum deviation is 3° for $\theta_H = 0$. This is in agreement with the above estimates of the experimental $\theta_H$ error. The fitted $\varphi_h = 90°$ value for this case suggests that the error came from the deviation of the disk plane from the vertical plane. The $H$ rotation plane is a horizontal plane and if the disk is not strictly in a vertical plane then an exact $\theta_H = 0$ case is impossible. The calculated fitted $\theta_H$ and $\varphi_h$ values in Fig. 6.16 agree with this scenario.

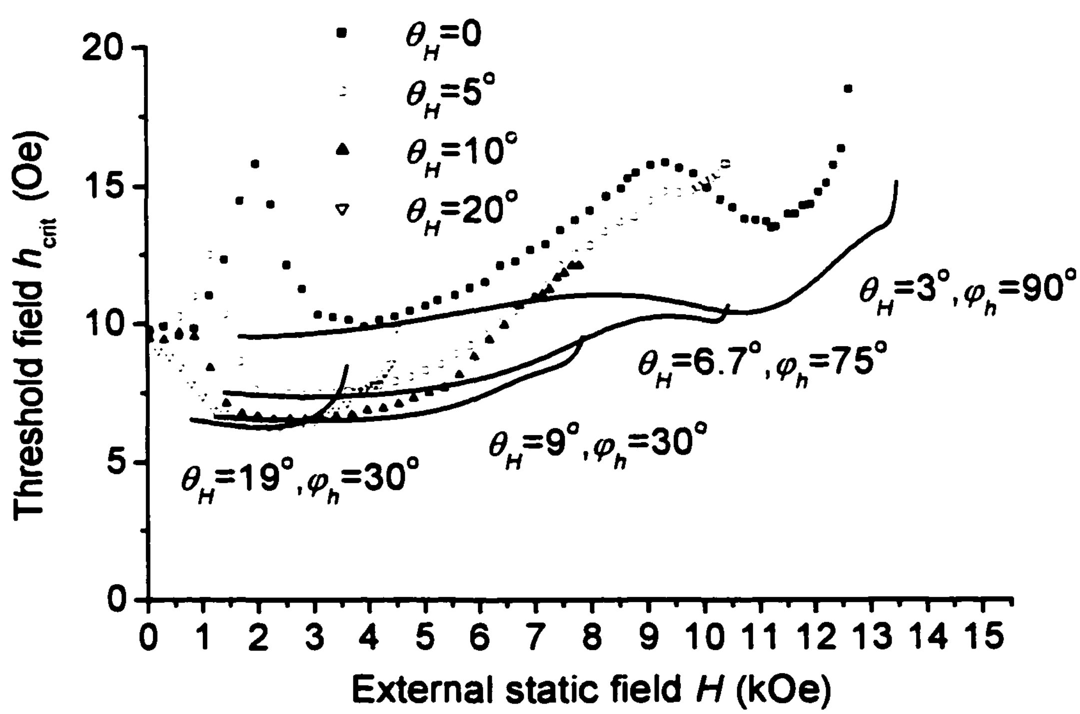


Figure 6.16. Out of plane oblique pumping threshold $h_{crit}$ as a function of the external static field $H$ for the Zn(Mn)-Y sample S2 with 16.7 GHz microwave excitation. The graphs show results for values of $\theta_H$, the field angle relative to the disk normal, as indicated. Solid lines indicate results of numerical calculations with fitting parameters $\theta_H$ and $\varphi_h$, as indicated. The spin wave linewidth $\Delta H_k$ was set to a constant value of 12.8 Oe for all calculated curves.

Another important feature of Fig. 6.16 is the deviation between the data and the calculated $h_{crit}$. The deviation increases with the $H$ increase. This implies that $\Delta H_k$ increases with an increase in $H$ and consequently with an increase in angle $\theta_M$ between the disk normal and $\mathbf{M}_s$. There are two possible mechanisms responsible for such increase. First is the dependence of $\Delta H_k$ on the spin wave propagation direction. This mechanism is unlikely because the discussion for Fig. 6.10 suggests that $\Delta H_k$ is independent of the spin wave propagation direction. The second mechanism is the influence of "magnetic stress" which occurs when $\mathbf{M}_s$ is tipped out of the disk plane. The smaller $\theta_M$ values cause more "magnetic stress". This magnetic stress may increase $\Delta H_k$.

The dependence of $\Delta H_k$ on $k$ should also be considered. Figure 2.5 shows that for all $\theta_H$ values, the $k$ values are in the same range. The parallel pumping data in Fig. 6.4(b) for the S2 sample show relatively small dependence of $\Delta H_k$ on $k$. Moreover, critical mode numerical calculations showed that $k$ become zero at $H_c \sim 5.5$ kOe for $\theta_H = 3°$ and $\varphi_h = 90°$, $H_c \sim 2.2$ kOe for $\theta_H = 6.7°$ and $\varphi_h = 75°$, and $H_c \sim 2.9$ kOe for $\theta_H = 9°$ and $\varphi_h = 30°$. One can see in Fig. 6.16 that below these fields, the data agree well with the theory. Therefore, the dependence of $\Delta H_k$ on $k$ will be excluded from the analysis and in the analysis wave numbers will be assumed to be close to zero as for the data in Fig. 6.10 for $\theta_h > 25°$. This assumption is valid for $H$ larger than the $H_c$ values specified above.

The $\Delta H_k$ response was calculated for each experimental $H$ value so that the calculated $h_{crit}$ curve matched the $h_{crit}$ data in Fig. 6.16. The approach is the same as described in Section 3.4, except that the $\Delta H_k$ response will be a function of $H$. In the minimization procedure, $\Delta H_k$ was assumed to be independent of the spin wave parameters in this first approximation.

Figure 6.17 shows the calculated $\Delta H_k$ vs. $H$ response for the out of plane oblique pumping data of Fig. 6.16. The calculations were done for fitting parameters $\theta_H = 3°, \varphi_h = 90°$ for the experimental $\theta_H = 0$ curve, $\theta_H = 6.7°, \varphi_h = 75°$ for the experimental $\theta_H = 5°$ curve, and $\theta_H = 9°, \varphi_h = 30°$ for the experimental $\theta_H = 10°$ curve. The $\Delta H_k$ response at low fields is determined by demagnetizing effects that are discussed above. At the termination points $H_{\text{cut}}$, the $\Delta H_k$ response is erroneous due to the misfit between the experiment and the theory. For $\theta_H = 3°$ and $\varphi_h = 90°$, this misfit results in a high field peak and a dip that are also present in the $h_{\text{crit}}$ data in Fig. 6.16. These high field features will also be excluded from the analysis. Besides low and high field regions, the $\Delta H_k$ response is similar for all three curves.

Along with the $\Delta H_k$ response, critical mode polar $\theta_k$ and azimuthal $\varphi_k$ angles and static magnetization equilibrium polar angle $\theta_M$ were calculated for each data point. As discussed above, the calculated wave number $k$ was zero. The results of these calculations are shown in Fig. 6.18. Graph (a) shows the polar spin wave propagation angle $\theta_k$ vs. $H$. Graph (b) shows the azimuthal spin wave propagation angle $\varphi_k$ vs. $H$. Graph (c) shows the static magnetization equilibrium polar angle $\theta_M$ vs. $H$. The graphs show results for values of $\theta_H$ and $\varphi_h$, the same as in Fig. 6.16, as indicated. The purpose of these graphs, along with Fig. 6.17, is to examine the $\Delta H_k$ response as a function of the critical mode angles and $\theta_M$.

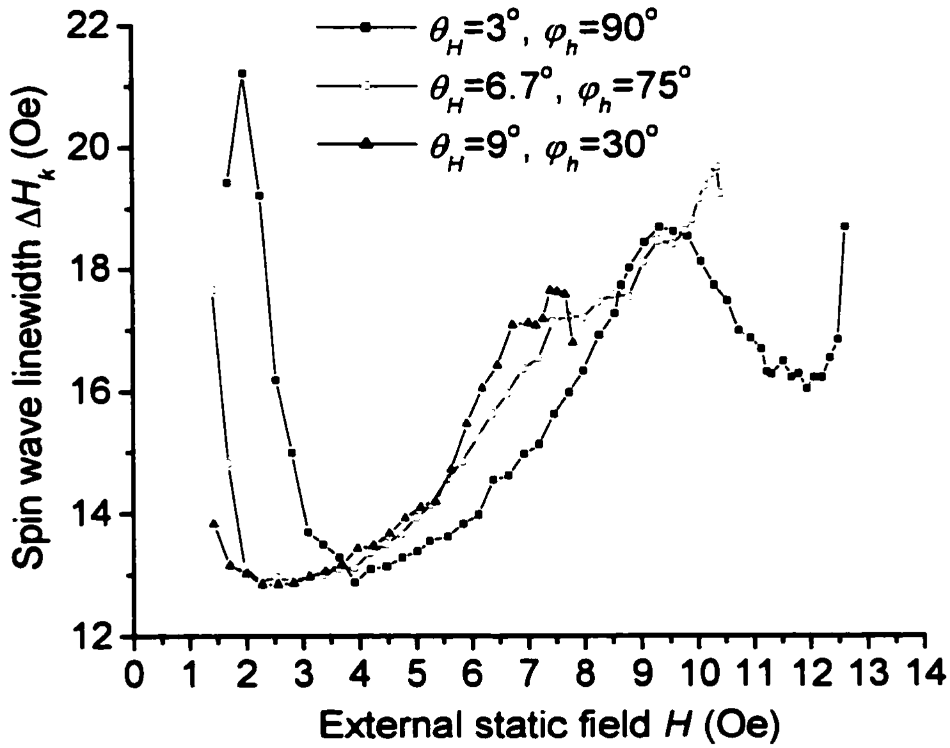


Figure 6.17. The calculated $\Delta H_k$ vs. $H$ response for the out of plane oblique pumping in for the Zn(Mn)-Y sample S2 with 16.7 GHz microwave excitation. The graphs show results for values of $\theta_H$ and $\varphi_h$, the same as in Fig. 6.16, as indicated.

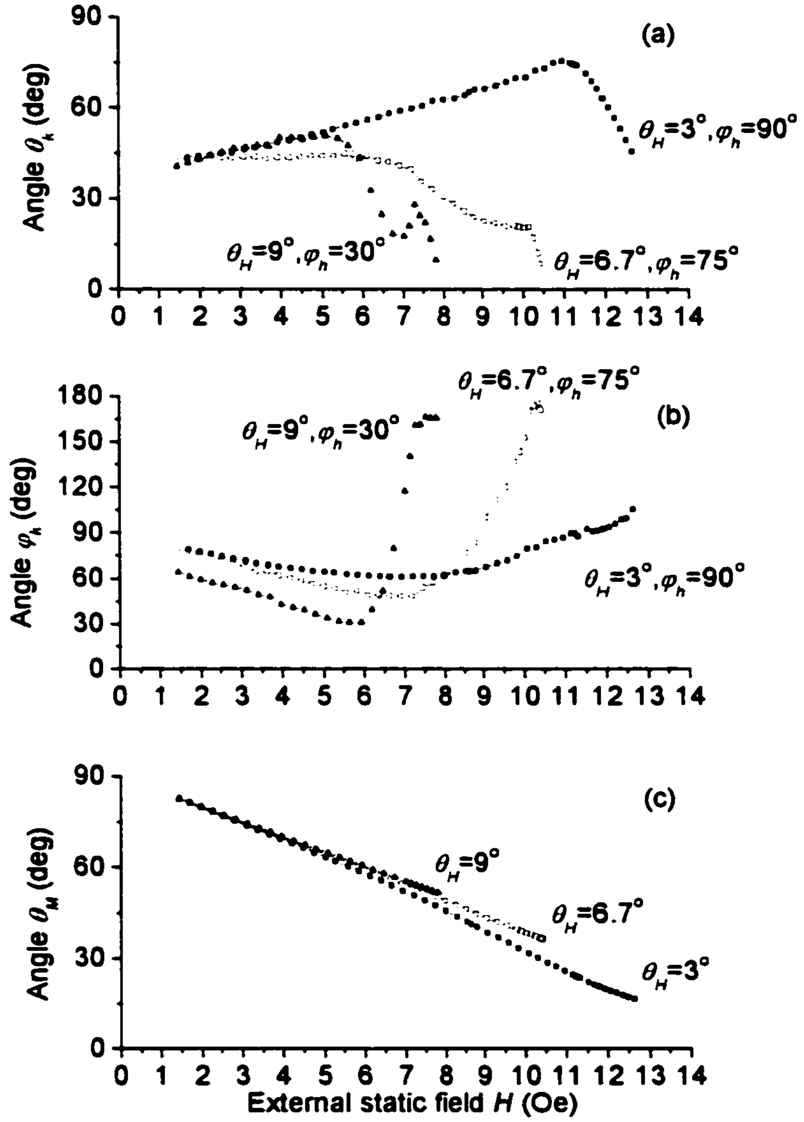


Figure 6.18. The results of numerical calculations for the out of plane oblique pumping data in Fig. 6.13. Zn(Mn)-Y sample S2 with 16.7 GHz microwave excitation. The graphs show (a) polar spin wave propagation angle $\theta_k$ vs. $H$, (b) azimuthal spin wave propagation angle $\varphi_k$ vs. $H$, and (c) static magnetization equilibrium polar angle $\theta_M$ vs. $H$. The graphs show results for values of $\theta_H$ and $\varphi_h$, the same as in Fig. 6.16, as indicated.

Graphs (a) and (b) demonstrate that there is no apparent correlation between $\Delta H_k$ and any of the critical mode angles $\theta_k$ and $\varphi_k$. The $\theta_k$ and $\varphi_k$ response is a result of the complicated oblique pumping configuration. Therefore, the possible correlation between $\Delta H_k$ and spin wave propagation direction may be related only to the propagation direction with respect to a hard crystallographic $c$ axis (Gurevich *et al.* [1999]). Graph (c) shows the possible correlation between $\Delta H_k$ and $\theta_M$.

As discussed above, there are two possible mechanisms that are responsible for the $\Delta H_k$ increase as $H$ increases. These mechanisms are the dependence of $\Delta H_k$ on the spin wave propagation direction and the influence of "magnetic stress" which occurs when $\mathbf{M}_s$ is tipped out of the disk plane.

The first mechanism should be related to the spin wave propagation direction with respect to a hard axis. This direction can be calculated from the $\theta_k$, $\varphi_k$, and $\theta_M$ values. The angle $\beta$ between $\mathbf{k}$ and the hard $Z$-axis in Fig. 2.4 is given by the relation (Arfken and Weber [1995])

$$\cos\beta = \sin\theta_M \sin\theta_k \cos\varphi_k + \cos\theta_M \cos\theta_k\,. \tag{6.6}$$

In order to investigate the first mechanism, the $\Delta H_k$ response should be examined as a function of $\beta$. Calculations show that there is no reasonable dependence of $\Delta H_k$ on $\beta$, the results are chaotic, and this mechanism can be dismissed.

In order to investigate the second "magnetic stress" mechanism, the $\Delta H_k$ response should be examined as a function of $\theta_M$ which is a measure of "magnetic stress". Figure 6.19 shows the $\Delta H_k$ vs. $\theta_M$ response for values of $\theta_H$ and $\varphi_h$, the same as in Fig. 6.16, as indicated. The solid line indicates the fit to the data. The fitting formula is given by

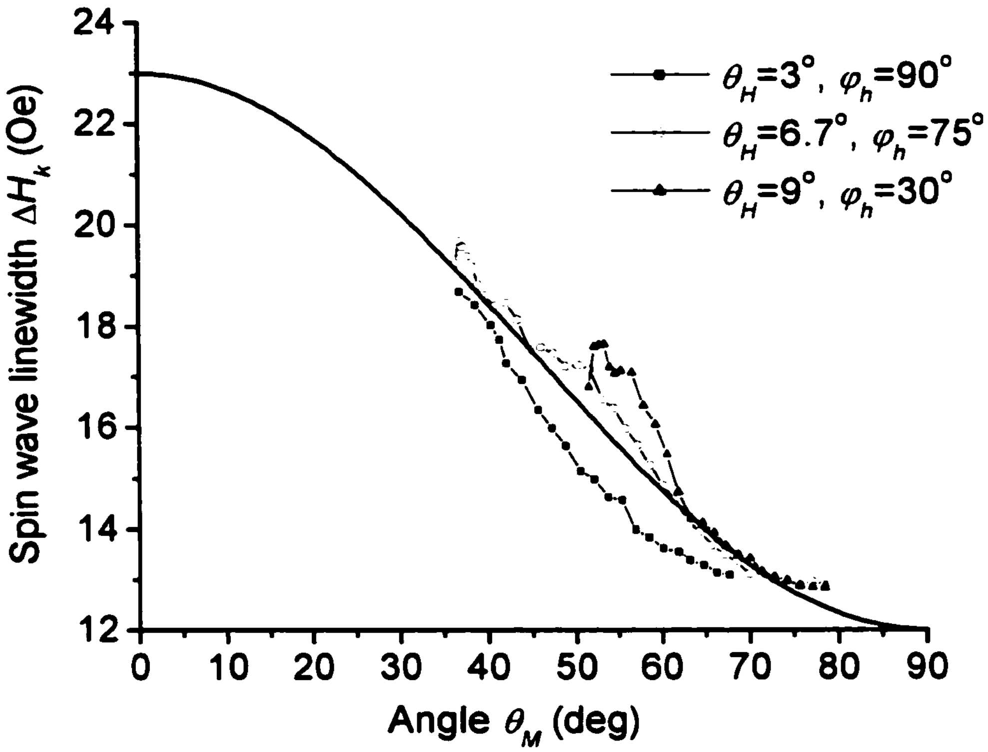


Figure 6.19. The calculated $\Delta H_k$ vs. the static magnetization equilibrium polar angle $\theta_M$ for the out of plane oblique pumping in the Zn(Mn)-Y sample S2 with 16.7 GHz microwave excitation. The graphs show results for values of $\theta_H$ and $\varphi_h$, the same as in Fig. 6.16, as indicated. The solid line indicates the fit to the data.

$$\Delta H_k = \Delta H_{k=0} + C_M \cos^2 \theta_M, \tag{6.7}$$

where $\Delta H_{k=0}$ is 12 Oe and $C_M$ is 11 Oe.

Equation (6.7) represents the best physically justified fit to the data in Fig. 6.19. At low fields, where the demagnetizing effects increase $h_{crit}$, the actual $\theta_M$ value may be 90°. This value implies that $\mathbf{M}_s$ is still in-plane. The quadratic cosine dependence is typical for anisotropic effects. The $\Delta H_k$ data in Fig. 6.19 represent the first observation of the "magnetic stress" effect which increases spin wave linewidth. The effect is big. The $C_M$ parameter determines the magnitude of this effect and it is comparable to $\Delta H_{k=0}$. This effect has not been predicted. A similar effect was observed for the FMR linewidth $\Delta H_0$ in Zn-Y at 9.5 GHz when $H$ is rotated out of plane (Hurben [1996]). The origin of the magnetic stress effect is currently unknown but the results may provide an additional insight to understand the mechanism of large loss in hexagonal ferrites.

The results of this chapter show important contrasts between the high power response in ferrites with small and large magnetocrystalline anisotropy. The parallel pumping 9 GHz data show the important sample size effect which made the oblique pumping investigation at this frequency impossible. The parallel pumping 16.7 GHz data show (1) an almost textbook $h_{crit}$ vs. $H$ response, (2) no significant effect of sample size or thickness, and (3) a $\Delta H_k$ vs. $k$ response which matches previous data for Zn-Y. The in-plane oblique pumping 16.7 GHz data show (1) the influence of the demagnetizing effects on the uniform precession and butterfly curves, (2) the good agreement between the uniform mode theory and the uniform mode response, and (3) the absence of the dependence of $\Delta H_k$ on the spin wave propagation direction. The out of plane oblique pumping 16.7 GHz data show (1) the sensitivity of the results to the orientation of the disk sample and $H$, (2) the qualitative agreement between the data and the numerical calculations that take into account the $\theta_H$ and $\varphi_h$ deviation from the experimental values, and (3) the $\Delta H_k$ dependence on the magnetic stress caused by the $\mathbf{M}_s$ deviation from the easy plane.

These conclusions represent the main results of the spin wave instability investigation in Zn-Y ferrite materials. They will be developed and discussed in the next chapter along with the proposed future work.

# CHAPTER 7

# SUMMARY

The objective of the dissertation was the investigation of the spin wave instability processes in anisotropic ferrites. The first part considered the development of the general spin wave instability theory. The formalism includes provision for a magnetic insulator of ellipsoidal shape, with a general free energy based magnetic anisotropy, and subject to a general microwave field configuration. The second part presented the results of the experimental investigation of the spin wave instability processes in the ferrite materials of current technological interest and the analysis of these results based on the developed theory.

Section 7.1 presents a brief summary of the topics and conclusions of all previous chapters. Section 7.2 discusses possible directions for the future work in the area of microwave magnetic materials.

## 7.1. Summary and Conclusion

The classical theory of spin wave instability in ferromagnetic insulators has been extended in Chapter 2 to include general anisotropy based on a tensor formulation of static and dynamic effective fields. The theory provides working equations for threshold calculations and critical mode determinations. The formulation is completely general and can accommodate any type of anisotropy and an arbitrary microwave field configuration. The sample shape is limited to that of a general ellipsoid in order to maintain a uniform magnetization and uniform internal static and microwave fields. The formalism includes the ability to include a general wave vector dependent spin wave relaxation rate or linewidth. As an example application, the formalism was applied to first order processes in an easy plane ferrite disk with parameters applicable to Zn-Y hexagonal ferrite with an in plane 17 GHz microwave pump field.

Chapter 3 described the operation of the high power microwave spectrometer which was built to investigate spin wave instability threshold fields in ferrites at microwave frequencies. The unique feature of this spectrometer is the operation at two frequencies of 9 and 16.7 GHz. This feature significantly increased measurement capabilities and resolved experimental problems for oblique pumping in Zn-Y hexagonal ferrite. High power microwave properties of three ferrite magnetic materials were investigated with the spectrometer.

Chapter 4 analyzed high power microwave properties of LPE YIG (110) oriented thin films which showed classical butterfly curves with low values of the spin wave linewidth. The analysis of the data showed that, for an in-plane magnetized film, thin film geometry forces spin waves to propagate in the film plane. The small magnetocrystalline anisotropy affects the spin wave instability threshold and shifts the butterfly curve kink point for different in-plane directions of the applied field. The data qualitatively agree with the results of the theoretical predictions in Chapter 2. The most important result is that the spin wave linewidth in single crystal YIG does not depend on the spin wave propagation direction with respect to the crystallographic axes.

The results of Chapter 5 for hipped polycrystalline YIG showed that dipole-dipole narrowing works for the uniform precession of magnetization and does not work for spin waves. The FMR linewidth data give the all time low linewidth for pure polycrystalline YIG of 13 Oe at X-band. This value agrees with the value predicted in Schlömann's [1958] theory of dipole narrowed anisotropy line broadening in large grain size YIG. The theory is also in excellent agreement with the measured $\Delta H_0$ frequency dependence. The high power microwave characterization at 9 and 16.7 GHz demonstrated that (1) the intrinsic microwave loss in hipped polycrystalline YIG can be similar to loss in single crystal YIG, (2) the spin wave linewidth is determined by the grain size, and (3) the transit time model needs more examination. The parallel pumping experiment can be an important tool of ferrite materials characterization on a micron and submicron scale as well as the intrinsic microwave loss characterization.

Chapter 6 presented the results of the spin wave instability investigation in easy plane Zn-Y hexagonal ferrite plates with large magnetocrystalline anisotropy. The parallel pumping measurements were performed at 9 and 16.7 GHz. At 9 GHz, the sample size effect was found, so that the threshold field value depended on the lateral sample size. The 16.7 GHz data show (1) an almost textbook $h_{crit}$ versus $H$ response, (2) no significant effect of sample size or thickness, and (3) a $\Delta H_k$ versus $k$ response which matches previous data for Zn-Y.

The investigation of oblique pumping which utilizes the full power of the general spin wave instability theory of Chapter 2 was performed at 16.7 GHz. The data analysis was performed for oblique pumping and the theoretical model was consistent with the data. The most important results are (1) the qualitative agreement between the theory of the spin wave instability and the data, (2) the independence of the spin wave linewidth in single crystal Zn(Mn)-Y on the spin wave propagation direction with respect to the hard $c$ axis, and (3) the discovery of the "magnetic stress" effect. The magnetic stress effect increases spin wave linewidth and the quantitative increase of 11 Oe is comparable to the minimum spin wave linewidth of 12.8 Oe. The $k$-dependent spin wave linewidth contribution is much smaller. The magnetic stress effect may point out the mechanisms for large intrinsic values of microwave loss in hexagonal ferrites.

### 7.2. Future Work

As a conclusion, the classical spin wave instability theory in ferromagnetic insulators has been extended to include general anisotropy based on a tensor formulation of static and dynamic effective fields. The theory provides working equations for threshold calculations and critical mode determinations. The theory was successfully applied to the analysis of the obtained comprehensive experimental data on anisotropic ferrite materials for various static and microwave field configurations. It was found that the spin wave linewidth in general is independent of the spin wave propagation direction, but it can increase if the magnetization is pulled out of the easy crystallographic plane.

The future work related to this thesis can be divided in two categories. The first category is the future work which is a consequence of the theoretical developments and experiments on the materials reported in this thesis. The second category is the future work on new materials related to the high power microwave spectrometer.

The parallel pumping results for LPE YIG thin films demonstrated that the bulk exchange spin wave approximation is applicable. This can lead to the oblique pumping experiments on these films, similar to the work on Zn-Y discussed in Chapter 6. The theoretical developments in Chapter 2 provide a sufficient theoretical background for this investigation. It will be interesting to verify the presence of the magnetic stress effect in obliquely magnetized YIG films.

Another interesting problem would be an investigation of the sample size influence on the threshold field. As shown in Chapter 5, the decrease in the grain size increases the threshold. One can visualize an experiment where a thin YIG film is etched into micron parts so that the effect of the grain size can be modeled precisely. This experiment could answer an old question about the minimum wave number of the excited spin waves and also verify the transit time model. A similar sample size effect was discussed in Section 6.2 for Zn-Y at 9 GHz. The presented experimental work considered only first-order spin wave instability processes. The second-order resonance saturation experiments on hipped YIG are also of interest. The second-order experiments were performed on Zn-Y by Cox *et al.* [2001].

The parallel pumping data in Chapter 6 for Zn-Y showed the influence of the inhomogeneous demagnetizing fields. One of the future goals is a parallel pumping investigation in a uniformly magnetized sample such as a sphere. This will require fabrication of a high quality Zn-Y sphere and x-ray orientation of the sphere. It is also interesting to investigate magnetostatic wave propagation in single crystal Zn-Y thin slabs and determine the magnetostatic wave spectra (Dorsey *et al.* [1990]) as for YIG thin films (Scott [2002]).

The future work for Zn-Y is mostly related to the theoretical investigation of the microwave loss mechanisms and the origin of the magnetic stress effect. The increase of damping if the magnetization is pulled out of the easy crystallographic plane was also observed for the FMR linewidth in Zn-Y (Hurben [1996]). It is also useful to calculate the exchange parameter and find its anisotropy. Brillouin light scattering experiments can help to visualize the excited critical modes in Zn-Y as has been done in YIG (Kabos *et al.* [1997]). The interesting problem is the fact that parallel pumping spin wave linewidth in pure Zn-Y is not affected by eddy current losses. One can also make oriented polycrystalline easy plane ferrite Zn-Y and investigate its high power microwave properties.

The high power microwave spectrometer can be used to measure thresholds in other types of magnetic materials than those investigated in this work. It is also useful to add a low temperature capability for the spin wave instability threshold measurements (Gurevich *et al.* [1999]). The interesting work would be a theoretical and experimental investigation of the first and second order spin wave instability processes in M-type hexagonal ferrites with large easy axis anisotropy (Lebedev *et al.* [2002]), but this would require a high power microwave spectrometer operating at frequencies above 60 GHz. Other materials are permalloy-type films where large conductivity and magnetization make a big difference. The spin wave instability processes in permalloy films received a limited attention (Berteaud and Pascard [1966]). The microwave loss mechanisms have not been understood completely (Kambersky and Patton [1975]) and the microwave properties of these materials are very important for the magnetic recording industry.

# REFERENCES


1. J. D. Adam, M. R. Daniel, P. R. Emtage, and S. H. Talisa, *Thin Films for Advanced Electronic Devices*, edited by M. H. Francombe and J. L. Vossen, Academic Press, Boston, 1991.
2. P. W. Anderson and H. Suhl, Phys. Rev. **100**, No. 6, 1788 (1955).
3. G. B. Arfken and H. J. Weber, *Mathematical Methods for Physicists*, fourth edition, Academic Press, New York, 1995.
4. A. J. Berteaud and H. Pascard, J. Appl. Phys. **37**, No. 5, 2035 (1966).
5. N. Bloembergen and R. W. Damon, Phys. Rev. **85** No. 4, 699 (1952).
6. N. Bloembergen and S. Wang, Phys. Rev. **93** No. 1, 72 (1954).
7. R. G. Cox, C. E. Patton, M. A. Wittenauer, P. Kabos, and L. Chen, J. Appl. Phys. **89**, No. 8, 4454 (2001).
8. R. G. Cox, unpublished work (2002).
9. S. Dixon, A. Tauber, R. O. Savage, J. Appl. Phys. **36**, No. 3, 1018 (1965).
10. S. Dixon, IEEE Trans. Magn. **14**, No. 1, 28 (1978).
11. P. Dorsey, K. Sun, C. Vittoria, M. A. Wittenauer, F. J. Friedlander, and A. Schindler, J. Appl. Phys. **67**, No. 9, 5524 (1990).
12. J. J. Green and B. J. Healy, J. Appl. Phys. **34**, No. 4, 1285 (1963).
13. J. J. Green and T. Kohane, SCP and Sol. State Tech. **7**, No. **8**, 46 (1964).
14. J. J. Green, C. E. Patton, and E. Stern, J. Appl. Phys. **40**, No. 1, 172 (1969).

15. J. H. E. Griffiths, Nature **158**, No. 4019, 670 (1946).

16. A. G. Gurevich and G. A. Melkov, *Magnetic Oscillations and Waves*, CRC Press, New York, 1996.

17. A. G. Gurevich, A. V. Nazarov, O. A. Chivileva, and V. V. Petrov, Phys. Solid State **41**, No. 9, 1513 (1999).

18. W. Haubenreisser, T. Klupsch, and F. Voigt, Phys. Stat. Sol. (b) **73**, 11 (1976).

19. J. Helszajn and J. McStay, IEEE Trans. Microwave Theory Tech. **MTT-18**, No. 9, 518 (1970).

20. J. Helszajn and J. McStay, IEEE Trans. Microwave Theory Tech. **MTT-20**, No. 7, 437 (1972).

21. M. J. Hurben, Ph. D. dissertation, Colorado State University, Fort Collins, Colorado (1996).

22. M. J. Hurben, D. R. Franklin, and C. E. Patton, J. Appl. Phys. **81**, No. 11, 7458 (1997).

23. M. J. Hurben and C. E. Patton, J. Appl. Phys. **83**, No. 8, 4344 (1998).

24. J. D. Jackson, *Classical Electrodynamics*, John Wiley & Sons, New York, 1998.

25. P. Kabos, M. Mendik, G. Wiese, and C. E. Patton, Phys. Rev. B **55**, No. 17, 11457 (1997).

26. B. A. Kalinikos, N. G. Kovshikov, and N. V. Kozhus', Sov. Phys. Solid State **27**, No. 9, 1681 (1985).

27. B. A. Kalinikos, M. P. Kostylev, N. V. Kozhus', and A. N. Slavin, J. Phys.: Condens. Matter **2**, 9861 (1990).

28. V. Kambersky and C. E. Patton, Phys. Rev. B **11**, No. 7, 2668 (1975).

29. A. Kasami and S. Koide, J. Phys. Soc. Japan **21**, 552, (1966).

30. T. Kasuya and R. C. Le Craw, Phys. Rev. Lett. **6**, No. 5, 223 (1961).

31. C. Kittel, Phys. Rev. **73**, No. 2, 155 (1948).

32. L. Landau and E. Lifshitz, Phys. Z. Sowjetunion **8**, 153 (1935).

33. B. Lax and K. J. Button, *Microwave Ferrites and Ferrimagnetics*, McGraw-Hill, New York, 1962.

34. S. V. Lebedev, C. E. Patton, M. A. Wittenauer, L. V. Saraf, and R. Ramesh, J. Appl. Phys. **91**, No. 7, 4426 (2002).

35. R. C. Le Craw and E. G. Spencer, J. Phys. Soc. Japan **17**, Suppl., No. B1, 401, (1962).

36. Y. H. Liu and C. E. Patton, J. Appl. Phys. **53**, No. 7, 5116 (1982).

37. M. Marysko, K. Nitsch, P. Novak, D. Menard, A.V. Nazarov, Y. Y. Song, C. E. Patton, M. Kucera, and H. Stepankova, presented at the 46$^{th}$ MMM Conference, CG-09, 2001, Seattle, Washington.

38. K. D. McKinstry, C. E. Patton, and M. Kogekar, J. Appl. Phys. **58**, No. 2, 925 (1985).

39. K. D. McKinstry and C. E. Patton, Rev. Sci. Instrum. **60**, No. 3, 439 (1989).

40. K. D. McKinstry, Ph. D. dissertation, Colorado State University, Fort Collins, Colorado (1991).

41. G. A. Melkov, Sov. Phys. JETP **43**, No. 4, 690 (1976).

42. M. Mita and H. Shimizu, J. Phys. Soc. Japan **35**, No. 2, 414, (1973).

43. M. Mita and H. Shimizu, AIP Conf. Proc. **24**, 514, (1975).

44. A. V. Nazarov, R. G. Cox, and C. E. Patton, IEEE Trans. Magn. **37**, No. 4, 2380 (2001).

45. A. V. Nazarov, C. E. Patton, R. G. Cox, L. Chen, and P. Kabos, J. Magn. Magn. Mater. **248**, No. 2, 164 (2002).

46. J. A. Osborn, Phys. Rev. **67**, No. 11/12, 351 (1945).

47. C. E. Patton and J. J. Green, IEEE Trans. Magn. **5** No. 3, 626 (1969).

48. C. E. Patton, J. Appl. Phys. **40**, No. 7, 2837 (1969).

49. C. E. Patton, J. Appl. Phys. **41**, No. 1, 431 (1970).

50. C. E. Patton, J. Appl. Phys. **41**, No. 4, 1637 (1970).

51. C. E. Patton and J. J. Green, Rev. Sci. Instrum. **42**, No. 2, 193 (1971).

52. C. E. Patton, *Microwave Resonance and Relaxation* in Magnetic Oxides, edited by D. J. Craik, John Wiley, London, 1975.

53. C. E. Patton, Phys. Stat. Sol. (b) **92**, 211 (1979).

54. C. E. Patton, Phys. Stat. Sol. (b) **93**, 63 (1979).

55. C. E. Patton and W. Jantz, J. Appl. Phys. **50**, No. 11, 7082 (1979).

56. C. E. Patton, IEEE Trans. Magn. **24** No. 3, 2024 (1988).

57. P. Röschmann, IEEE Trans. Magn. **14** No. 5, 1247 (1975).

58. E. Schlömann, J. Phys. Chem. Solids, **6**, No. 2/3, 242 (1958).

59. E. Schlömann, Raytheon Tech. Report R-48, Waltham Ma. (1959).

60. E. Schlömann, J.J. Green, and U. Milano, J. Appl. Phys. **31**, No. 5, Suppl., 386S (1960).

61. E. Schlömann, R. I. Joseph, and I. Bady, J. Appl. Phys. **34**, No. 7, 1998 (1963).

62. E. Schlömann, J. Appl. Phys. **34**, No. 3, 1998 (1963).

63. M. M. Scott, Ph. D. dissertation, Colorado State University, Fort Collins, Colorado (2002).

64. D. G. Scotter, J. Appl. Phys. **42**, No. 10, 4088 (1971).

65. J. Smit and H. P. J. Wijn, *Ferrites*, John Wiley, New York, 1959.

66. M. Sparks, *Ferromagnetic Relaxation Theory*, McGraw Hill Publ. Co., New York, 1964.

67. D. D. Stancil, *Theory of Magnetostatic Waves*, Springer-Verlag, New York, 1993.

68. M. Sugimoto, *Properties of Ferroxplana-Type Hexagonal Ferrites*, in Ferromagnetic Materials, edited by E. P. Wohlfarth, Vol. 3, North-Holland, Amsterdam, 1982.

69. H. Suhl, J. Phys. Chem. Solids **1**, No.4, 209 (1957).

70. J. R. Truedson, Ph. D. dissertation, Colorado State University, Fort Collins, Colorado (1993).

71. J. R. Truedson, P. Kabos, K. D. McKinstry, and C. E. Patton, J. Appl. Phys. **76**, No. 1, 432 (1994).

72. C. Vittoria, J. Magn. Magn. Mater. **21**, 109 (1980).

73. Q. H. F. Vrehen, H. G. Beljers, and J. G. M. de Lau, IEEE Trans. Magn. **5**, No. 3, 617 (1969).

74. R. A. Waldron, *Theory of Guided Electromagnetic Waves*, Van Nostrand Reinhold Company, London, 1969.

75. G. Wiese, L. Buxman, P. Kabos, and C. E. Patton, J. Appl. Phys. **75**, 1041 (1994).

76. G. Wiese, P. Kabos, and C. E. Patton, Phys. Rev. B **51**, No. 12, 15085 (1995).

77. G. Winkler, *Magnetic Garnets*, Vieweg & Sohn, Braunschweig, 1981.

78. Y. M. Yakovlev, Sov. Phys. Solid State **10**, No. 8, 1911 (1969).

79. Y. M. Yakovlev, Y. N. Burdin, Y. R. Shilnikov, and T. N. Bushueva, Sov. Phys. Solid State **12**, 2475 (1971).

80. Y. M. Yakovlev and Y. N. Burdin, Sov. Phys. Solid State **16**, No. 2, 301 (1974).

81. Y. T. Zhang, C. E. Patton, G. Srinivasan, G. O. White, C. J. Brower, and C. A. Edmondson, Rev. Sci. Instrum. 58, No. 4, 620 (1987).